ABSTRACT

Title of Dissertation:	TRANSIENT INFRARED ABSORPTION STUDIES OF MOLECULAR SUPER ROTORS PREPARED IN A TUNABLE OPTICAL CENTRIFUGE
	Tara Jade Michael, Doctor of Philosophy, 2021
Dissertation Directed By:	Professor Amy S. Mullin, Department of Chemistry and Biochemistry

In the work presented here, an ultrafast, angularly accelerating optical trap, called an optical centrifuge, rotationally excites gas-phase molecules such as N_2O, CO, and CO_2 to extremely high-J rotational levels with oriented angular momentum. Molecules in highly energetic rotational levels are known as super rotors and relax to thermal equilibrium. The state-resolved collision dynamics are investigated using polarization-sensitive high-resolution transient infrared absorption spectroscopy. Three different optical centrifuge traps are used to impart angular momentum to the gas-phase molecules: a full optical bandwidth, a reduced optical bandwidth, and a tunable optical bandwidth. New IR spectral lines of N_2O with $J = 140 - 205$ ($E_{rot} = 8{,}200 - 17{,}400\ \text{cm}^{-1}$) are reported. Polarization-dependent transient measurements of N_2O in $J = 195$ reveal high orientational anisotropy of $\boldsymbol{r} = 0.85$ produced by the centrifuge. The nearly-nascent rotational distributions of CO are investigated using two pressures and two optical centrifuge bandwidths. The shapes of the distributions beyond the peak at $J = 62$ mimic the intensity profile in the fall-off region of the shaped optical pulses. The capture and acceleration efficiencies of CO and CO_2 at comparable angular frequencies using three clipped chirps are also investigated. Nascent rotational distributions show that CO_2 and CO exhibit narrow and broad distributions, respectively, due to differences in molecular polarizability anisotropy. Surprisingly, the ratio of $[CO_2]$:[CO] trapped by the centrifuge is nearly 1.5, despite CO_2 having twice as many states as CO and about 3-fold larger polarizability anisotropy. The relaxation dynamics of CO and N_2O with He and Ar buffer gases indicate that He is more efficient at rotational quenching than is Ar, and leads to products with larger recoil.

TRANSIENT INFRARED ABSORPTION STUDIES OF MOLECULAR SUPER ROTORS PREPARED IN A TUNABLE OPTICAL CENTRIFUGE

by

Tara Jade Michael

Dissertation submitted to the Faculty of the Graduate School of the
University of Maryland, College Park, in partial fulfillment
of the requirements for the degree of
Doctor of Philosophy
2021

Advisory Committee:
Professor Amy S. Mullin, Chair
Professor John T. Fourkas
Professor Millard H. Alexander
Professor Daniel Falvey
Professor Leah Dodson
Professor Lee Mundy

Dedication

I dedicate this thesis to my mom, Marcie Rojek.

Acknowledgements

There are many people I would like to thank for their support and encouragement throughout my graduate school experience. First, I would like to thank my advisor, Dr. Amy Mullin. Her passion and enthusiasm for her students and the research was evident in our very first meeting. She has pushed me to become a better scientist and prepared me with the skill set to tackle any challenges ahead. I truly believe I picked the right research group and cherish all the moments I spent in the lab.

I would like to thank my committee members Dr. John Fourkas, Dr. Millard Alexander, Dr. Daniel Falvey, Dr. Leah Dodson, and Dr. Lee Mundy for taking the time to read and provide feedback on this thesis.

The past and present members of the Mullin group have been integral to my success in graduate school. Although my time with Dr. Matt Murray was brief, his warm welcome and enthusiastic discussions provided the best introduction to group. I would especially like to thank my amazing lab mate, Dr. Hannah Ogden, who was essential in collecting all the data presented in this thesis. Hannah provided endless support, encouragement, and guidance. She has become one of my closest friends and I could not have done this work without her. I would also like to thank Dr. Paul Diss and Christopher Lukowski for stimulating discussions, help with all the technical and instrumental issues I encountered along the way, and constant support. Matt Laskowski and Teresa Miller are two bright young scientists that made the last couple years refreshing and fun. I’m glad I had the opportunity to spend some time with the new Mullin group members, Mike, Pierce, and Eric. I’m lucky to have had such an incredible group of colleagues and friends.

Finally, I would not be the person I am today without the overwhelming strength and dedication from my amazing mother. The culmination of this work is the result of her tireless effort helping me and supporting me throughout my entire education, starting from the very beginning. All of this work is for her.

Table of Contents

List of Tables

List of Figures

List of Abbreviations

BG	Buffer gas
CDSC4000	Carbon Dioxide spectral Database
CW	Continuous-wave
FWHM	Full width at half maximum
$\lambda/2$	Half-wave plate
InSb	Indium antimonide
IP	In-plane
IR	Infrared
MPA	Multi-pass amplifier
OOP	Out-of-plane
PBC	Polarizing beam cube
QCL	Quantum cascade laser
$\lambda/4$	Quarter-wave plate
S1	Spectrum 1
S2	Spectrum 2
SR	Super rotor

Chapter 1: Introduction

1.1 Background

Molecules with large amounts of rotational energy are present in plasmas, molecular lasers, high temperature exoplanet atmospheres, and as products of photodissociation, exothermic reactions, and vibrational energy transfer.[1-20] The discovery and characterization of hot planets and simulations of exoplanet atmospheres rely on a combination of laboratory measurements of hot molecules and *ab initio* calculations.[21] Heating a gas makes it possible to observe IR transitions from highly excited levels that are not populated at ambient temperatures. However, heating can also lead to spectral congestion and line broadening, which complicate and obscure otherwise well-resolved spectra.[22] The extent of rotational excitation using linear optical methods is determined by the thermally populated rotational levels and by optical selection rules that require small changes in angular momentum quantum number. In some cases, vibration-to-rotation energy transfer can be used to excite molecules beyond thermally accessible levels.[23] An alternative approach to heating and using linear optical methods is a non-resonant optical technique, called an optical centrifuge, that drives molecules into excited rotational levels presumably without directly exciting the vibrational and translational degrees of freedom in a molecule.

The optical centrifuge is an optical trap that rotationally excites gas-phase molecules to extremely high-J rotational levels with oriented angular momentum. The highly rotationally excited molecules are known as super rotors. Villeneuve *et. al*. were the first to demonstrate the optical centrifuge, trapping and spinning Cl_2 molecules to the point of bond dissociation.[24] The optical centrifuge is comprised of two oppositely-chirped, circularly polarized pulses of light that are combined to create a linearly polarized, angularly accelerating optical field. The angularly accelerating optical field interacts with the electron clouds of gas-phase molecules, aligning the molecules with the field. Molecules that are trapped in the angularly accelerating field are spun into high rotational quantum levels. Molecules are released from the trap and have rotational angular frequencies Ω_J equal to the instantaneous trap frequency Ω_{oc} when the field intensity is not sufficient to hold them, or the kinetic energy gained in the acceleration process exceeds the interaction with the optical field.

Armon and Friedland characterized the excitation process of molecules in the optical centrifuge using both classical and quantum mechanical descriptions.[25] In the classical limit, molecules undergo autoresonance by continuously self-adjusting its rotation to the accelerating frequency of the optical trap and are driven to higher rotational levels. In the quantum limit, the molecules undergo successive quantum ladder climbing through stimulated Raman excitation involving pairs of states. Armon and Friedland describe the efficiency of the optical centrifuge to trap and rotationally excite molecules based on three timescales: the drive sweeping time (which is based on the chirp rate of the accelerating field), the Rabi drive, and the initial molecular rotation.

Using an optical centrifuge as the excitation source for rotational energy transfer studies expands our knowledge of molecular energy exchange processes by opening the door to a higher energy regime. Previous studies of rotational energy transfer of thermally accessible levels show that collisions with small $|\Delta J|$ are the most probable events, that rotational energy transfer rate constants decrease with increasing J, and that rotational energy transfer cross sections can exceed gas kinetic cross sections.[26] Rotational energy transfer is distinct from electronic and vibrational relaxation because rotational energy levels are usually spaced more closely than the thermal energy at room temperature. In addition to close energy spacing, the degeneracy of rotational levels increases with J, leading to the presence of numerous, energetically accessible channels. The details of rotational energy transfer depend to some extent on the nature of the species involved. Collisions of HF $(J = 13)$ with H_2 results in rotational relaxation rates that are 10-fold larger than for collisions with rare gases.[2,23,26-27] IR double-resonance experiments on CO+CO rotational energy transfer demonstrated that state-to-state rate data for rotational levels up to $J = 14$ are best described with a statistical polynomial-exponential gap model with rates that decrease with increasing initial rotational level.[27] Events with $|\Delta J|$ up to 6 contribute an appreciable amount to the relaxation kinetics and narrow Doppler linewidths are observed for product levels associated with the largest energy transfer rates.[27] These features are understood with a classical model of rotational energy transfer, wherein weak collisions induce small $|\Delta J|$ values and minimal changes in velocity vectors and hard collisions induce the converse.[27]

The Mullin research lab has made tremendous strides in uncovering the behavior and properties of super rotors by coupling the optical centrifuge to a high-resolution transient IR absorption spectrometer. The earliest measurements in the Mullin group used single-pass overlap of the IR probe with the optical centrifuge. Yuan *et. al.* identified new spectral lines and expanded the range of known N_2O

$(00^01 \leftarrow 00^00)$ IR transition frequencies to include $J = 93 - 99$.[28] The first polarization-dependent study of super rotors by Toro *et. al.* revealed that CO_2 in $J = 76$ acts as a molecular gyroscope, retaining its initial plane of orientation through thousands of collisions.[29] A multi-pass detection scheme was implemented in which the IR probe overlaps the optical centrifuge beam 11 times. This modification significantly improved signal-to-noise and enabled detection of higher rotational levels. Murray *et. al.* studied the relaxation dynamics of CO_2 in $J = 76$ and 100 with He and Ar buffer gas, showing that He is more effective at rotational quenching and Ar is more effective at reorienting CO_2 to isotropic distributions of angular momentum vectors.[30] Ogden *et. al.* identified new IR spectral transitions of N_2O $(00^01 \leftarrow 00^00)$ from $J = 140 - 205$ and measured the first inverted rotational distribution, indicating that we were getting closer to the nascent distribution of centrifuged molecules.[31] In the work presented here, a tunable optical centrifuge is created with the implementation of an adjustable beam block, such that rotational levels can be selectively populated, and the dynamics of the nascent (or nearly-nascent) centrifuged distributions are explored.

1.2 Outline

The outline of the thesis is as follows:

- Chapter 2: This chapter describes the main components of the optical centrifuge coupled to a high-resolution transient IR absorption spectrometer. The theory, experimental design, and data analysis for trapping, spinning, and detecting molecules in high-J levels is explained.
- Chapter 3: New IR spectral transitions of N_2O $(00^01 \leftarrow 00^00)$ are measured for rotational levels $J = 140 - 205$. The collision dynamics of optically

centrifuged N_2O in $J = 92 - 195$ is investigated at a pressure of 5 Torr and with a reduced optical bandwidth optical centrifuge. Polarization-dependent Doppler-broadened line profiles for $J \geq 180$ show small translational energy gain from near-resonant collisional energy transfer and large values of orientational anisotropy, near $r = 0.77$.

- Chapter 4: The nearly-nascent rotational distributions of CO are measured at two pressures (2.5 and 5 Torr) and with two optical centrifuge bandwidths (full and reduced). Polarization-dependent measurements reveal an inverted rotational distribution that peaks at $J = 62$. The distribution above $J > 62$ correlates to the shape of the trap intensity, resulting in broader and sharper distributions using the full and reduced optical bandwidths, respectively. Doppler profiles show translation $T < 300$ K for $J = 75$.
- Chapter 5: A tunable optical centrifuge is made with an adjustable beam block to compare the nascent rotational distributions of CO and CO_2 with comparable angular frequencies at a pressure of 500 mTorr. Absolute number densities were calculated from transient measurements and reveal that the centrifuge traps CO_2 about 1.5 times more efficiently than CO. Narrow and broad distributions produced by CO_2 and CO, respectively, suggest that the centrifuge traps about the same number density of CO and CO_2 molecules but the molecular properties, such as polarizability, govern the shape of the nascent distribution.
- Chapter 6: The collision dynamics of CO and N_2O super rotors with He and Ar buffer gas are investigated. Doppler broadened line profiles of CO in $J = 42 -$

62 show that collisions between CO and He are mainly adiabatic. Doppler profiles show large translational gain for collisions of N_2O in $J = 195$ with He, indicating sudden collisional energy transfer. N_2O in $J = 140 - 195$ show less population change and translational energy gain with the addition of Ar, indicating mainly adiabatic collisions.

- Chapter 7: Overall conclusions of the experiments presented in this work are discussed and suggestions for future experiments are given.

Chapter 2: Experimental Methods and Analysis

This chapter describes the experimental methods used to create an ensemble of super rotors and study the time-dependent collision dynamics as the molecules relax to thermal equilibrium. The chirped output of a 1 Khz Ti:Sapphire regenerative amplifier is further shaped to create two oppositely chirped pulses that enter a multi-pass amplifier pumped by an Nd:YAG laser. The amplified pulses are overlapped in space and time using a delay stage and polarizing beam cube, creating an angularly accelerating pulse. The pulse is focused into a gas sample cell to rotationally excite molecules. A quantum cascade laser (QCL) is tuned to specific infrared (IR) ro-vibrational transitions of gas-phase molecules, and the time-dependent appearance in individual rotational levels is measured with a transient IR absorption spectroscopy. The frequency of the IR light is stabilized with active feedback control using a wavemeter, an etalon, and a lock-in amplifier. The main components of the optical centrifuge and high-resolution transient IR absorption spectrometer are shown in Figure 2.1. Molecules such as N_2O, CO_2, and CO were investigated using this technique. In the following sections, N_2O and CO will be used as examples to illustrate the experimental approach.

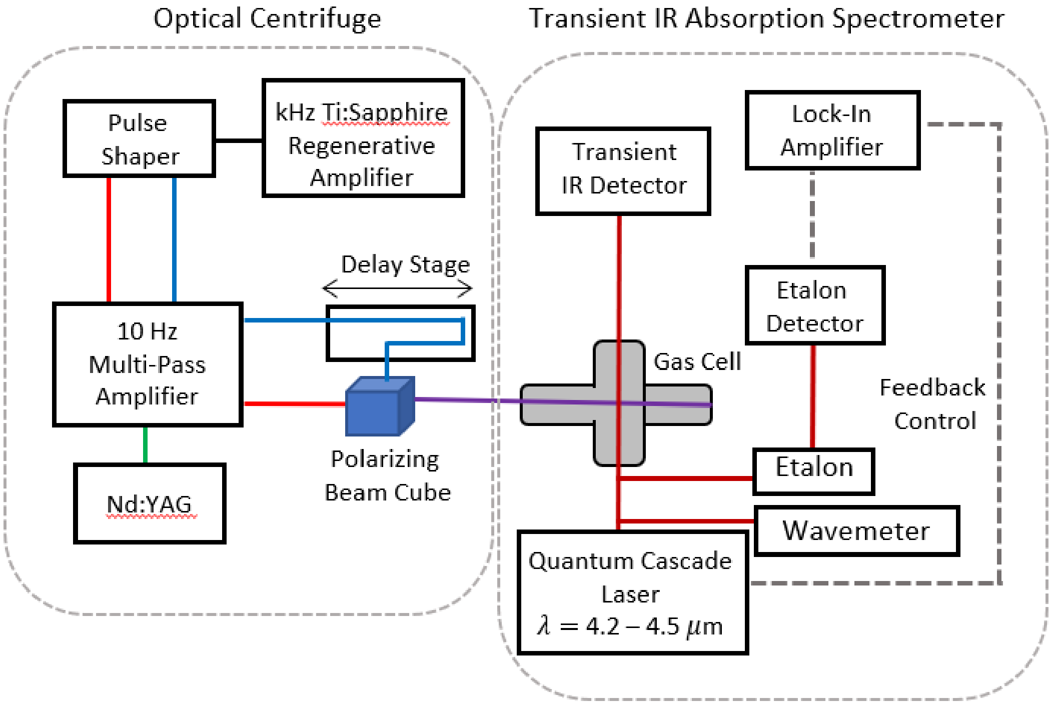

Figure 2.1 The main components of the optical centrifuge and the wavelength-stabilized transient IR absorption spectrometer.

2.1 Creating the Optical Centrifuge

2.1.1 Theory

In the research presented here, an optical centrifuge is used to rotationally excite an ensemble of gas-phase molecules to extremely high rotational levels with oriented angular momentum. In this section, the fundamental principles of creating and using an optical centrifuge are described.

The optical centrifuge produces a linearly polarized, angularly accelerating optical field that traps and spins a thermal sample of gas-phase molecules into high rotational levels. The technique was first described by Ivanov and coworkers and is based on shaped ultrafast laser pulses.[32] The optical field induces a dipole moment $\vec{\mu}_{ind}$ in gas-phase molecules that have polarizability anisotropy $\Delta\alpha$, where $\Delta\alpha = \alpha_{\parallel} -$

$\alpha_\perp$ and $\alpha_\parallel > \alpha_\perp$. The depth of the interaction potential U_0 between the electric field and the molecule is

$$U_0 = \frac{-1}{4}\Delta\alpha E^2 cos^2(\theta), \qquad (2.1)$$

where E^2 is the optical intensity and θ is the angle between the most polarizable axis of the molecule and the polarization. The interaction potential is most stable when the field and axis of maximum polarizability are parallel ($\theta = 0$), as shown in Figure 2.2.

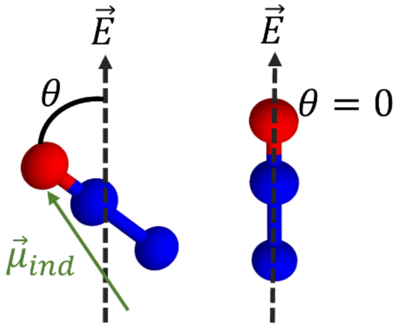

Figure 2.2 Induced dipole of N_2O leading to alignment with the optical field.

The optical field angularly accelerates based on the temporal chirps of the pulses, as described in Section 2.1.2. Molecules that are aligned with the instantaneous optical field rotate with the field, gaining rotational energy and angular momentum. Based on Equation 2.1, molecules with larger values of $\Delta\alpha$ have a stronger interaction with the angularly accelerating field. The strength of the optical trap also depends on the pulse intensity. Once the optical trap falls below a critical minimum intensity, the interaction is no longer strong enough to hold onto the molecules, and they can fall out of the trap. A molecule remains trapped in the optical centrifuge field if the rotational kinetic energy K gained does not exceed the potential energy U_0. The kinetic energy gained by the molecule during the turn-on time t_{on} of the centrifuge is determined by

$$K \sim \frac{1}{2}U_0 + \frac{1}{2}I(\beta t_{on})^2, \qquad (2.2)$$

where I is the molecule's moment of inertia. Here, the first term comes from the Virial Theorem and the second term is due to the rotation of the frame.[32]

The angular acceleration of the optical trap is controlled by overlapping, in space and time, two oppositely chirped pulses of opposite circular polarizations. The chirped pulses have time-dependent optical frequencies in units of radians s^{-1}. The positively chirped pulse is denoted 1 and the negatively chirped pulse is denoted 2, and their instantaneous frequencies are given by

$$\omega_1(t) = \omega_0 + \beta(t) \tag{2.3}$$

and

$$\omega_2(t) = \omega_0 - \beta(t), \tag{2.4}$$

respectively. Here, ω_0 is the initial frequency of light corresponding to $\lambda_0 = 805\ nm$, and β. In our apparatus, β is 0.5×10^{12} radians s^{-1} ps^{-1}. The pair of oppositely chirped pulses together create an angularly accelerating, linearly polarized optical field. The linear field results from combining pulses with opposite chirp and opposite circular polarization, as shown in Equation 2.5 where $\Delta\omega(t) = \omega_1(t) - \omega_2(t)$.

$$\vec{E}(t) = E_0(\mathrm{t})\cos\left(\omega_0 t\right)\left[\cos\left(\frac{\Delta\omega}{2}t\right)\hat{x} - \sin\left(\frac{\Delta\omega}{2}t\right)\hat{y}\right]. \tag{2.5}$$

The chirped pulses 1 and 2 have the same initial frequency ω_0. The instantaneous frequencies diverge and the angular acceleration of the optical trap increases linearly with $\Delta\omega(t)$. The instantaneous angular frequency $\Omega_{OC}(t)$ of the optical trap is half of the time-dependent frequency difference $\Delta\omega(t)$ between the two chirped pulses, in

$$\Omega_{OC}(t) = \frac{1}{2}\Delta\omega = \frac{1}{2}(\omega_1(t) - \omega_2(t)). \tag{2.6}$$

Based on Equation 2.6, the maximum acceleration Ω_{max} of the optical field is dependent on the temporal overlap the pulses. The terminal angular frequency of the optical trap can be controlled by removing selected frequencies from one or both of the chirped pulses, ending the angular acceleration of the field at lower angular frequencies.

In our experiments, the optical trap interacts with a sample of gas-phase molecules at 300 K. The initial rotational distribution of the sample is isotropic, as illustrated in Figure 2.3a. The propagation vector $\vec{k}_{oc}$ of the optical centrifuge pulse is along the *z*-direction and the optical field spins in the xy-plane, causing trapped molecules to be angularly accelerated in the *xy*-plane, as shown in Figure 2.3b. This process results in an ensemble of molecules with unidirectional spin and oriented angular momentum vectors, as in Figure 2.3c.

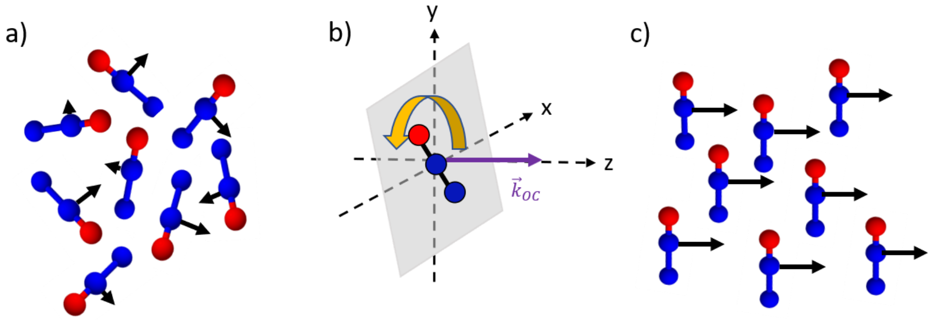

Figure 2.3 a) Rotational, isotropic distribution of a thermal N_2O gas sample. The arrows indicate angular momentum vectors. b) The optical centrifuge pulses propagate in the *z*-direction causing trapped molecules to rotate in the *xy*-plane. c) An ensemble of molecules with oriented angular momentum is created.

2.1.2 Stretching and Amplifying the Pulses

The optical centrifuge has four main components: an ultrafast Ti:Sapphire oscillator, a regenerative amplifier, a custom-built spectral pulse shaper, and a multi-pass amplifier, as shown in Figure 2.4. Each of these components is described in this section.

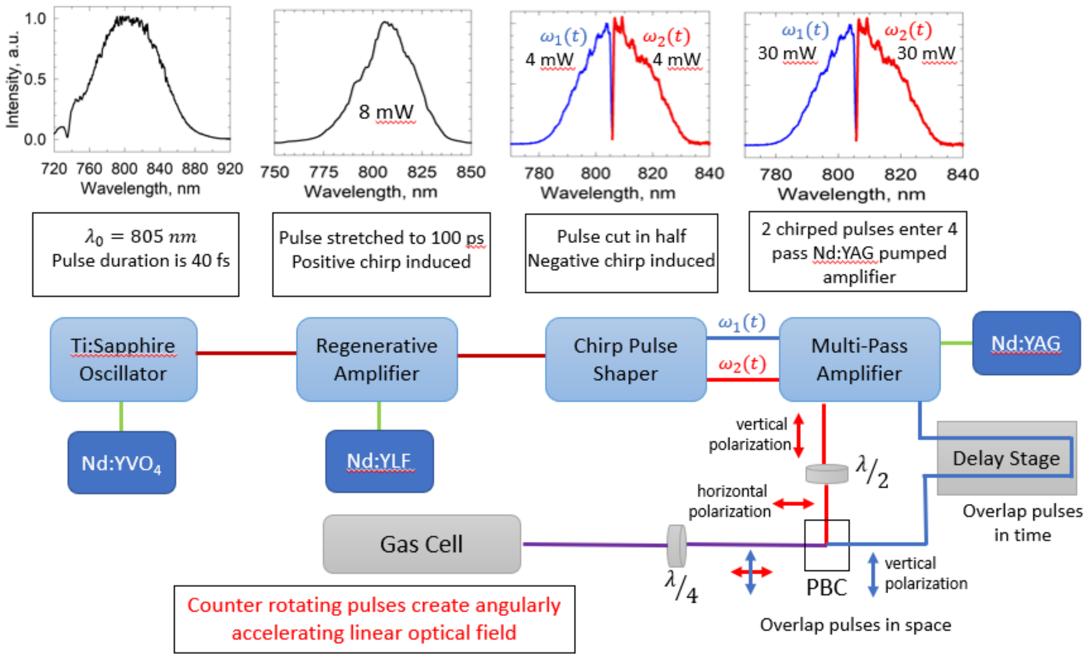

Figure 2.4 Schematic of the major components involved in the optical centrifuge.

A Ti:Sapphire oscillator pumped by a diode pumped, frequency doubled $Nd:YVO_4$ laser at 532 nm produces 40 fs pulses centered at $\lambda_0 = 805$ nm at a repetition rate of 80 MHz.

The pulse stretching is achieved with a pair of gratings and retro-reflecting mirrors. The oscillator output is dispersed by a grating such that blue wavelengths travel a longer distance than red wavelengths, and then is reflected by a curved gold mirror. At this point, the pulse duration is 100 ps and the pulse is positively chirped. The stretched pulse then enters a multi-pass, Ti:Sapphire regenerative amplifier that is pumped with 527 nm light from a frequency-doubled Nd:YLF laser. The pulse undergoes several round trips, leading to amplification gain of over 10^6. The amplified pulse leaves the resonator with vertical polarization. The timing of amplification and cavity dumping in the regenerative amplifier is controlled using a pair of Pockels cells. The first Pockels cell allows a single pulse into the resonator, and the second Pockels cell releases the amplified pulse from the resonator after a sufficient number of round trips. The regenerative amplifier runs at a repetition rate of 1 kHz and a pulse picker reduces the output to a repetition rate of 10 Hz.

The output of the regenerative amplifier enters a custom-built spectral pulse shaper. The positively chirped pulse is cut in half spectrally to create two spatially separated pulses, each with 50 ps pulse duration. One of the pulses maintains a positive chirp, whereas the other pulse is given a negative chirp using a pair of gratings.

The output of the pulse shaper then enters a multi-pass amplifier (MPA). The MPA contains two Ti:Sapphire rods pumped at 10 Hz by 532 nm light from a frequency doubled Nd:YAG. Each chirped pulse passes through a Ti:Sapphire rod four times, and is amplified 4-fold on each pass. Each chirped pulse has a final pulse energy near 30 mJ. A schematic of the beam path for one of the chirped pulses through the MPA is shown in Figure 2.5.

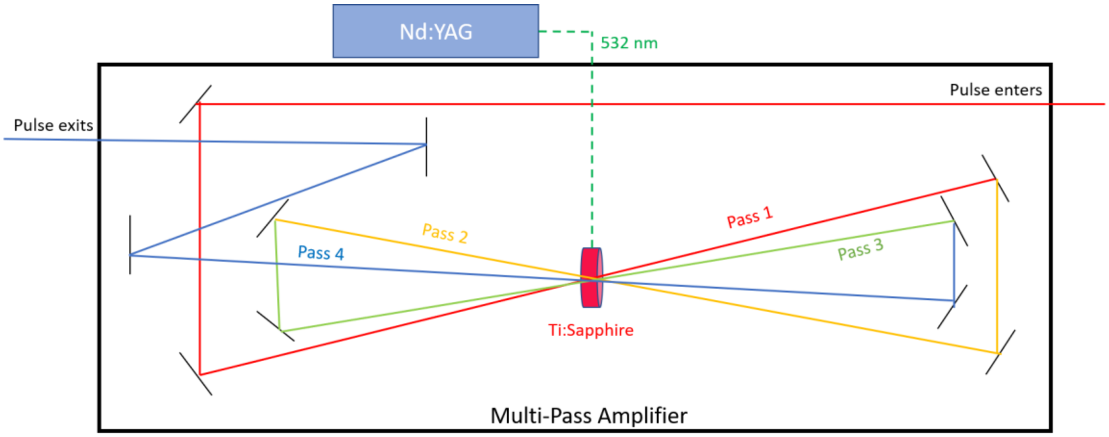

Figure 2.5 Beam path of one chirped pulse through the multi-pass amplifier. The Ti:Sapphire crystals are the gain medium, and are pumped at 10 Hz by 532 nm light from a frequency-doubled Nd:YAG laser.

The two pulses exit the MPA with the same vertical polarization. The positively chirped pulse is sent through a delay stage and the negatively chirped pulse is sent through a half-wave plate ($\lambda/2$) to rotate its polarization by $90°$. The pair of pulses with orthogonal polarization are spatially combined in a polarizing beam cube (PBC). The pulses are then combined, using the delay stage to control the relative timing. The combined pulses pass through a quarter-wave plate ($\lambda/4$), which induces opposite circular polarization in each pulse. The combination of oppositely-chirped pulses with counter-rotating circular polarization results in a linearly polarized optical field that angularly accelerates over the time of the pulse. The final pulse is focused into a gas cell with a beam waist of 53 μm (with a 106 μm diameter cross section) using a 50 cm focal length lens. The combined pulse energy that enters the cell is reduced by 8% (from 60 mJ to 55.2 mJ) due to losses in optical components. The pulse irradiance at the focal point in the sample cell is typically $I = 2.5 \times 10^{14}$ W cm^{-2}.

2.1.3 Creating a Tunable Optical Centrifuge

The optical centrifuge trap requires the overlap of the oppositely-chirped pulses in both space and time. Figure 2.6a shows the full bandwidth spectrum of the optical centrifuge and Figure 2.6b shows the intensity of the optical trap as a function of the instantaneous angular frequency Ω_{oc}.

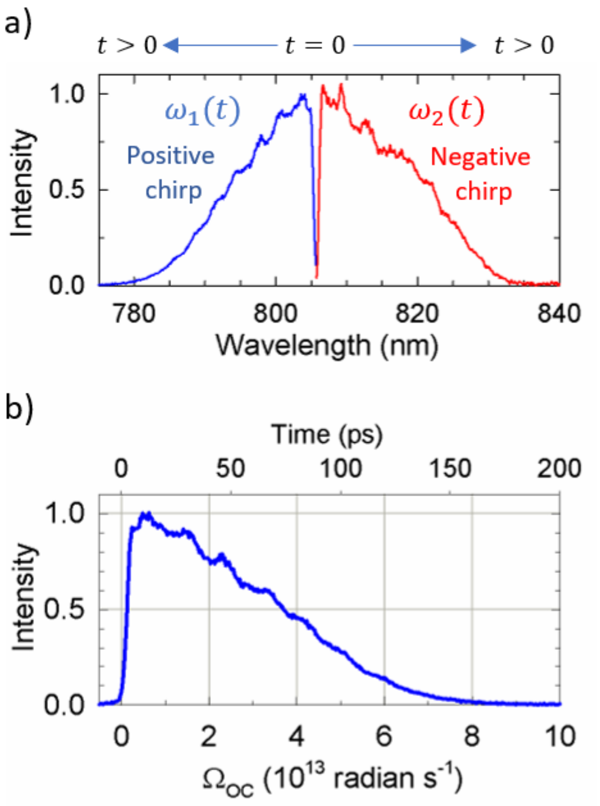

Figure 2.6 a) Spectra of the two pulses at the full bandwidth. b) Instantaneous angular frequency Ω_{oc} of the optical centrifuge using the full bandwidth.

The ultimate angular acceleration Ω_{max} of the optical centrifuge depends on the spectral bandwidth $\Delta\omega$ of the initial optical pulse. The angular acceleration of the optical trap is interrupted if the spectrum of one pulse is blocked beyond a certain wavelength. For the experiments described in this thesis, the spectral bandwidth of one pulse was used to control the rotational levels excited. The spectral bandwidth of the optical trap was reduced by introducing a movable beam block in the pulse shaper, as shown in Figure 2.7. The beam block removes an adjustable amount of the short wavelength portion of the positively-chirped pulse, decreasing the overall bandwidth of the trap and thereby the maximum angular acceleration of the field Ω_{max}.

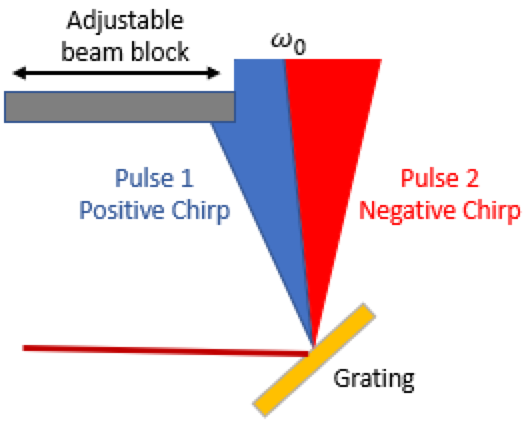

Figure 2.7 Schematic of making a tunable optical centrifuge made reducing the bandwidth of the positively-chirped pulse.

Figure 2.8a shows the spectrum of oppositely chirped pulses where the bandwidth of the positively chirped pulse (blue) has been reduced by the beam block, compared to the full bandwidth shown in grey. Figure 2.8b shows the instantaneous angular frequency of the reduced bandwidth trap in blue. The full optical bandwidth leads to a maximum angular acceleration with Ω_{max} near 6.0×10^{13} radians s^{-1}, as shown in grey. The reduced optical bandwidth in Figure 2.8b leads to a maximum angular acceleration with Ω_{max} near 3.3×10^{13} radians s^{-1}, as shown in blue.

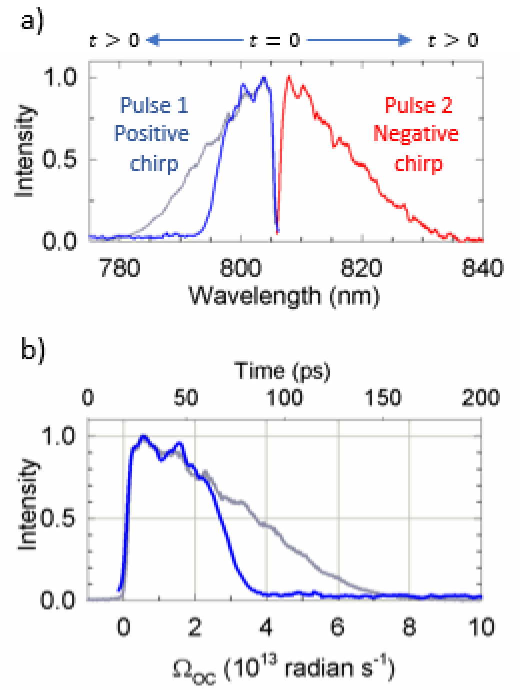

Figure 2.8 a) Reduced spectrum of positively chirped pulse (blue), compared to the full spectrum (grey). b) Instantaneous angular frequency of the reduced-bandwidth optical trap (blue), compared to the full bandwidth trap (grey).

2.1.4 Rotational Energy of Optically Centrifuged Molecules

The angular frequency Ω_J of molecules trapped in the optical centrifuge is equal to the instantaneous angular frequency Ω_{OC} of the field. The extent to which rotational energy is imparted to optically centrifuged molecules depends on the value of Ω_{max} for the optical trap. The classical rotational energy of a centrifuged molecule is equated to its quantum energy, i.e.

$$E_{rot} = \frac{1}{2} I \Omega_J^2 = BJ(J+1). \qquad (2.7)$$

Here, I is the molecule's moment of inertia, Ω_J is its classical angular frequency, B is the rotational constant for the quantum rigid-rotor model, and J is the rotational quantum number. The highest rotational quantum level produced by the optical centrifuge is estimated using the approximation that $J(J+1) \approx J_{max}^2$ to yield

$$J_{max} \approx \frac{I\Omega_J}{\hbar}, \tag{2.8}$$

(where $\hbar$ is Planck's constant). Values of J_{max} are determined using the molecule's moment of inertia. Table 2.1 shows J_{max} values for CO, N_2O, and CO_2 for the full bandwidth trap and for the reduced bandwidth trap shown in Figure 2.8, along with their rotational energies E_{rot}.

Table 2.1. Estimated values of J_{max} and rotational energy for CO_2, N_2O, and CO

Molecule	Moment of Inertia (10^{-46}kg m^2)	J_{max} (E_{rot} in cm^{-1})	
		$\Omega_{max} = 6.0 \times 10^{13}$ radians s^{-1}	$\Omega_{max} = 3.3 \times 10^{13}$ radians s^{-1}
CO	1.46	84 (13,700)	46 (4,150)
N_2O	6.68	380 (60,700)	208 (18,200)
CO_2	7.17	408 (65,100)	226 (20,000)

For comparison between rotational levels that are accessed using the optical centrifuge and thermally possible levels, a maximum J_0 value for which the sum of thermal population from $J = 0$ to J_0 is 0.999 is defined. For linear molecules, J_0 can be estimated by

$$J_0 \approx 2.5\sqrt{k_B T/B}, \tag{2.9}$$

where k_B is Boltzmann's constant. The highest thermally accessible rotational levels for CO, N_2O, and CO_2 are $J_0 = 26, 56$, and 58, respectively.

2.2 High-Resolution Transient Infrared Absorption Spectroscopy

2.2.1 Theory of State-Resolved Transient Absorption

The research presented here uses a high-resolution transient IR absorption spectrometer to investigate the spectroscopy, quantum level distributions, and collisional energy transfer dynamics of molecules in extreme rotational levels as prepared by an optical centrifuge. The instrumentation used to make these measurements is described in the next section. Here, the theory of transient IR absorption spectroscopy is discussed, and examples of transient absorption signals are shown.

The optical centrifuge pulse creates an inverted rotational distribution that populates energy levels well above those populated at 300 K. The subsequent state-resolved relaxation dynamics are measured by probing individual rovibrational transitions with high-resolution, continuous-wave (CW) IR light. A schematic of the excitation process and IR probing is shown in Figure 2.9a for optically centrifuged N_2O. The IR probe transitions involve one quantum absorption in the asymmetric stretch mode $(00^01, J+1 \leftarrow 00^00, J)$ near $\lambda = 4.4$ μm. The selection rule for IR absorption is $\Delta J = \pm 1$ where ΔJ is the change in rotational quantum number; P-branch transitions have $\Delta J = -1$ and R-branch transitions have $\Delta J = +1$. An example of a R-branch $(00^01 \leftarrow 00^00)$ transition of N_2O in the $J = 180$ level is shown in Figure 2.9b. In the work presented here, two types of state-resolved dynamics are probed. In some cases, the nascent distribution of optically centrifuged rotational levels is probed directly. In other experiments, the products of collisional energy transfer are measured.

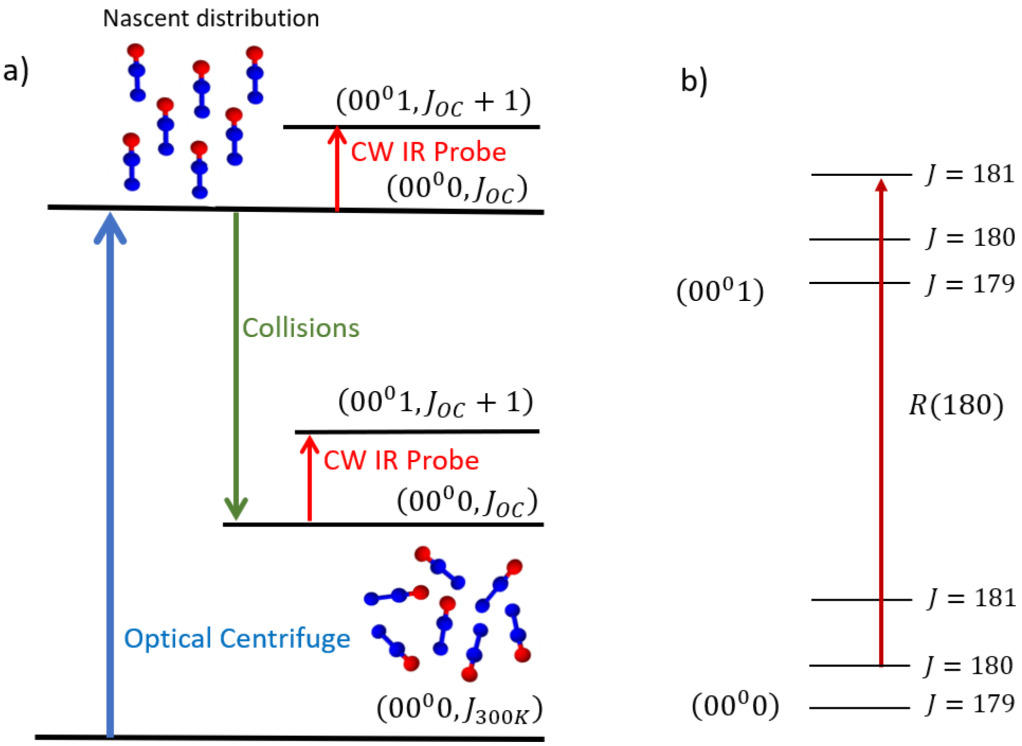

Figure 2.9 a) Schematic of the transient IR probing of N_2O molecules excited in an optical centrifuge and their subsequent collision dynamics. b) R-branch ($00^01 \leftarrow 00^00$) transition of $J = 180$.

Fractional linear IR absorption is proportional to the population of molecules in a specific rovibrational state. Beer's Law for absorption is

$$I_t/I_0 \;= e^{-\alpha p \ell}, \tag{2.10}$$

where I_t is the transmitted light intensity, I_0 is the incident light intensity, α is the absorption coefficient, p is the pressure, and ℓ is the pathlength. Fractional absorption measurements $\Delta I/I_0$ are used to determine I_t/I_0, where $I_t/I_0 = 1 - \Delta I/I_0$. The state-specific "pressure" of centrifuged molecules is converted to a number density using the ideal gas law. Figure 2.10 shows the transient absorption at 500 mTorr of the same CO level using a reduced optical bandwidth and a full optical bandwidth. For the experimental conditions in these measurements, CO in $J = 41$ using a reduced-bandwidth centrifuge is part of the nascent distribution of centrifuged molecules, whereas population in the $J = 41$ level using the full bandwidth centrifuge results from collisions. The transient signal from $t = 0$ to the peak absorption is shown in red. Transient absorption signals of molecules produced in the nascent distribution have a prompt response, whereas absorption of collision-induced levels exhibit a gradual increase as the rotational population grows in. The increase in population using a reduced bandwidth centrifuge is apparent from the fact that the $J = 41$ signal is 3-fold larger than for the full bandwidth centrifuge.

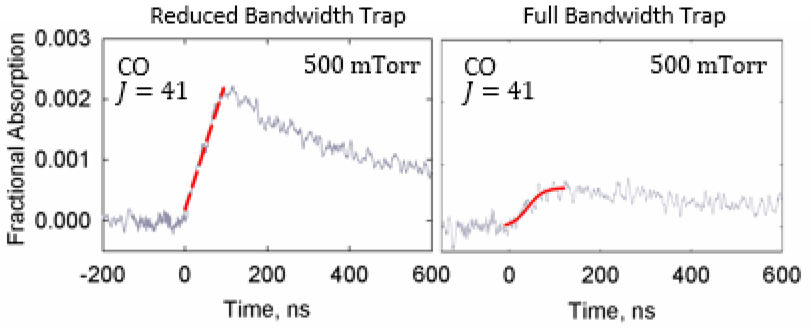

Figure 2.10 Transient fractional absorption signals of CO $J = 41$ at a pressure of 500 mTorr following excitation using a reduced (left) and full (right) bandwidth centrifuge.

The absorption coefficient is defined by

$$\alpha = Sf(0)N, \qquad (2.11)$$

where S is the absorption strength, $f(0)$ is a line-shape factor, and N is defined based on the ideal gas law as $N = n/(PV) = 1/(RT)$, where T is the temperature for which S was determined. S is a measure of the integrated absorption strength for a rotationally-resolved IR transition at a specific temperature, as defined by

$$S = \int_0^\infty \sigma(\nu)d\nu, \qquad (2.12)$$

where $\sigma(\nu)$ is the cross-section for absorption and ν is the frequency of light. S has units of cm^{-1}/(molecule cm^{-2}) and is reported in the HITRAN spectral database for $T =$

296 K. The line-shape factor $f(0)$ takes into account the Gaussian Doppler-broadened absorption line profile. The functional form of $f(0)$ is given by

$$f(0) = \frac{2}{\Delta\nu_{Dop}}\sqrt{\frac{ln2}{\pi}}. \tag{2.13}$$

Here $\Delta\nu_{Dop}$ is the full width at half maximum (FWHM) of the Doppler-broadened line profile. The line width of a Doppler-broadened line profile is a measure of the state-specific translational temperature:

$$\Delta\nu_{Dop} = \sqrt{\frac{8k_B T ln2}{mc^2}}\nu_0, \tag{2.14}$$

Here, T is the translational temperature, m is the molecular mass, c is the speed of light, and ν_0 is line-center transition frequency. Figure 2.11 shows a transient Doppler-broadened line profile measured for N_2O in $J = 180$ at $t = 60$ ns following the optical centrifuge pulse. The observed line width $\Delta\nu_{obs}$ corresponds to a transient line profile with a dynamic translational temperature T_{trans}. Fitting the data to a Gaussian profile yields a translational temperature of $T_{trans} = 607 \pm 50$ K.

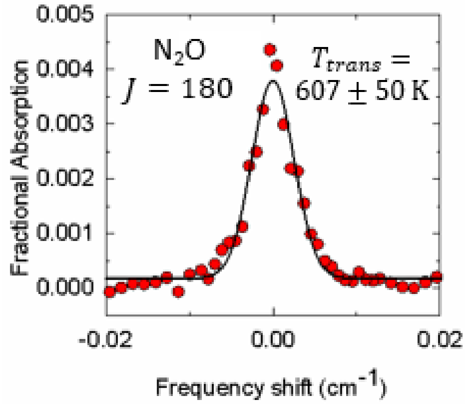

Figure 2.11 Transient Doppler-broadened line profile measured at $t = 60$ ns following the optical centrifuge pulse for the N_2O $J = 180$ level at a pressure of 5 Torr.

Molecules with non-zero velocity components along the IR propagation vector absorb light at different frequencies from the center frequency based on the Doppler effect. The observed absorption frequency ν is shifted from line center ν_0 based on the ratio of the velocity V to the speed of light c via

$$\nu = \nu_0 \left(1 + \frac{V}{c}\right). \tag{2.15}$$

When an equal number of molecules are moving towards the detector and away from the detector, the spectral absorption line is broadened symmetrically about the line-center frequency ν_0.

State-specific number densities n_{vJ}/V are determined from line-center fractional absorption measurements and Doppler-broadened line profiles using Equation 2.16, where f_v and f_J are fractional population in vibration and rotational level at $T = 296$ K:

$$\frac{n_{vJ}}{V} = \frac{-\ln\left(\frac{I_t}{I_0}\right)}{Sf(0)\ell} f_v f_J \frac{\Delta\nu_{obs}}{\Delta\nu_{Dop}} \tag{2.16}$$

Here, f_v and f_J are fractional population in vibration and rotation, respectively, for the v, J state at $T = 296$ K. The fractional population in a quantum state i is defined by the Boltzmann equation

$$f_i = \frac{g_i \exp\left(-E_i/k_B T\right)}{Q_i}, \tag{2.17}$$

where g_i is the degeneracy and Q_i is the partition function.

2.2.2 Transient IR Absorption Experimental Components

The optical centrifuge is used in conjunction with to a high-resolution transient IR absorption spectrometer to measure the state-specific relaxation dynamics of super rotors. State-resolved transient absorption measurements reveal how populations of individual rovibrational levels evolve in time. IR polarization-dependent spectroscopy is used to study the time evolution of orientational anisotropies of super rotors. Doppler-broadened line profiles are a measure of the amount of translational energy in a specific rotational level. Together, this information helps to elucidate the dynamics of collisions involved in rotational energy transfer of super rotors.

Figure 2.12 shows a schematic of the high-resolution IR spectrometer. The IR probe source is a linearly polarized quantum cascade laser (QCL) from Daylight Solutions operating between $\lambda = 4.2$ μm and 4.5 μm. The QCL has a frequency resolution of $\Delta\nu_{IR} < 2 \times 10^{-4}$ cm^2. A half-wave plate is used to control the angle of IR polarization. The IR probe enters a gas cell and makes 11 passes between two gold mirrors before detection on a liquid nitrogen cooled indium antimonide (InSb) detector.

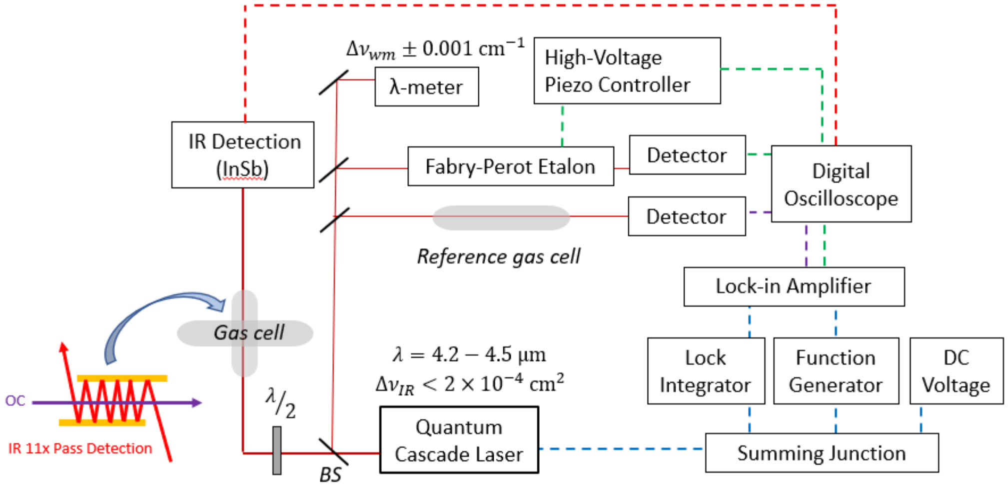

Figure 2.12 Schematic diagram of the high-resolution IR spectrometer experimental set-up.

The IR detectors used in this research have rise times of either 50 ns or 100 ns. The transient fractional absorption signals are collected on two channels of a digital oscilloscope, one AC-coupled and the other DC-coupled. The AC-coupled channel is a measure of transient IR absorption ΔI. The DC-coupled signal is a measure of the transient transmitted intensity I_t. The oscilloscope is triggered at $t = 0$ by detecting the optical centrifuge pulse with a photodiode. For a negatively–biased IR detector, the AC- and DC-coupled channels are transformed into fractional absorption $\Delta I/I_0$ using

$$\left|\frac{\Delta I}{I_0}\right| = \frac{\langle AC\rangle}{\langle DC\rangle - \langle AC\rangle} = \frac{\Delta I}{I_t - \Delta I}. \tag{2.18}$$

The pathlength of IR and optical centrifuge overlap is $\ell = 0.12$ cm. Prior to the sample cell, a portion of the IR light from the QCL is split off and used for wavelength measurement with a wavemeter, and for active feedback control for frequency stabilization. Frequency control is achieved by passing the IR light either through a reference gas cell or a tunable Fabry-Perot etalon. A lock-in amplifier is used to lock the output frequency of the QCL to an absorption line of a known molecular transition or to a fringe of the tunable etalon. The etalon cavity length is controlled with a high-voltage piezo controller. A voltage is sent to the piezo-mounted mirror, causing changes in cavity length and the integer number of wavelengths that constructively interfere within the cavity. The lock-in amplifier applies a voltage to the QCL to change the IR frequency to maintain an integer number of wavelengths in the new etalon cavity. This method allows for controlled tuning across a line-center absorption in small frequency steps of 0.001 cm^{-1}. The wavemeter is a traveling Michelson interferometer that measures the IR frequency with a frequency resolution of $\Delta\nu_{wm} = 0.001$ cm^{-1}.

2.2.3 Polarization Spectroscopy of Optically Centrifuged Molecules

The optical centrifuge creates an ensemble of molecules with oriented angular momentum vectors. Figure 2.13 shows the geometry of the interaction region, with the propagation vector of the optical centrifuge $\vec{k}_{OC}$ along the *z*-axis, causing molecules to spin in the *xy*-frame. The IR probe beam crosses the optical centrifuge beam perpendicularly and $\vec{k}_{IR}$ lies along the *x*-axis. The IR probe polarization is controlled using a wave plate to rotate the polarization by 90°. IR light with vertical polarization has an electric field $E_{\parallel}$ that is parallel to the plane of rotation, yielding transient signals denoted as $t_{\parallel}$. IR probing with horizontal polarization has an electric field $E_{\perp}$ that is perpendicular to the plane of rotation, with transient signals denoted $t_{\perp}$.

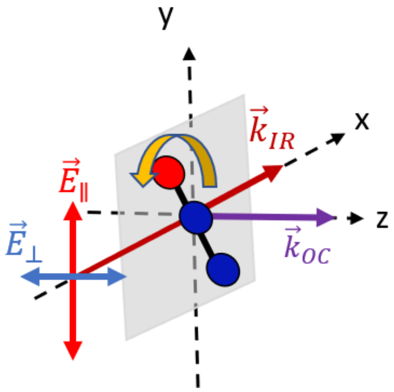

Figure 2.13 Geometry of the IR detection region with either parallel or perpendicular probing relative to the plane of molecular rotation.

Transient absorption measurements collected with both vertical and horizontal IR polarizations, that probe either parallel or perpendicular to the plane of molecular rotation, ($t_{\parallel}$ and $t_{\perp}$) are used to separate in-plane and out-of-plane angular momentum components. In-plane transient signals t_z are absorption measurements of molecules with a component of their angular momentum aligned with the *z*-axis. These are molecules directly prepared by the optical centrifuge that have oriented angular momentum. Out-of-plane transient signals $(t_x + t_y)$ are absorption measurements of molecules with a component of their angular momentum along the *x*- or *y*- axis. This group consists of bath molecules or super rotor molecules that have been reoriented due to collisions. In-plane and out-of-plane signals are defined by

$$t_z = 2t_\parallel - t_\perp \tag{2.19}$$

and

$$t_x + t_y = 2t_\perp, \tag{2.20}$$

respectively. The orientational anisotropy r shown in Equation 2.21 is a fractional measure of molecules with in-plane components relative to all molecules in a given quantum level

$$r = \frac{t_z}{t_x + t_y + t_z} = \frac{2t_\parallel - t_\perp}{2t_\parallel + t_\perp}. \tag{2.21}$$

2.2.4 Gas Kinetic Rate Constants

The number of collisions in the experiments presented here is controlled using pressure. Reduced pressure leads to a longer time between collisions, and thereby gives access to dynamic information that is closer to the nascent distribution of centrifuged molecules. The pressures used in this research range from 500 mTorr to 10 Torr, with measurements at $t = 100$ ns, corresponding to nascent distributions for the former pressure and approximately 10 collisions for the latter pressure.

The collision rate in a gas-phase sample is given by

$$\frac{dN_{col}}{dt} = k_{col}\rho, \tag{2.22}$$

where N_{col} is the number density of collisions, t is time, ρ is the number density of the gas, and k_{col} is the collision rate constant. The thermally averaged collision rate constant is defined by

$$k = \sigma\langle v_{rel}\rangle, \tag{2.23}$$

where σ is the collision cross section and $\langle v_{rel}\rangle$ is the average relative velocity, defined by

$$\langle v_{rel}\rangle = \sqrt{\frac{8k_BT}{\pi\mu}}. \tag{2.24}$$

A hard-sphere model defines the collision cross section by $\sigma = \pi d^2$ where d is the effective radius of the collision pair. A Lennard-Jones model uses the distance parameter σ_{LJ} and well depth of a potential ε defined by

$$V_{LJ}(r) = 4\varepsilon\left(\left(\frac{\sigma_{LJ}}{r}\right)^{12} - \left(\frac{\sigma_{LJ}}{r}\right)^{6}\right) \tag{2.25}$$

to measure to a Lennard-Jones collision rate constant given by

$$k_{LJ} = \pi{\sigma_{LJ}}^2\,\Omega^{(2,2)*}v_{rel}. \tag{2.26}$$

The collision integral $\Omega^{(2,2)*}$ is determined at a reduced temperature $T^* = k_BT/\varepsilon$ as follows:

$$\Omega^{(2,2)*} = 1.16145(T^*)^{-0.14874} + 0.52487\exp(-0.7732\,T^*) + 2.16178\exp(-2.438787\,T^*) \tag{2.27}$$

Tables 2.2 and 2.3 show the parameters and collision rate constants at 300 K using hard sphere and Lennard-Jones models, respectively.

Table 2.2 Hard-sphere parameters and collision rate constants at 300 K

	σ_{HS} (pm)	μ (10^{-26} kg)	v_{rel} (m s^{-1})	k_{HS} (10^{-10} cm^3 s^{-1})
CO	350	2.34	672	2.58
CO_2	375	3.67	536	2.37
N_2O	388	3.67	536	2.53

Table 2.3 Lennard-Jones parameters and collision rate constants at 300 K

	ε/k_B (K)	σ_{LJ} (pm)	μ (10^{-26} kg)	v_{rel} (m s^{-1})	k_{LJ} (10^{-10} cm^3 s^{-1})
CO	135	350	2.34	672	2.93
CO_2	246	375	3.67	536	3.42
N_2O	220	388	3.67	536	3.47

The average time between collisions is determined from the collision rate constant using

$$\frac{dt}{dN_{col}} = (k_{col}\,\rho)^{-1}. \tag{2.28}$$

Tables 2.4 and 2.5 show the average time between collisions using collision rate constants from hard sphere and Lennard-Jones models for CO, CO_2, and N_2O at pressures of 500 mTorr to 10 Torr.

Table 2.4 Average time between collisions based on hard-sphere rate constants

P(Torr)	ρ(cm^{-3})	dt/dN_{col} (ns)		
		CO	CO_2	N_2O
0.5	1.6×10^{16}	240	260	240
2.5	8.1×10^{16}	48	52	49
5.0	1.6×10^{17}	24	26	24
10	3.2×10^{17}	12	13	12

Table 2.5 Average time between collisions based on Lennard-Jones rate constants

P(Torr)	ρ(cm^{-3})	dt/dN_{col} (ns)		
		CO	CO_2	N_2O
0.5	1.6×10^{16}	210	180	180
2.5	8.1×10^{16}	42	36	36
5	1.6×10^{17}	21	18	18
10	3.2×10^{17}	10	9	9

Chapter 3: Transient Spectroscopy and Collision Dynamics of Optically Centrifuged N_2O

Adapted from: H. M. Ogden, T. J. Michael, M. Murray, A. S. Mullin, Transient IR $(00^01 - 00^00)$ absorption spectroscopy of optically centrifuged N_2O with extreme rotation up to $J = 205$. *J. Quant. Spectrosc. Radiat. Transf.* **2020**, 246.

In this work, I collected and analyzed the transient absorption measurements of N_2O and edited the manuscript.

3.1 Introduction

In this chapter, new IR transitions are reported for optically centrifuged N_2O, and the collisional relaxation dynamics of the rotationally excited molecules is investigated. The main isotopologue of N_2O is rotationally excited to high-J levels with an optical centrifuge, and R-branch ν_3 transitions for levels with $J = 92$ to 205 are measured using high-resolution transient IR absorption spectroscopy. The collisional relaxation of super rotors with $J = 92$ to 205 is characterized by collecting polarization-dependent, Doppler-broadened line profiles. Transient absorption signals and Doppler profiles are converted to number densities. Doppler-broadened profiles reveal the amount of translational energy gained for in-plane and out-of-plane rotors in levels with $J = 92$ to 205. Polarization-dependent measurements reveal the orientational anisotropy of N_2O molecules prepared in the optical centrifuge and in the relaxation process.

Nitrous oxide, N_2O, is an important species in many environments, and high-resolution IR spectra have been reported previously for transitions with $J \leq 100$. In 1987, Toth reported IR transitions involving levels up to $J = 92$ at 300 K.[33] A number of studies have reported molecular constants for vibrational hot bands.[34–37] In 2011, the Mullin group extended the experimental observation of N_2O (00^00) ν_3 transitions to

$R100$ using optical centrifuge excitation and single-pass transient IR detection.[28] In 2014, Ting *et. al.* reported ν_3 transition frequencies up to $R100$ with 10 kHz precision.[38] Here, we extend the observed transitions to $R205$, which is made possible by the addition of a multi-pass IR detection cell to the optical centrifuge spectrometer.

In lieu of experimental observations of high-J transitions for N_2O, the high-temperature spectrum has been calculated with global modeling of line positions using an effective Hamiltonian with vibrational polyads.[39] This approach uses 138 parameters, and successfully reproduces accurate line positions for more than 37,000 measured line positions of 325 vibrational bands. Two high-temperature spectral databases, NOSD-1000 and HITEMP, include calculated IR transitions for high-J transitions of N_2O.[40,41] The maximum J-level listed in the HITEMP database is near $J = 100$.

High-J transitions, identified here as ν_{ext}, were extrapolated from low-J HITRAN energies.[42] Molecular constants were determined from data for $J \leq 90$ using an energy expansion in $J(J+1)$, where $E_n(J) = \nu_n + B_n J(J+1) - D_n(J(J+1))^2 + H_n(J(J+1))^3$ and n is the number of quanta in the ν_3 mode. The molecular constants in units of cm^{-1} are $\nu_0 = 0$, $B_0 = 0.41901$, $D_0 = 1.7609 \times 10^{-7}$, $H_0 = -1.6687 \times 10^{-14}$, $\nu_1 = 2223.757$, $B_1 = 0.41556$, $D_1 = 1.7547 \times 10^{-7}$, and $H_1 = -1.3351 \times 10^{-14}$. Line positions for the ν_3 transitions were also calculated up to $J = 205$ from the set of effective Hamiltonian parameters developed by V.I. Perevalov and coworkers.[39] Line positions from the effective Hamiltonian calculations are identified here as ν_{calc}. The observed transitions ν_{obs} are compared to both extrapolated line positions ν_{ext} and calculated line positions ν_{calc}.

A portion of the calculated R-branch transitions is shown in Figure 3.1, based on a 1000 K distribution. A band head is seen at $R116$ and transitions for higher-J levels lie between known lower-J transitions. This feature is used to measure new high-J transitions with spectral fingerprinting.

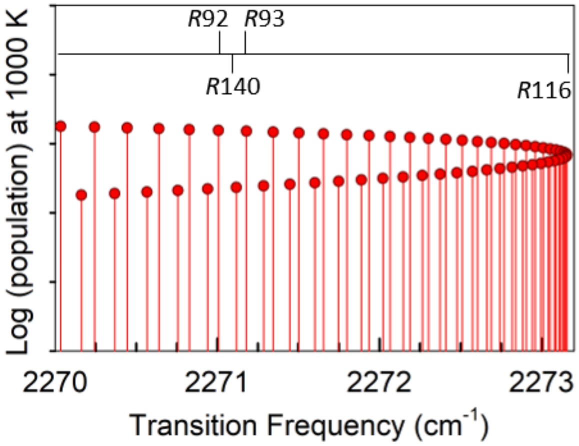

Figure 3.1 Calculated ν_3 R-branch transitions for high-J levels of N_2O. Transitions have been observed previously up to J = 100.

After identifying the line-center transitions, the collision dynamics for levels with $J = 92$ to 195 at a pressure of 5 Torr were investigated using polarization-dependent high-resolution transient IR absorption spectroscopy. Doppler-broadened line profiles were measured using vertical and horizontal IR polarizations and the time-dependent translational energy gains of in-plane and out-of-plane super rotors were determined. The transient IR absorption signals and Doppler profiles were used to calculate absolute number densities and to measure the orientational anisotropy of in-plane rotors during collisional relaxation.

3.2 Experimental Methods

Figure 3.2 shows a schematic diagram of the optical centrifuge transient IR absorption spectrometer. In the work reported here, an optical centrifuge was used to excite a 300 K sample of N_2O into extreme rotational levels with oriented angular momentum. High-resolution transient IR absorption spectroscopy of individual rotational levels was performed with a quantum cascade laser, a multi-pass detection cell, and active feedback control of the IR wavelength. The optical centrifuge spectrometer has been described in detail in Chapter 2, and the key features are given below.

3.2.1 Optical Centrifuge Excitation of N_2O $(00^0 0)$

The spectrum of the oppositely chirped pulses used to rotationally excite N_2O is shown in Figure 3.2a. The trap intensity is shown in Figure 3.2b as a function of instantaneous angular frequency Ω_{OC} where $\Omega_{OC}(t) = \frac{1}{2}\left(\omega_1(t) - \omega_2(t)\right)$. For these measurements, an optical coating flaw at $\lambda = 788$ nm led to a drop in trap intensity near $\Omega_{OC} = 5.0 \times 10^{13}$ radians s^{-1}. The highest rotational level measured here is $J = 205$, for which $E_{rot} > 17000$ cm^{-1} and rotational angular frequency is $\Omega_J = 3.2 \times 10^{13}$ radians s^{-1}.

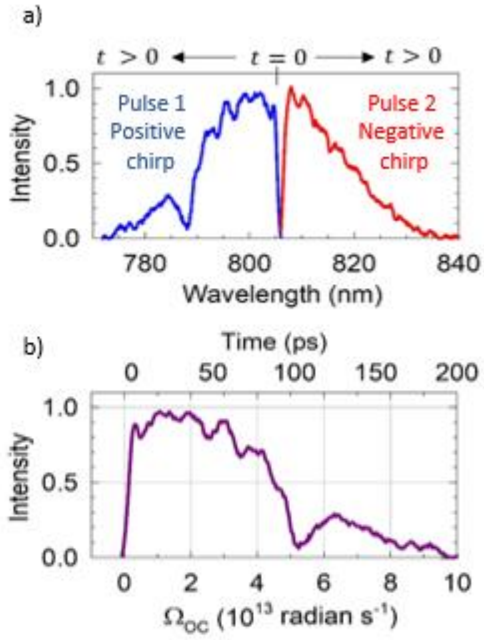

Figure 3.2 a) Spectrum of the chirped pulses that form the optical centrifuge. b) Intensity of the optical centrifuge field as a function of angular frequency.

3.2.2 High-Resolution Transient IR Absorption Spectrometer

The optical centrifuge is coupled to a high-resolution transient IR absorption spectrometer to measure the appearance of molecules in high-J levels and identify new spectral lines. New R-branch transitions were measured for states with $J = 140$ to 205, corresponding to the wavelength range of the IR laser output. The cell pressure was 5 Torr, for which the average time between collisions is approximately 20 ns. Collision numbers reported in this paper are based on a Lennard-Jones collision rate constant. Transient signals measured at $t = 60$ ns after the centrifuge pulse correspond to populations that have undergone 3 collisions on average. Spectroscopic grade N_2O (99.99% purity) was used.

IR transition frequencies were determined using high-resolution transient spectral fingerprinting and a wave meter with an effective resolution that is better than

$\Delta\nu_{wm} = 1 \times 10^{-3}$ cm^{-1}. The wavemeter is internally calibrated using a stabilized HeNe transition. Transient fingerprint spectra were recorded by starting at a known N_2O transition and stepping the IR frequency in steps of $\delta_\nu < 0.001$ cm^{-1}. The accuracy of the wavemeter readings was established by locking the IR probe laser output frequency to a transition involving a thermally populated N_2O state and comparing with known transition frequencies. The detector used in these experiments has a rise time of 50 ns.

Polarization-dependent Doppler-broadened line profiles were measured for N_2O with $J = 92$ to 195 levels. Transient signals were collected at discrete IR wavelengths as the probe laser was tuned across the line profile in approximately 40 steps. Doppler profiles at discrete times were fit to Gaussian functions and time-dependent translational temperatures were extracted from the widths of the fitted profiles.

3.3 Results

Here, the transition frequencies for N_2O $(00^01 - 00^00)$ R-branch transitions with $J =$ 140 to 205 using transient IR absorption spectroscopy are reported. Line positions were determined using spectral fingerprinting for four transitions. Line positions for 7 additional transitions were measured with the wavemeter. Polarization-dependent transient Doppler profiles were measured as a function of J to show how line widths are affected by optical centrifuge excitation and by collisions. Time-dependent line profiles give information about the collisional energy transfer and orientational anisotropy of N_2O super rotors.

3.3.1 Transient Spectroscopy of Optically Centrifuged N_2O

Figure 3.3a shows the transient absorption signal at line center for the $R140$ transition near 2271 cm^{-1}. The $R140$ transition frequency is between $R92$ and $R93$, as shown in the transient spectrum in Figure 3.3b. The spectrum is shown at three times following the centrifuge pulse. The fingerprint scans show that the $R140$ intensity increases from $t = 60$ to 120 ns and then decreases from $t = 120$ to 200 ns, whereas the $R92$ and $R93$ intensities increase ten-fold from $t = 60$ ns to 200 ns. The population changes arise from rotational energy transfer as the optically centrifuged molecules return to equilibrium populations through collisions. The initial increase in the $R140$ signal shows that the centrifuge pulse initially prepares molecules in levels higher than $J = 140$, and that population passes through this level during the relaxation process. The scan for $R140$ at $t = 60$ ns shows that the population in $J = 140$ is comparable to those for $J = 92$ and 93.

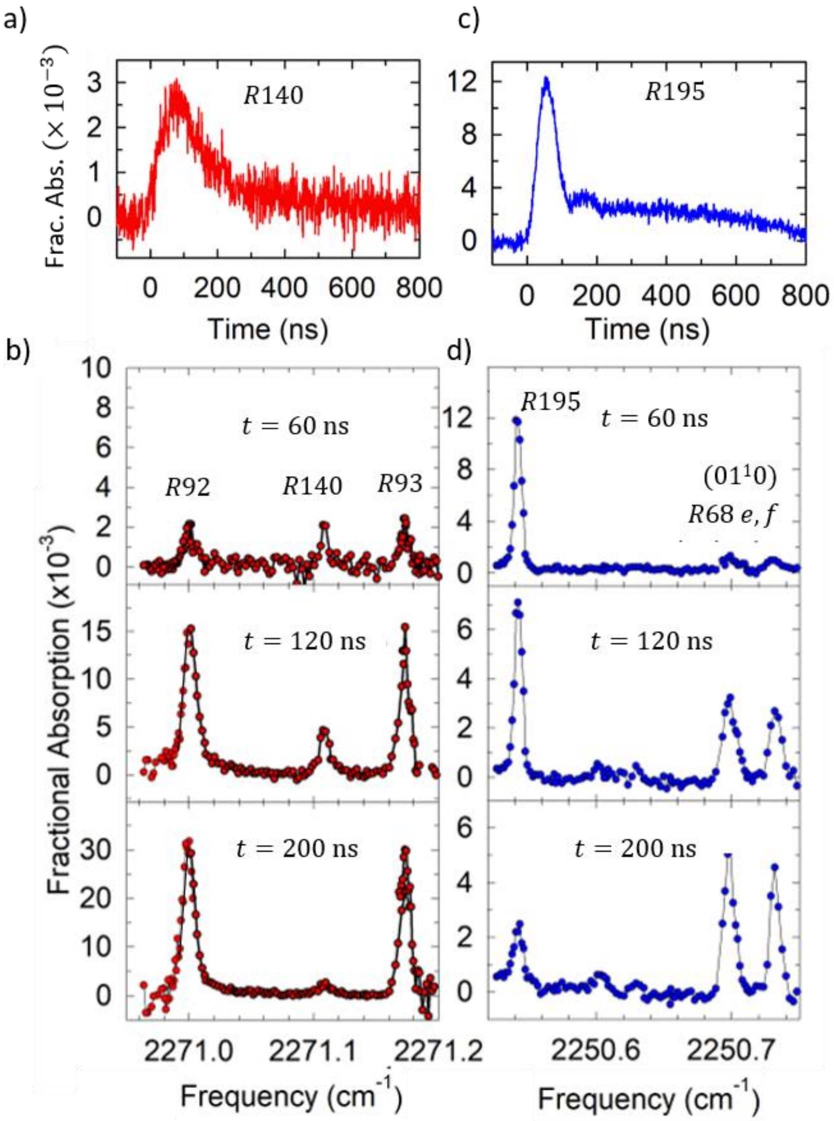

Figure 3.3 Line-center transient absorption measurements for a) $R140$ and c) $R195$ of N_2O. Transient fingerprint scans at $t = 60, 120$, and 200 ns after optical centrifuge excitation for b) $R140$ and d) $R195$.

Figure 3.3c shows the line center transient signal for $R195$. Two components are present: a prompt population that is formed in the centrifuge and a delayed population that comes from collisional cooling of centrifuged molecules. Spectral fingerprinting for $R195$ uses $R68\ e, f$ transitions of the $(01^11 - 01^10)$ band, as shown in Figure 3.3d. The $R195$ transition is most intense at $t = 60$ ns and has decreased by a factor of four at t = 200 ns. Population in the bending state increases by a factor of 3 over the same time period, as a result of collisional energy transfer. The time-dependent scans show how population is initially created in high-J levels with the optical centrifuge pulse and then collisions redistribute the energy into lower rotational levels and possibly vibrational levels that are not easily populated with traditional optical methods. The N_2O (01^10) bending mode can be populated by rotation-to-vibration/rotation energy transfer from the (00^00) state or by rotational excitation of (01^10) state that is 8% of vibrational distribution at 300 K. In other optical centrifuge experiments, we have detected transient absorption of CO_2 (03^30) $P43$, resulting from collisions; it is likely that the one quantum of the bend for N_2O is also populated by collisions.[43] Further evidence of the population inversion created by the optical centrifuge pulse is seen by comparing the peak intensities of $R140$ and $R195$. The peak intensity of $R195$ is 4-fold larger than that for $R140$.

Absolute line center frequencies ν_{obs} were determined through a combination of spectral fingerprinting and wavemeter measurements. Values of ν_{obs} are listed in Table 3.1 for eleven IR transitions. The uncertainty in line position is indicated by the number in parentheses. In all cases, the transition frequencies were determined by collecting transient absorption signals at discrete IR wavelengths. Line positions for 4 transitions were determined by measuring Doppler-broadened line profiles (described in the next section). These line positions are reported with an uncertainty of $\delta\nu_{obs} = \pm0.002$ cm^{-1}. Line positions for the remaining transitions were determined by scanning across the line profile in larger frequency steps than those used for the Doppler measurements and have a conservative uncertainty of $\delta\nu_{obs} = \pm0.01$ cm^{-1}.

Table 3.1 Observed, calculated, and extrapolated ν_3 R-branch N_2O line positions in (cm^{-1})

J	E_J [a]	ν_{obs}	ν_{calc} [b]	ν_{ext} (cm^{-1}) [c]
140	8202	2271.108(2)	2271.0908	2271.117
160	10677	2266.197(2)	2266.1457	2266.199
165	11344	2264.50(1)	2264.4482	2264.511
167	11617	2263.79(1)	2263.7173	2263.785
169	11892	2263.02(1)	2262.9569	2263.030
170	12031	2262.64(1)	2262.5655	2262.641
180	13464	2258.348(2)	2258.2443	2255.350
190	14973	2253.32(1)	2253.1800	2253.327
195	15756	2250.544(2)	2250.3687	2250.540
203	17049	2245.71(1)	2245.4827	2245.703
205	17380	2244.43(1)	2244.1865	2244.420

a. Energies of N_2O (00^00) levels based on effective Hamiltonian calculations from Ref 39.
b. Calculated transitions from Ref 39.
c. Transition frequencies based on extrapolation of a third order polynomial expansion from Ref 42.

The observed line positions ν_{obs} are compared with the predicted frequencies ν_{calc} and ν_{ext} in Figure 3.4. In all cases, the predicted frequencies are remarkably similar to the observed values, given the large values of J and rotational energy. The extrapolated frequencies using a simple polynomial expansion in $J(J+1)$ essentially match the observed values, and the calculated frequencies using an effective Hamiltonian show slight deviations with a small J-dependent increase.

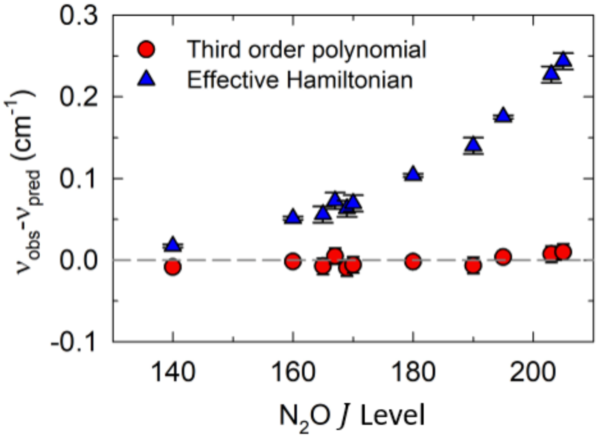

Figure 3.4 Deviations of observed and predicted frequencies for N_2O high-*J* *R*-branch transitions.

The predicted frequencies from the extrapolated data are based on a perturbative treatment of rotational energy with the rigid rotor model as the reference system. This model does not explicitly include all vibrational modes of the molecule. The deviations for the extrapolated frequencies are surprisingly small, given the simplicity of the model.

The effective Hamiltonian accounts for rotation, vibration, and their couplings, and is therefore a much more realistic model than the perturbative expansion.[39] This model also successfully predicts the observed transitions. The deviations from the observed transition frequencies correspond to less than one part in 10^4. At first glance, it is surprising that transitions from the effective Hamiltonian deviate from the observed transitions more than those for the simple perturbative expansion. It should be kept in mind, however, that data for high-*J* transitions were not available when the effective Hamiltonian calculations were performed. Being able to observe previously unknown rotational transitions with optical centrifuge excitation will allow for further refinement of sophisticated effective Hamiltonian modeling.

3.3.2 Transient Populations and Line Profiles of High-***J*** N_2O

The pulsed optical centrifuge excitation imparts large amounts of rotational energy to the sample, and gives rise to time-dependent line intensities and profiles. The time evolution of the spectral lines gives information about the energy relaxation process. Here we report the time evolution of J-dependent number densities and Doppler-broadened line profiles for $J = 140$ to 195 of N_2O. The orientational anisotropy of in-plane rotors is also discussed.

The full bandwidth optical centrifuge produces angular acceleration up to $\Omega_{max} = 6.0 \times 10^{13}$ radians s^{-1}, which is estimated to excite N_2O levels as high as $J = 385$ with rotational energy $E_{rot} > 60{,}000\ \mathrm{cm}^{-1}$. The reduced optical bandwidth centrifuge produces angular acceleration up to $\Omega_{max} = 5.0 \times 10^{13}$ radians s^{-1}, which corresponds to excitation to levels as high as $J = 310$ with rotational energy $E_{rot} > 45{,}000$ cm^{-1}. Figure 3.5 compares the line-center transient signal of $R195$ under the same conditions using full and reduced optical bandwidths, with all other experimental conditions being similar. The reduced bandwidth increases population in $J = 195$ by 12-fold.

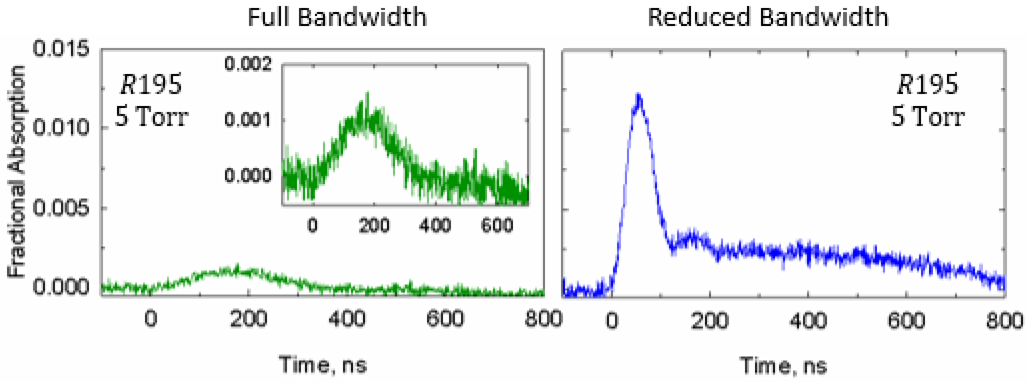

Figure 3.5 Transient signal of $J = 195$ that was populated using the full bandwidth centrifuge (left) and the reduced bandwidth centrifuge (right). The IR probe polarization was vertical.

Polarization-dependent spectroscopy was used to characterize the orientational anisotropy of optically centrifuged N_2O. Line-center transient absorption signals were collected for rotational levels with $J = 92\text{–}195$ using vertically and horizontally polarized IR light, as shown in Figure 3.6a. The raw transient signals were converted to in- and out-of-plane transients, as shown in Figure 3.6b. The intensities of the in-plane transient signals increase with J, indicating an inverted rotational population. The $J = 195$ transient signal is prompt, indicating that this state is populated directly by the optical centrifuge, whereas the $J = 92$ signal grows in more slowly due to collisional energy transfer. The in-plane signals are larger than the out-of-plane signals for higher-J levels showing a high degree of orientational anisotropy for molecules prepared by the optical centrifuge. In contrast, the in-plane and out-of-plane signals for $J = 92$ have comparable intensities, showing that they have comparable populations.

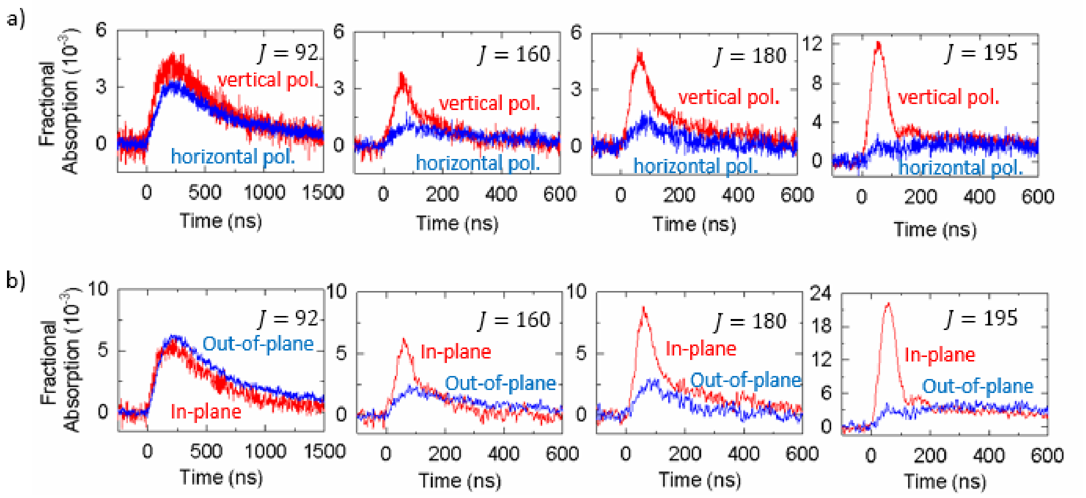

Figure 3.6 Line-center transient signals of $J = 92$ to 195 using vertical and horizontal polarized IR light. b) Transient signals were converted to in-plane and out-of-plane signals from measurements collected with vertical and horizontal polarized IR light.

State-specific number densities $N(J)$ were determined from transient absorption signals using $N(J) = -\ln(I_t/I_0)/(S_{296}(J)\, f(0)\, \ell) \cdot f_v f_J \cdot (\Delta\nu_{obs}/\Delta\nu_{296})$.

Values of $S_{296}(J)/f_v f_J$ for the high-J transitions were determined from known line strength values and transition dipole moments using the approach of Gamache and Rothman.[42] The line strength values have a fractional uncertainty less than 0.01. The fractional uncertainties in I_t/I_0 and $\Delta\nu_{obs}$ are each less than 0.10; the overall fractional uncertainty in $N(J)$ values is less than 0.21. Figure 3.7 shows in-plane (red) and out-of-plane (blue) N_2O (00^00) populations after $3-6$ collisions on average following the optical centrifuge pulse. After 3 collisions ($t =$ 60 ns), the population inversion of in-plane molecules created by the centrifuge pulse is clear, with the J =195 population nearly 3-fold larger than that for $J =$ 92. By 6 collisions ($t = 120$ ns), collisional energy transfer has nearly doubled the population in $J = 92$ and reduced the J =195 population by a factor of 4. The out-of-plane population is significantly smaller than the in-plane population and shows similar time-dependent shifts toward lower-J levels through collisional relaxation.

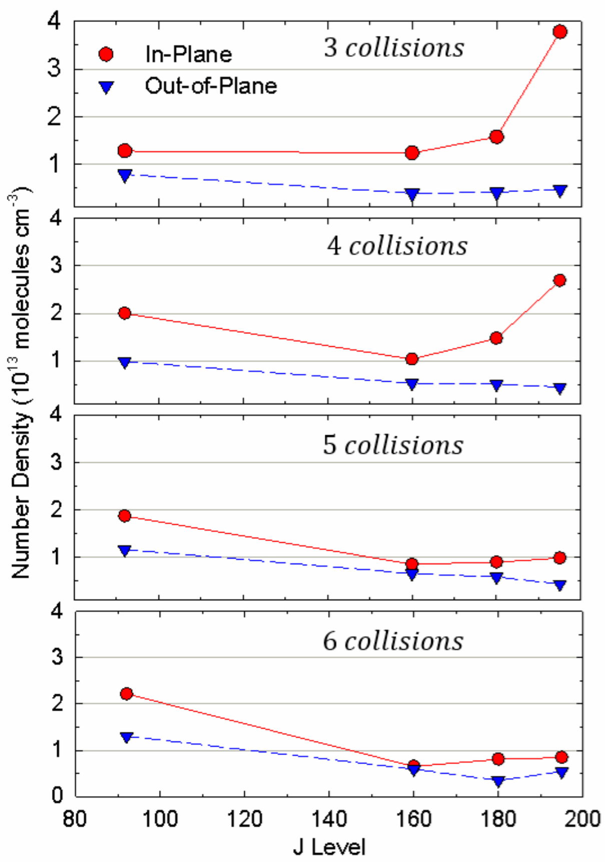

Figure 3.7 Number densities of in-plane (red) and out-of-plane (blue) N_2O with $J = 92$ to 195, showing collisional energy transfer from 3 to 6 collisions (t = 60-120 ns) after the optical centrifuge pulse.

The transient line profiles for the $R92$ to $R195$ transitions are Doppler-broadened, and give information about J-specific translational energy distributions. The in-plane (red) and out-of-plane (blue) Doppler profiles at $t = 60$ ns are shown in Figure 3.8, along with Gaussian fitting results. From $R92$ to $R195$, the line widths become narrower, showing that the average translational energy decreases with increasing J level. The peak intensities increase with J because of the population inversion.

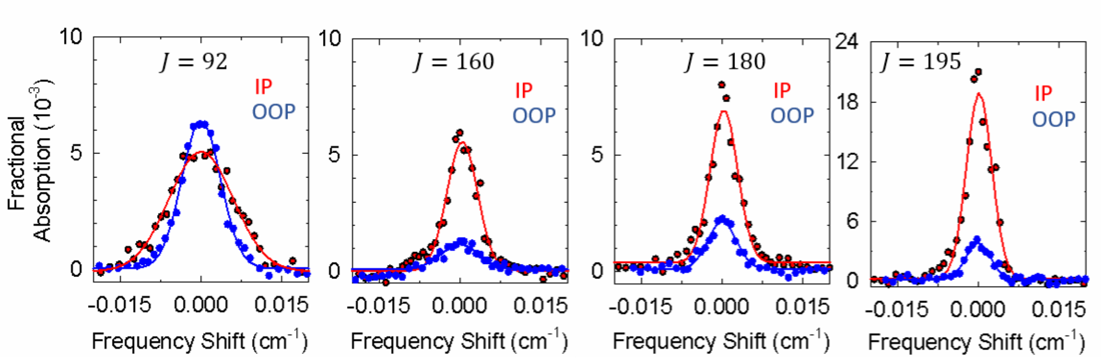

Figure 3.8 In-plane (IP, red) and out-of-plane (OOP, blue) Doppler-broadened line profiles for $J = 92 - 195$ at $t = 60$ ns.

The time-dependent in-plane and out-of-plane translational temperatures for N_2O with $J = 92 - 195$ are plotted in Figure 3.9a and 3.9b. For the levels measured, the translational temperatures are all greater than 300 K due to rotation-to-translational energy transfer. The J-dependence shows that higher-J levels gain less translational energy than the lower-J levels, for both in-plane and out-of-plane measurements. The time-dependence for in-plane rotors $J \geq 160$ shows that the translational energy gain increases as more collisions occur. The $J = 195$ translational energy remains relatively flat from $t = 40$ to 80 ns, corresponding to 2 to 4 collisions on average at a pressure of 5 Torr. Around $t = 90$ ns, or 5 collisions, the translational energy gain increases steadily for $J = 180$ and 195, while the translational energy gain increases rapidly for $J = 160$. Further down the collisional cascade $J = 92$ is populated with high translational energy near $T = 2500$ K at $t = 50$ ns (after 2 to 3 collisions). For the highest energy levels, the population is gone before the line profiles narrow, showing that rotational relaxation is faster than translational quenching. For the lower rotational levels, such as $J = 92$, collisions between bath molecules and super rotor molecules produce population with large translation after the first few collisions and continue to populate as the higher levels relax through lower levels. Interestingly, the in-plane and out-of-plane translational energies are similar for $J = 180 - 195$. The out-of-plane translational energy is initially hotter for $J = 160$ near $T = 1500$ K than the in-plane translation near $T = 600$ K. For $J = 92$, the out-of-plane translation is cooler than the in-plane translation at all times.

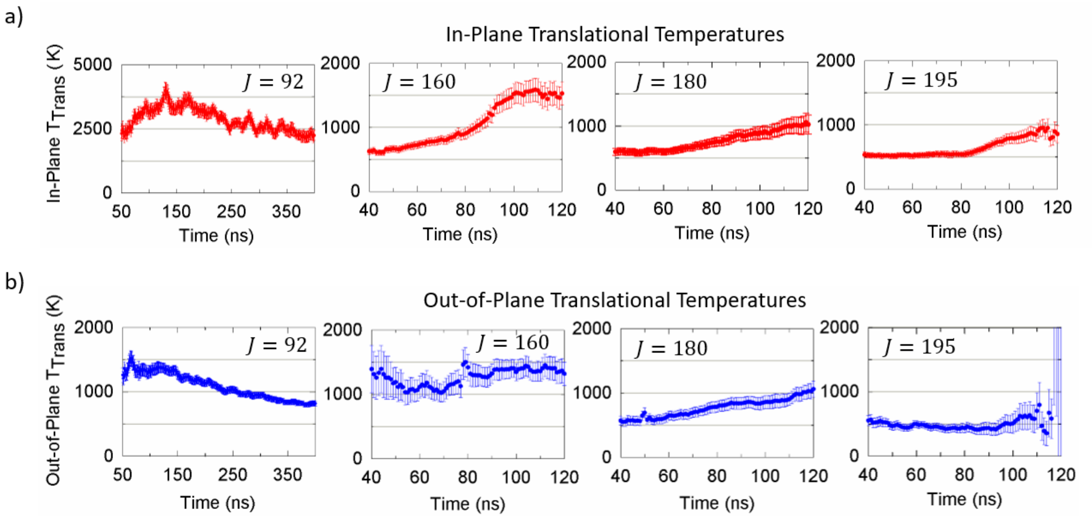

Figure 3.9 a) In-plane and b) out-of-plane translational energy over time for N_2O molecules with $J = 92 - 195$.

The observed J-dependent data in Figure 3.9 provide insight as to how collisions disperse the rotational energy of centrifuged molecules. Generally speaking, the relaxation of centrifuged molecules occurs by two limiting cases: resonant- and non-resonant energy transfer, depending on the J level of their collision partner. The amount of translational energy in the collision products increases based on the rotational energy difference of the colliding molecules.

In one case, near-resonant energy transfer occurs in collisions of two centrifuged molecules that involve $\Delta J = \pm 1$ transitions. In this case, ΔE_{up} and ΔE_{down} values are nearly equal in magnitude, leaving negligible energy available for translation. On the other hand, collisions of centrifuged molecules with low-J

molecules that have $\Delta J = \pm 1$, transitions result in large amounts of translational energy, because the rotational energy transfer is non-resonant. Because rotational energy scales roughly as J^2, lower-J levels gain more translational energy than ones that are closer to the initial levels prepared in the centrifuge. This behavior is clearly seen for the in-plane molecules in Figure 3.9a. Of course, J-changing collisions are not limited to $\Delta J = \pm 1$ and collision products will have low translational energies as long as the rotational energy transfer is resonant or near resonant. Furthermore, the observation of translational broadening even for $R195$ at $t = 60$ ns indicates that the optical centrifuge initially prepares N_2O molecules well above $J = 200$. It should be possible in future studies to observe N_2O transitions with $J > 200$ by extending the IR tuning range in our transient spectrometer.

The efficiency of energy transfer to occur from rotation-to-translation through collisions is examined by the timescales involved in the process. Two timescales are considered: the rotational period of the molecule $t_{rot} = 2\pi/\omega_{rot}$ and the duration of the collision t_{col}. The adiabaticity parameter a compares both timescales and is defined as

$$a = t_{col}/t_{rot} \tag{3.1}$$

For long interactions between two colliding molecules in which one completes many revolutions compared to the other, rotation-to-translation energy transfer is inefficient and the collision is considered adiabatic. This occurs when $a > 1$. When the timescales become comparable to, or faster than, the revolution of the molecule, then rotation-to-translation energy transfer is efficient, and the collision is considered sudden or impulsive. This situation occurs when $a \sim 1$ (or smaller).

Molecules with lower angular frequencies, such as $J = 92$ (1.45×10^{13} radians s^{-1}), rotate more slowly than a super rotor, and have longer collisional interactions times that lead to large translational energy gains, as seen in Figure 3.10. Molecules in $J = 160$ initially have translational energy near $T_{trans} = 500$ K at $t = 50$ ns and then steadily gain 900 K in translation by $t = 100$ ns. This large translational energy gain is characteristic of non-resonant, sudden collisions.

The data from Figure 3.9 were used to characterize the transition from the adiabatic to sudden collision regime for N_2O, as shown in Figure 3.10. At the earliest time in Figure 3.10a, molecules in $J = 92$ level are populated by non-resonant collisions between a bath molecule with a super rotor or a centrifuged molecule that fell out of the trap. The collision dynamics that populate the $J = 92$ level are sudden, and result from rotation-to-translation energy transfer. Molecules in levels with $J = 160$, seen in Figure 3.9a, undergo non-resonant collisions that result in translational energy gain. A range of interaction timescales for N_2O-N_2O collisions were determined as $t_{col} = 0.45$ ps to 0.26 ps by defining $a = 1$ to occur somewhere between $J = 92$ and 160 (Figure 3.10).

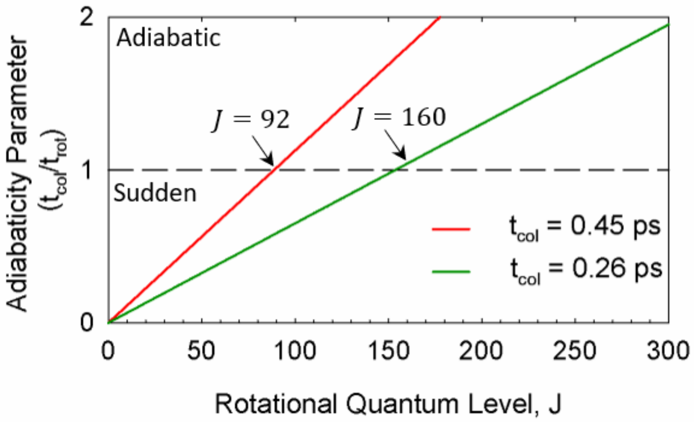

Figure 3.10 Adiabaticity curve for N_2O where $a = 1$ occurs at $J = 92$ and $J = 160$ and shown as a dashed line.

Figure 3.11 shows the time-dependent orientational anisotropy r for N_2O with $J = 92 - 195$ based on polarization-dependent absorption measurements. In each plot, the grey dashed line at $r = 1.00$ indicates a distribution with all molecules rotating in the xy-plane defined by the optical field of the centrifuge pulse. The line at $r = 0.33$ corresponds to an isotropic distribution of angular momentum orientations. The anisotropy values shown in Figure 3.11 increase for molecules that have higher angular momentum. Molecules in the $J = 195$ level initially have orientational anisotropy values of $r = 0.85$ at $t = 50$ ns (or 2.5 collisions on average). The high degree of orientational anisotropy indicates that most molecules in this level were directly created in the centrifuge and are spinning in the original plane of rotation. At $t = 50$ ns, molecules in lower-J levels, such as $J = 92$, have orientational anisotropy values of $r = 0.65$, which is closer to an isotropic distribution. By $t = 100$ ns, or 5 collisions on average, $J = 195$ has orientational anisotropy of $r = 0.79$. Molecules further down the collisional cascade with $J = 160$ initially have anisotropy values near $r = 0.77$ and decrease to $r = 0.65$ after 5 collisions. Interestingly, the anisotropy of the $J = 92$ level persists out to $t = 400$ ns (20 collisions) without returning to an isotropic distribution. This observation shows that high-J N_2O molecules tend to retain the projection of their angular momentum vector as they undergo collisional relaxation.

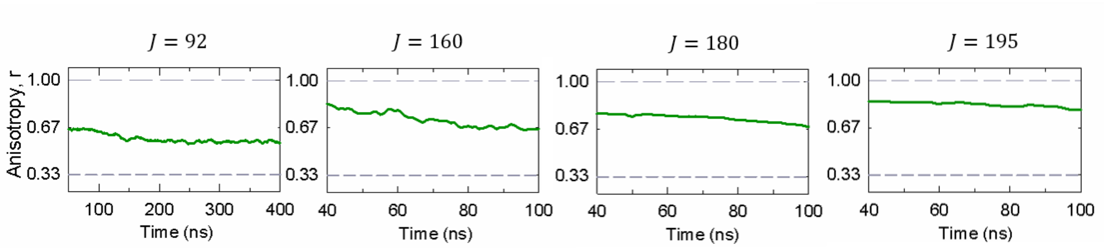

Figure 3.11 Orientational anisotropy r of in-plane super rotors as a function of time for rotational levels $J = 92 - 195$.

Super rotors prepared in the optical centrifuge behave as molecular gyroscopes, with angular momentum affecting the extent to which the molecules tend to retain their initial plane of orientation through collisions. The persistence in orientational anisotropy is associated with the change in tilt angle $d\varphi$ that is induced during a collision, as indicated in Equation 3.2

$$d\varphi = \frac{Kdt}{L} \,. \tag{3.2}$$

Here K is torque on the molecule from the collision and L is the molecule's classical angular momentum. For a N_2O molecule in $J = 195$, the maximum collision-induced tilt angle is $d\varphi = 9°$, based on a $300\,\text{K}$ collision with a relative velocity that is perpendicular to the plane of molecular rotation. For a molecule in $J = 92$, the maximum collision-induced tilt angle is $d\varphi = 19°$. Large amounts of angular momentum slow down orientational randomization. This behavior was observed in the Mullin group in a previous polarization-dependent study of CO_2 with $J = 76 - 100$.[44] Murray *et. al.* found that molecules in the $J = 100$ level have larger anisotropy values that persist for twice as long as molecules in $J = 76$. For a CO_2 molecule in $J = 100$, the maximum collision-induced tilt angle is $d\varphi = 12°$. The $J = 92$ level of N_2O has an angular frequency of $\Omega_{92} = 1.45 \times 10^{13}$ radians s^{-1} similar to the $J = 100$ level in CO_2 with $\Omega_{100} = 1.47 \times 10^{13}$ radians s^{-1}, but N_2O retains higher orientational anisotropy throughout the same number of collisions. CO_2 in $J = 100$ relaxes to isotropic orientations with anisotropy values of $r = 0.33$ after 20 collisions, whereas N_2O in $J = 92$ persists with orientational anisotropy of $r = 0.67$ throughout 20 collisions.

3.4 Conclusion

The work reported here demonstrates that the optical centrifuge is a powerful technique for populating high rotational levels without having to perform experiments under high temperature conditions. When coupled with high-resolution transient IR absorption probing, new transition frequencies for high-J levels can be measured within 0.01 cm^{-1}. Here, new R-branch transitions for N_2O $(00^01 - 00^00)$ absorption up to $R205$ are reported. These measurements greatly extend previous observations of transitions up to $R100$, and provide a direct comparison with a theoretical model of high temperature spectral lines, thereby helping to validate and refine the model.[28,33] Polarization-dependent Doppler broadened line profiles of $J = 92 - 195$ show small translational energy gain for collisions that result in near-resonant energy transfer and large translational gain from non-resonant collisions. Orientational anisotropy of in-plane super rotors reveal high anisotropy near $r = 0.85$ for molecules with $J = 195$, showing a high degree of orientated angular momentum for this level. The persistence in orientational anisotropy over time is attributed to the gyroscopic behavior of molecular super rotors. In a broader sense, the information gained from this study will enhance tools for characterizing remote and high temperature environments and for modeling molecules in extreme rotational levels.

Chapter 4: State-Resolved Rotational Distributions and Collision Dynamics of CO Molecules Made in a Tunable Optical Centrifuge

Adapted from: T. J. Michael, H. M. Ogden, A. S. Mullin, State-Resolved Rotational Distributions and Collision Dynamics of CO Molecules Made in a Tunable Optical Centrifuge. *J. Chem. Phys.* **2021**, 154.

I collected and analyzed the polarization-dependent transient absorption measurements of CO and prepared the manuscript.

4.1 Introduction

Here we control the rotational excitation of CO and explore, using high-resolution, polarization-dependent transient IR spectroscopy, how the nascent rotational distribution is affected by the time-dependent shape of the optical trap. Time-dependent population measurements were performed to characterize how the nascent distribution and the orientational anisotropy are relaxed by collisions. Transient Doppler line profiles provide information about the state-dependent translational energy gain from rotational energy transfer.

We have reported two previous studies on collisions of optically centrifuged CO. The first study used high-resolution transient IR absorption probing in a single-pass detection configuration to characterize the collision-induced population changes of individual rotational levels with $29 \leq J \leq 39$.[45] Overall decay rates for these levels increase with increasing J, consistent with the initial creation of an inverted rotational distribution, followed by a cascade of collisional cooling. No population was detected in levels with $J > 39$ because collisional cooling of higher J levels was faster than the instrument response time. Doppler profiles for the $J = 29$ level indicated that the rotational energy transfer to this level involves large $|\Delta J|$ events, based on line broadening corresponding to a translational temperature of $T_{trans} = 800$ K after 10 gas kinetic collisions.

A second study of optically centrifuged CO measured transient population in the $J = 62$ to 73 levels, made possible by the implementation of a multipass detection scheme.[46] At pressures of 25 to 100 Torr and optical pulse intensities up 2.0×10^{13} W/cm^{-2}, emission from C_2 was observed following the pulsed excitation of CO, indicating that reactions of excited CO lead to formation of C_2. By controlling the polarization of the chirped optical pulses, we showed that rotational energy in triplet CO inhibits bimolecular reactions that lead to the formation of C_2. Two shaped pulse polarizations were used to rotationally excite the CO molecules: an optical centrifuge and a dynamic polarization grating. The dynamic polarization grating consists of two pulses with orthogonal linear polarization and drives molecules into high rotational levels through sequential Raman transitions. The optical centrifuge creates an ensemble with oriented angular momentum, whereas as the dynamic polarization grating does not. For optical centrifuge excitation, population in the $J = 62$ to 73 levels is as much as five time larger than for excitation with a dynamic polarization grating, and the C_2 reaction yields are correspondingly reduced by a factor of two. Emission is not observed below pressures of 10 Torr. The studies reported here on the near-nascent distributions of optically centrifuged CO were performed at pressures of 2.5 to 5.0 Torr under conditions in which C_2 emission is undetectable.

In this chapter, two different optical centrifuge bandwidths are used to excite CO molecules rotationally. When the full bandwidth is used, the highest rotational level observed is $J = 80$, with an energy near $12{,}300$ cm^{-1} and an angular frequency of $\Omega_J =$

5.8×10^{13} radians s^{-1}. When the bandwidth is limited by blocking a portion of the positively chirped pulse, the highest rotational level observed is $J = 67$, with an energy near 8600 cm^{-1} and an angular frequency of $\Omega_J = 4.8 \times 10^{13}$ radians s^{-1}. In these studies, high-resolution transient IR absorption spectroscopy is used to measure the distribution of optically centrifuged molecules as a function of optical centrifuge bandwidth. Polarization-dependent transient IR spectroscopy is used to measure the orientational anisotropy of the centrifuged molecules, and Doppler-broadened line profiles are used to determine the translational energy of the centrifuged molecules. This work investigates the formation and relaxation mechanisms of CO molecules in extreme rotational levels with orientated angular momentum that are well beyond thermally accessible levels.

4.2 Experimental Details

The details of the optical centrifuge laser system coupled to a high-resolution transient IR absorption spectrometer has been described in Chapter 2. The optical pulse intensity at the sample cell is 2.8×10^{13} W/cm^{-2} for 2.5 Torr measurements and 2.5×10^{13} W/cm^{-2} for 5 Torr measurements. The IR probe transitions are individual R-branch transitions of the $(1-0)$ vibrational band. IR transition frequencies and absorption strengths are reported in the HITRAN database up to $J = 58$.[42] Guelachvili and coworkers reported CO transitions up to $J = 93$.[47,48]

Transient absorption signals are collected using a liquid-nitrogen-cooled InSb detector with an amplifier with a rise-time of 50 ns. The IR light is wavelength-modulated at 100 Hz and the IR frequency is controlled by active feedback stabilization using a tunable confocal etalon, a second InSb detector, and a lock-in amplifier. The IR modulation increases the IR frequency spread to less than 2.3×10^{-4} cm^{-1} (7 MHz) which is more than a factor of 20 smaller than the full-width half-maximum linewidths of 5.2×10^{-3} cm^{-1} (155 MHz) for the probe transitions at 300 K. The line-center frequencies of the IR probe transitions are determined with the combination of an IR wavemeter and by locking the IR laser to an etalon fringe, tuning the etalon across the line profile, and finding the maximum transient signal.

Doppler-broadened line profiles were collected at a pressure of 5 Torr for nine different rotational levels with $29 \leq J \leq 80$ using vertical IR polarization, which is parallel to the plane of the centrifuged molecules. Doppler profiles were measured by collecting fractional absorption signals at approximately 40 discrete IR frequencies. The IR wavelength was locked to a fringe of a tunable etalon and transient absorption signals were collected at individual wavelengths as the etalon was tuned in frequency steps of $\Delta\nu = 0.001$ cm^{-1} across an IR transition. Doppler profiles were fit to Gaussian functions and time-dependent translational temperatures were determined from the full widths at half maximum.

The IR light is linearly polarized, and the polarization angle relative to the xy-plane is controlled with a half-wave plate. Orientational anisotropy measurements were made with parallel and perpendicular configurations, relative to the xy-plane. Spectroscopic grade CO (99.99% purity) was used in this study reported. Diffusion times across the excitation and probe volume in these experiments is longer than 1 μs.[45]

4.3 Results and Discussion

In this study, the nearly-nascent distributions of optically centrifuged CO molecules under two different optical centrifuge bandwidths and pressures are investigated using high-resolution transient IR absorption spectroscopy. The first configuration uses the full optical bandwidth and a gas pressure of 2.5 Torr. The second configuration uses reduced optical bandwidth and a gas pressure of 5 Torr. The orientational anisotropy of the samples is measured using polarization-dependent IR probing, and the time-dependent distributions reveal how collisions relax the optically centrifuged molecules. Doppler-broadened line profiles of mid- and high-J levels provide a measure of the rotation-to-translation energy transfer that accompanies the collisional relaxation of optically centrifuged molecules.

4.3.1 Controlling the Optical Trap

Figure 4.1 shows the spectra of the pulses used in this study, along with the angular frequency and the relative field intensity associated with each spectrum. Spectrum 1 (S1) uses the full Ti:Sapphire bandwidth, shown in Figure 4.1a. Figure 4.1b shows that Spectrum 2 (S2), which has reduced optical intensity at 788 nm in the positively chirped pulse resulting from the addition of a reflective notch filter. The angular acceleration of the optical centrifuge trap relies on the simultaneous presence of both pulses. By reducing intensity at a selected wavelength range in S2, the angular acceleration of molecules in the trap is interrupted. The centrifuged molecules are therefore released from the trap with lower rotational energy than would have been achieved with the full trap bandwidth.

Figures 4.1c and 4.1d show the relative intensities of positively chirped pulse for S1 and S2, respectively, as a function of the instantaneous optical centrifuge angular frequency Ω_{OC}. The insets show the slope of each optical trap as the trap intensity drops toward zero. The intensity of the S1 trap decreases smoothly in time, with a negative fall-off slope of $\beta_1 = 0.16$ per 10^{13} radians s^{-1} out to $\Omega_{OC} = 7 \times 10^{13}$ radians s^{-1}. The intensity fall-off for the S2 trap starting at $\Omega_{OC} = 4 \times 10^{13}$ radians s^{-1} is over three times steeper, with a negative slope of $\beta_2 = 0.51$ per 10^{13} radians s^{-1}. In this chapter, I investigate how the nascent distribution is affected by the optical pulse in the fall-off region.

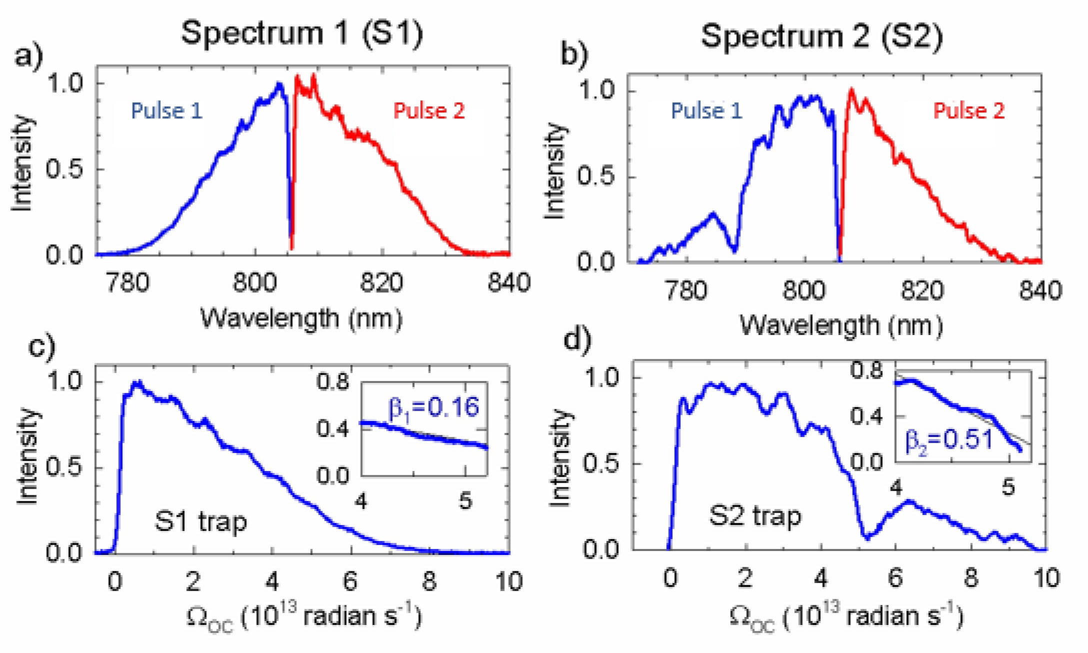

Figure 4.1 Chirped pulse spectra for a) the full bandwidth, Spectrum 1 (S1), and b) the reduced bandwidth trap, Spectrum 2 (S2). Angular frequency profiles of c) the S1 trap, and d) the S2 trap. The insets show that the trap intensity fall-off slope is nearly three times larger for S2 than for S1.

4.3.2 Polarization-Dependent Spectroscopy of Optically Centrifuged CO

Polarization-dependent, high-resolution transient IR absorption spectroscopy was used to probe the $J = 29$ to 80 rotational levels to characterize the orientational anisotropy of optically centrifuged CO molecules. Line-center transient IR signals were collected with vertical and horizontal IR probing that is parallel ($t_{\parallel}$) and perpendicular ($t_{\perp}$) to the plane of molecular rotation, as shown in Figure 4.2a for the $J = 70$ level prepared with the S1 trap, and in Figure 4.2b for $J = 62$ made in the S2 trap. Transient signals were converted to in-plane (t_z) signals for molecules rotating in the *xy*-plane and out-of-plane ($t_x + t_y$) signals for molecules rotating in the *z*-plane. The in- and out-of-plane transients were fit to exponential decays starting at 100 ns, shown in the right-hand plots of Figure 4.2, and the fit parameters were used to characterize the orientational anisotropy and the collisional relaxation of the centrifuged molecules. Line-center signals ($t_{\parallel}, t_{\perp}, t_z$ and $t_x + t_y$) were converted to integrated parallel ($p_{\parallel}$), perpendicular ($p_{\perp}$), in-plane (p_z), and out-of-plane ($2p_x$) signals using transient Doppler-broadened line profiles that are presented in a later section.

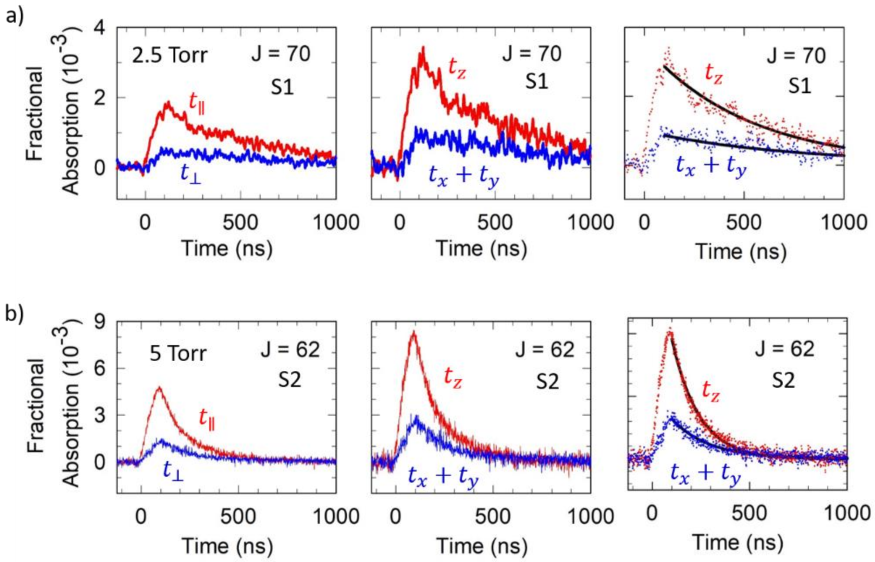

Figure 4.2 Polarization-dependent transient IR absorption signals of CO in a) $J = 70$ prepared in the S1 trap at 2.5 Torr, and b) $J = 62$ made in the S2 trap at 5 Torr. For both rotational levels, the left-hand plot shows the parallel and perpendicular transient signals, the center plot shows in- and out-of-plane signals, and the right-hand plot shows the exponential fitting result starting at $t = 100$ ns.

Polarization-dependent transient spectra were collected for CO in $J = 70 - 75$ using the S1 trap at a pressure of 2.5 Torr. The average time between gas-kinetic collisions for these data is 42 ns, based on a Lennard-Jones collision rate constant of $k_{LJ} = 2.9 \times 10^{-10}$ cm^3 molecule^{-1} s^{-1}. Additionally, measurements were made for CO with $J = 29 - 67$ using the S2 trap at a pressure of 5 Torr. In this case, the gas-kinetic collision time is 21 ns. The transient signals peak near $t = 100$ ns, and represent the nearly nascent distribution of optically centrifuged molecules. The observed decay rates for the high-J levels scale with pressure. At 5 Torr, transient signals are essentially gone by $t = 500$ ns, whereas transients collected at 2.5 Torr often persist to $t = 1$ μs and beyond.

To characterize the orientational anisotropy of the centrifuged molecules, the line-center signals were converted to integrated in-plane (p_z) and out-of-plane ($p_x +$

p_y) signals using transient Doppler-broadened line profiles. Figures 4.3a and 4.3b show in-plane (IP) and out-of-plane (OOP) signals at t =100 ns for the S1 and S2 traps, respectively. Substantially more in-plane molecules are observed for levels with $J \geq 48$ in both optical traps. The S1 data focus on the high-J tail of the centrifuged molecules. The S2 data span a larger range of J-levels and the population inversion of in-plane rotors is evident. The reduced bandwidth in the S2 trap limits the highest observed centrifuged level to $J = 67$, whereas population is detected to $J = 80$ with the full bandwidth trap.

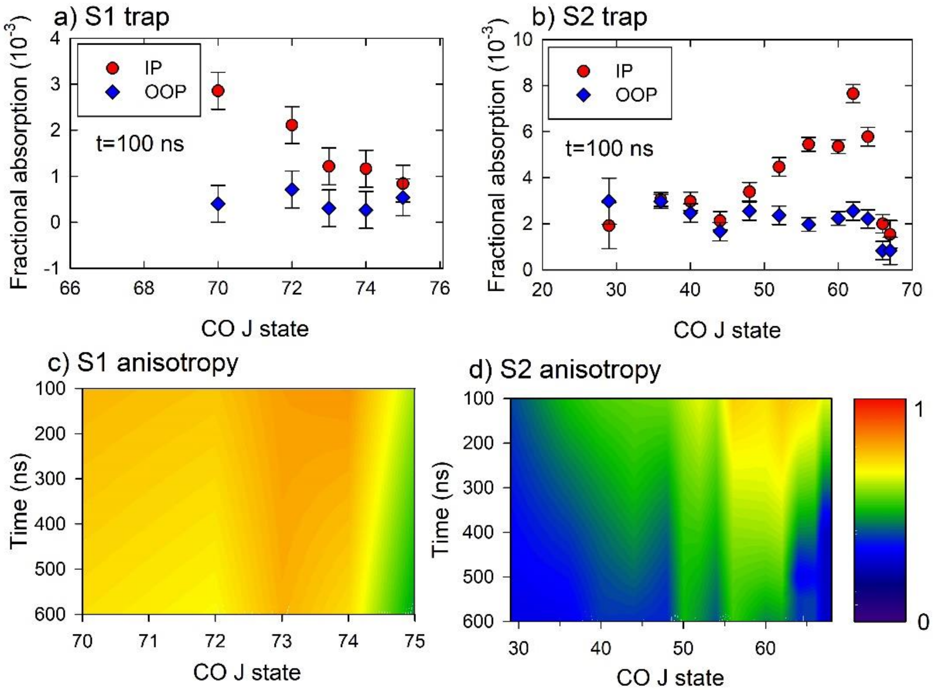

Figure 4.3. In-plane (IP) and out-of-plane (OOP) signals at $t = 100$ ns following the centrifuge pulse for CO in a) $J = 70 - 75$ prepared in the S1 trap at 2.5 Torr pressure, and b) $J = 29 - 67$ prepared in the S2 trap at 5 Torr pressure. Heat maps of the time-dependent orientational anisotropies for the c) S1 and d) S2 bandwidths, based on the CO levels measured in a) and b).

Figure 4.3b shows that the in-plane and out-of-plane S2 data for CO rotational levels with $J \leq 44$ have comparable intensities and are relatively independent of J. Transient population in these levels comes both from molecules that have fallen out of the trap and molecules have undergone collisions with high-J molecules. It is not surprising that this subset of molecule shows little difference in their orientational polarization, because they were either not held very tightly by the trap or were formed through impulsive collisions.

Orientational anisotropy values were determined for the centrifuged molecules as a function of J and time for both traps. Figures 4.3c and 4.3d show heat maps of the orientational anisotropies for CO molecules prepared in the S1 and S2 traps respectively, starting at $t = 100$ ns. At the earliest time, the peak anisotropy is near r $=$ 0.8 for the S1 trap and is just above $r = 0.7$ for the S2 trap. Both sets of data show high anisotropy values for a range of J levels that are produced in the optical centrifuge: $J = 70$ to 74 for the S1 trap and $J = 55$ to 65 for the S2 trap. At some point in the pulse, the intensity of the optical field is not large enough to continue holding the molecules and the centrifuged molecules are released from the trap with a high degree of rotational orientation. In contrast, molecules with $J \leq 44$ that are populated primarily as a result of falling out of the trap or through collisions have anisotropy values closer to the isotropic limit of $r = 1/3$.

The heat maps in Figure 4.3 show that large orientational anisotropies for the high-J levels persist for many collisions, highlighting the gyroscopic behavior of optically centrifuged molecules. For the S1 data, just over two gas kinetic collisions have taken place at $t = 100$ ns and the anisotropy values remain near $r = 0.8$ for the $J = 70$ to 74 levels at $t = 600$ ns, corresponding to 14 gas kinetic collisions. For the S2 data, fewer than 5 gas kinetic collisions have taken place at $t = 100$ ns and the peak anisotropy values remain near $r = 0.7$ for the $J = 55$ to 65 levels until $t = 400$ ns, or ~ 19 gas kinetic collisions. By $t = 600$ ns, or ~ 28 collisions, the peak anisotropy values are near $r = 0.5$ for the S2 data. Similar to macroscopic gyroscopes, molecules with large amounts of rotational angular momentum tend to resist orientational relaxation through collisions because collision-induced angle changes are inversely proportional to the rotational frequency Ω_J and J. The result is that average thermal collisions of CO in the $J = 10$ rotational level result in a 90° tilt to the molecule's angular momentum vector, whereas a similar collision with CO in the $J = 70$ rotational level leads to a 13° tilt. In this way, molecules that are centrifuged to high-J levels retain their nascent rotational orientation longer than molecules in lower-J levels and those populated through collisions.

4.3.3 Distribution of Optically Centrifuged CO: Optical Bandwidth Dependence

Additional transient absorption measurements were made to characterize how the distribution of centrifuged molecules is affected by changing the fall-off slope of the optical trap. Populations of individual CO J levels were determined for the two optical centrifuge bandwidths based on parallel polarized transient IR absorption measurements, CO IR absorption strengths, and an absorption path length of $\ell = 0.1$ cm. A description of the procedure for calculating number densities is given in Chapter 2.2. The population distribution at $t = 200$ ns for the S1 trap is shown in Figure 4.4a as a function of the trap angular frequency, and the distribution at $t =$

100 ns for the S2 trap is shown in Figure 4.4b. In both cases, the distributions have undergone approximately 5 gas-kinetic collisions. Both distributions have a maximum in-plane population near $J_{max} = 62$, followed by reduced population in higher J-levels, indicating that the trap intensity is dropping and releasing the centrifuged molecules. Figures 4.4a and 4.4b also show the respective trap intensity, which has been scaled to the population in the J-level just above J_{max} where the fall-off begins. The high-J tail of the in-plane rotational population distributions mimic the trap intensity profiles. The full bandwidth trap leads to a monotonic decrease in population from J_{max} to $J = 80$. In comparison, the reduced bandwidth trap shows a much sharper reduction in population, extending from J_{max} to $J = 67$.

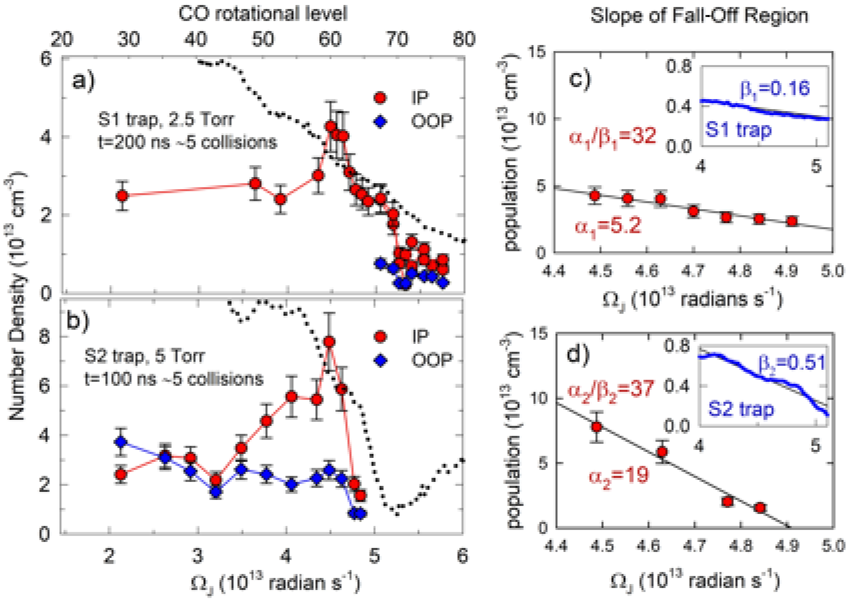

Figure 4.4 Distributions of optically centrifuged CO molecules using a) the S1 full bandwidth trap and b) the S2 trap. Red circles indicate population of IP-rotors and blue diamonds indicate OOP-rotors. The trap intensity is indicated by the dotted line. The slope of the IP population c) for the S1 trap and d) for the S2 trap is compared to the slope of the trap in the fall-off region.

The correlation of the CO population with the trap intensity profile in the fall-off region is further explored by comparing the slopes α_1 and α_2 of the population fall-off, which are shown in Figures 4.4c and 4.4d for the S1 and S2 trap, respectively, along with the trap fall-off slopes β_1 and β_2. The ratio of $\alpha_1/\beta_1 = 32$ is similar to $\alpha_1/\beta_1 = 37$, showing that the high-J distribution of centrifuged molecules correlates to the shape of the trap intensity.

4.3.4 Collisional Relaxation of Optically Centrifuged CO

The time evolution of the distribution of molecules centrifuged in the S1 trap is explored here. Figure 4.5 shows the J-dependent distribution of CO with $J = 29$ to 80 at $t = 100$, 200, and 400 ns following the centrifuge pulse. The in-plane populations (red circles) are much larger than the out-of-plane populations (blue diamonds) and decrease without a J-shift in the peak of the distribution. The relative trap intensity (shown as a dotted line) is scaled to the peak of the CO distribution at $t = 100$ ns. The distribution at 100 ns has undergone just over 2 gas kinetic collisions. At $t = 200$ ns, the population in levels with $J \geq 50$ uniformly shows a 15% decrease relative to the population at $t = 100$ ns. At $t = 400$ ns, an additional 30% decrease is seen relative to the $t = 200$ ns population. The amplitude of the distribution is reduced through collisions as molecules move into lower-J levels. Lower energy levels also show population loss. Population in $J = 29$ initially drops by 20% between $t = 100$ ns and 200 ns, then is fairly constant out to 1 μs, as molecules from higher-J levels relax through collisions into lower-J levels.

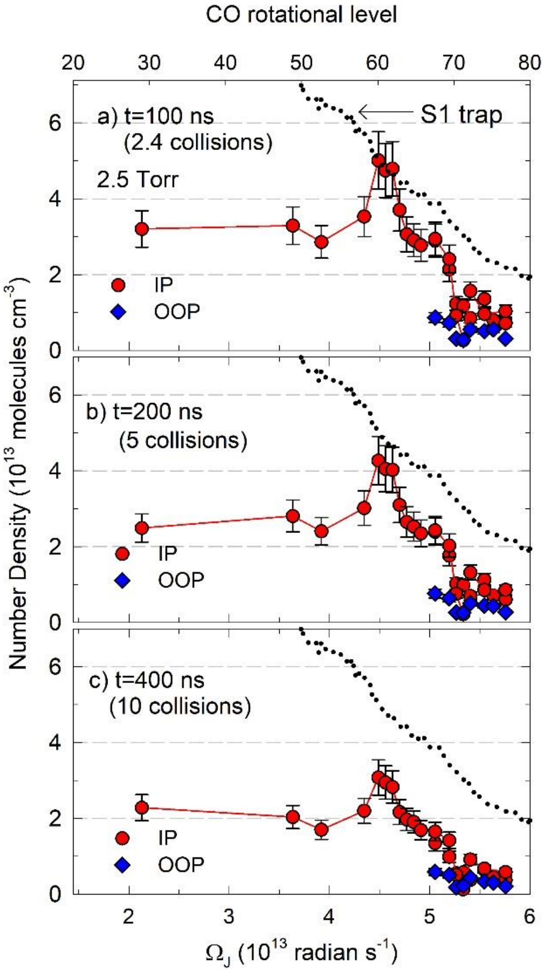

Figure 4.5 Time snapshots of the IP and OOP distribution CO molecules at a) $t = 100$ ns, b) 200 ns, and c) 400 ns after the centrifuge pulse. The dotted black line is the S1 trap intensity scaled to the maximum population at 100 ns.

The rotational distribution broadens slightly with collisions. Figure 4.6a shows the time-dependent populations of $62 \leq J \leq 80$ along with linear fitting results and population changes for individual levels between $t = 100$ ns and 200 ns and between $t = 200$ ns and 400 ns. The slope decreases in magnitude over time, as in Figure 4.6b, showing that population is moving from the peak of the distribution to higher J levels, but that the changes in J are relatively small. We do not see evidence that collisions move population into levels higher than $J = 80$, showing that the overall relaxation process predominantly involves collisions that move population to lower-J levels.

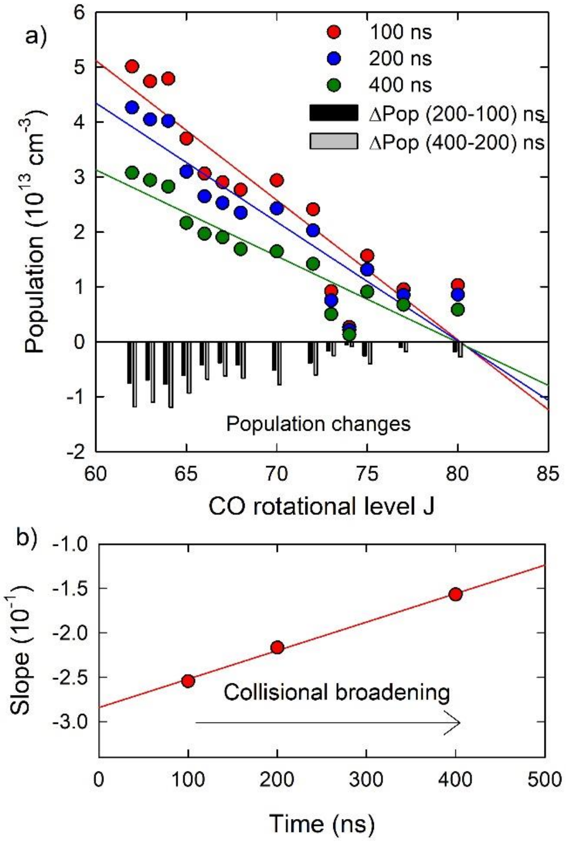

Figure. 4.6 a) Population of CO levels with $62 \leq J \leq 80$ from Figure 4.5 at $t = 100, 200$ and 400 ns, along with unconstrained linear fitting results. The bar graph shows changes in population for $\Delta t = (200 - 100)$ns and $\Delta t = (400 - 200)$ns. b) The magnitude of the slope of the rotational population distribution decreases with time, showing that collisions broaden the nascent rotational distribution and energy transfer occurs with a range of $|\Delta J|$ values.

4.3.5 Translational Energy Distribution of Optically Centrifuged CO Molecules

Translational energy distributions were obtained from transient Doppler-broadened line profile measurements. Line profiles for the J = 29 and J = 62 to 80 rotational levels were collected using parallel IR probing in the S1 optical trap at a pressure of 5 Torr. The Doppler-broadened line profiles were fit to Gaussian functions and time-dependent translational temperatures were extracted from the profile widths. Figure 4.7 shows transient Doppler profiles for the $J = 29, 62, 68,$ and 75 levels at $t =$ 120 ns after the centrifuge pulse. As J increases, the Doppler profiles narrow, corresponding to lower translational temperatures for the higher J-levels. At $t = 120$ ns, the $J = 29$ level has a translational temperature near $T_{trans} = 700$ K while the $J = 75$ level has a temperature near $T_{trans} = 240$ K.

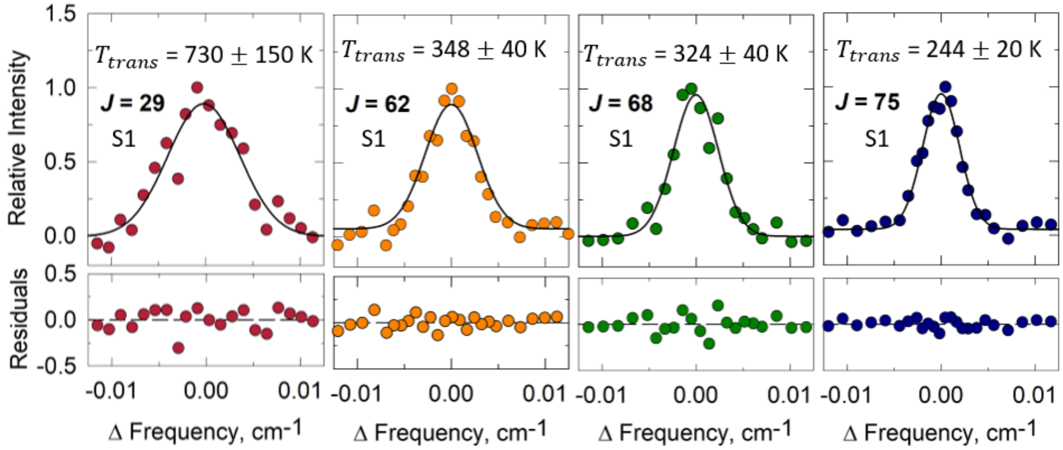

Figure 4.7. Transient Doppler-broadened line profiles for CO with $J = 29, 62, 68,$ and 75 at $t = 120$ ns after the centrifuge pulse. Residuals for the Gaussian fit are shown below each profile.

The time-dependent temperatures shown in Figure 4.8a-c highlight the differences between low and high-J levels formed during and after the optical centrifuge pulse, as does the heat map generated from the $J = 29$ and $J = 62 - 80$ Doppler profiles shown in Figure 4.8d. The high-J levels have low initial translational temperatures that remain low for many collisions. These data are evidence that the optical centrifuge selectively imparts rotational, but not translational, energy to the trapped molecules. Here, the lowest translational temperature ($T = 240$ K) is observed for the $J = 75$ level, for which the angular frequency is near the upper limit of the S1 optical trap. Line profile measurements for low-J levels show that molecules with low velocities are selectively trapped in the optical field prior to angular acceleration, thereby leading the highest J-levels to have the lowest translational energies in optical centrifuge excitation.[50] In collisions, low translational energies are the signature of resonant and near-resonant rotational energy transfer which involve small energy gap values. The low T_{trans} data in Figure 4.8d show the importance of such resonant processes for the $J > 50$ levels of CO. In contrast, the $J = 29$ level is created within the first 5 gas-kinetic collisions with significant amounts of translational energy that is eventually relaxed through collisions. This observation shows that the lower-J levels are initially populated through impulsive collisions with centrifuged molecules and that subsequently, translational cooling occurs as does population transfer of molecules from higher-J levels with narrower velocity spreads.

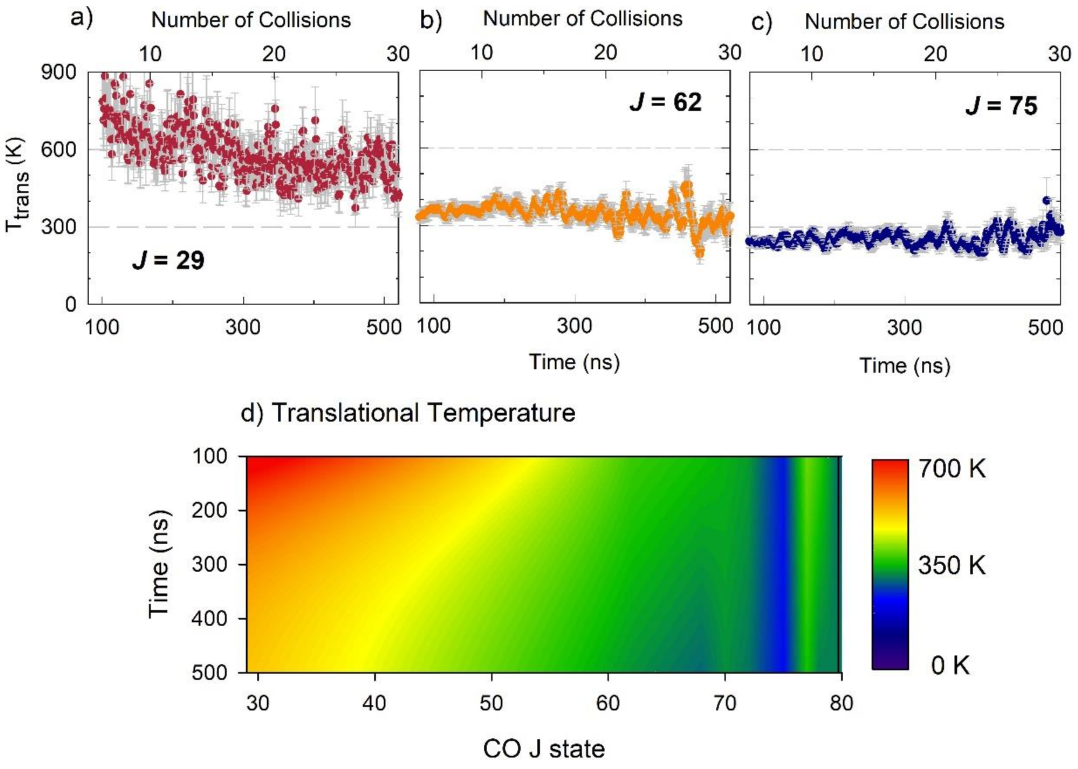

Figure 4.8 a) Time-evolution of translational temperatures for CO J = $29, 62$, and 75. b) Heat map of time-dependent translational temperatures based on transient Doppler profiles measured for the $J = 29$ and the $J = 68$ to 80 levels.

4.3.6 Decay Kinetics of Optically Centrifuged CO Molecules

Transient signals such as those shown in Figure 4.2 were fit to exponential decays to characterize the decay kinetics. Equation 4.1 describes collisions that move CO(J) to CO(i):

$$CO(J) + M_J \overset{k_r}{\rightarrow} CO(i) + M_J, \tag{4.1}$$

where $i \neq J$, M_J is a collision partner that relaxes the level J, and k_r is the overall removal rate constant for J. State-to-state rotational relaxation rate constants for CO with $0 \leq J \leq 29$ were reported by Phipps *et al.*[26] Total removal rate constants k_r for individual states decrease from $J = 0$ to $J = 10$, and then are essentially constant from $J = 10$ to 29 with an average value of $k_r = 3.4 \times 10^{-10}$ cm^3 molecule^{-1} s^{-1}. Neglecting processes that move population into level J, the time dependence is given by Equation 4.2.

$$\frac{d[CO(J)]}{dt} = -\, k_r\, [CO(J)]\, [M]_J \tag{4.2}$$

Assuming pseudo-first order conditions with $[M]_J > [CO(J)]$ and defining $\gamma \equiv k_r\, [M]_J$ leads to an equation for the fractional decay of CO(J):

$$[CO(J)]_t / [CO(J)]_0 = exp\,(-\gamma\, t). \tag{4.3}$$

Decay constants γ were determined by fitting the transient signals with Equation 4.3, yielding values of $[M]_J \approx 10^{16}$ molecules cm^{-3}. This is approximately one-tenth the ambient number density at 5 Torr and is a lower limit to the actual value since collisions that populate each J level were not included. This result shows that the pseudo-first assumption is valid, and that collisions that relax centrifuged molecules most likely involve an ambient bath molecule.

4.3.7 Implications of Rotational Energy Transfer at High Energies

Observations of near-nascent J levels of optically centrifuged CO molecules provide information about rotational energy transfer in an energy regime far above thermal energies at room temperature. The centrifuge creates an inverted rotational distribution with orientated angular momentum, and the data reported here show that collisional relaxation of this ensemble has similarities with energy transfer under thermal conditions. Low translational energies for the centrifuged molecules indicate \that relaxation processes with small $|\Delta J|$ are favored, as does the slight spreading observed in the inverted rotational distribution. These features are consistent with rotational energy processes reported for thermal samples at room temperature and below and indicate that energy gap models are appropriate in the high-J regime.

There are several key differences, however, for rotational energy transfer in the high-J regime. One difference is that orientational anisotropy persists for many collisions, consistent with the physics of macroscopic gyroscopes. The presence of large amounts of angular momentum inhibits a molecule's orientational relaxation, because the directional change of the angular momentum vector through a collision is inversely proportional to the molecule's angular frequency. Measurements have shown that optically centrifuged molecules tend to lose population in individual J levels before the angular momentum projections are randomized.

A second distinct characteristic of rotational energy transfer for centrifuged molecules is that the total amount of rotational energy and the associated energy gaps are much larger than in a thermal sample. This situation results in large translational energy in molecules that result from large $|\Delta J|$ events. In the case of CO initially centrifuged to $J > 70$ with more than $9{,}000$ cm^{-1} rotational energy, the $J = 29$ level has a 900 K Doppler profile, whereas the $J = 75$ level has a 240 K profile. The near-nascent CO distribution indicates that CO_2 and N_2O likely have initial centrifuged distributions with $J > 300$ and rotational energies above $36{,}000$ cm^{-1}. In other studies, we have observed N_2O in $J = 93$ with a 3300 K Doppler profile after ~ 30 collisions and CO_2 in $J = 100$ with a 1700 K profile after ~ 30 collisions.[43,44] Simulations by Averbukh and coworkers show that an ensemble of optically centrifuged N_2 molecules first has a gyroscopic phase in which the average rotational energy remains high followed by a large increase in average translational energy as the sample redistributes the energy and a sharp drop in rotation.

4.4 Conclusion

Here, we have shown that the near-nascent rotational distributions of optically centrifuged CO molecules can be controlled by changing the spectral bandwidth of the optical trap. The time-dependent properties of individual J-levels were investigated using high-resolution transient IR absorption spectroscopy. With a full bandwidth trap, CO molecules were generated in rotational levels up to $J = 80$, whereas with a reduced bandwidth trap the maximum CO rotational level was $J = 67$. The rotational distributions are inverted, and both have peak populations near $J = 62$. The slopes of the rotational distributions for $J > 62$ mimic the intensity profile of the optical trap. The centrifuged molecules show a high degree of orientational anisotropy, with values as high as $r = 0.8$ for the $J = 60$ to 75 levels. The anisotropy values for these levels remain constant for at least 15 gas-kinetic collisions, showing that large amounts of rotational angular momentum inhibits orientational relaxation, in much the same way as macroscopic gyroscopes resist reorientation. Molecules in lower J-levels have much smaller orientational anisotropy values and return to isotropic distributions through collisions more quickly than the high J-levels. The observation of the inverted CO distribution is evidence of the extent to which spectral bandwidth correlates to molecular rotation and will guide in the future development of a tunable optical centrifuge for controlling initial rotational distributions.

These studies highlight the dynamical behavior of molecules in high J-levels that are prepared with oriented angular momentum in an optical centrifuge. The optically centrifuged levels of CO have low translational temperatures that remain low for many collisions. This observation, along with slight collisional broadening of the nascent distribution, reveals that rotational energy transfer with small $|\Delta J|$ is the predominant relaxation pathway for the centrifuged molecules, as is consistent energy gap models of rotational relaxation. Differences from thermal studies arise based on the much larger rotational energies and energy gaps of centrifuged molecules, particularly in their long-lived orientational anisotropy and large translational energy gains. These results add to the growing body of knowledge of molecules with large amounts of angular momentum and contribute to our understanding of molecular energy transfer in extreme energy conditions.

Chapter 5: Nascent Rotational Distributions and Capture Efficiencies of CO and CO_2 in a Tunable Optical Centrifuge Using Transient IR Absorption Spectroscopy

5.1 Introduction

Here, a tunable optical centrifuge is used to measure the nascent rotational distributions of CO and CO_2 to investigate how the molecular properties of the centrifuged molecules, such as the polarizability anisotropy and the moment of inertia, impact the nascent distributions produced. High-resolution transient IR absorption spectroscopy yields absolute number densities of centrifuged molecules before collisions redistribute the energy. Rotational levels up to $J = 49$ for CO and $J = 240$ CO_2. The capture and acceleration efficiencies of CO and CO_2 using variable bandwidth optical traps are compared to elucidate how different molecular species are trapped in the optical centrifuge.

Trapping and angularly accelerating a molecule in an optical centrifuge is based on the interaction of an intense optical field and the polarizability anisotropy of the molecule being trapped. The interaction energy is proportional to the polarizability anisotropy $\Delta\alpha$ of the molecule. CO and CO_2 are both linear molecules with non-zero polarizability anisotropy values, but $\Delta\alpha$ for CO_2 is nearly 4-fold larger than for CO. In addition, for a given chirp rate of the shaped pulses, the efficiency of angular acceleration of a molecule in the optical trap is affected by its moment of inertia. If the moment of inertia is too large, molecules will lag the field acceleration and be left behind. The moment of inertia for CO_2 is nearly 5-fold larger than the value for CO. A comparison of the nascent distributions for CO and CO_2 is expected to give more information about the capture and acceleration of molecules in the optical centrifuge.

The experiments reported in Chapter 4 show that the full bandwidth optical centrifuge is capable of spinning CO molecules to angular frequencies as high as $\Omega_J = 5.8 \times 10^{13}$ radians s^{-1}. This angular frequency corresponds to CO$_2$ in the $J = 388$ level. However, IR ν_3 transitions for CO$_2$ have only been reported up to $J = 128$.[42] Semi-empirical transition frequencies have been reported up to $J = 300$ in the 4000 K Carbon Dioxide Spectral Database (CDSD4000).[50] An extrapolation of the semi-empirical data to the $J = 388$ level shows that the IR frequency required is beyond the tuning range of the IR laser in our spectrometer. Additionally, assigning rotational quantum numbers to transitions near $J = 388$ would require starting at $J = 128$ and working upwards.

To overcome the obstacles described above, we reduced the bandwidth of the optical centrifuge so that the nascent CO and CO$_2$ distributions would overlap with available IR frequencies. We introduced three sequential reductions (or "clips") in the bandwidth of the optical trap using an adjustable beam block, so that the angular frequency of the trap could be varied over $\Omega_{oc}(\text{FWHM}) = (2.8 - 3.6) \times 10^{13}$ radians s^{-1}. We measured five new IR R-branch transition frequencies for probing CO$_2$ in rotational levels with $200 \leq J \leq 240$. These rotational levels have angular frequencies in this range of Ω_{oc}. We identified 5 CO rotational levels with comparable angular frequencies and measured how the nascent CO and CO$_2$ distributions respond to changes in the trap frequency. These levels are listed in Table 5.1, along with their energies and classical rotational frequencies.

Table 5.1: Rotational energies and Ω_J values for selected J-levels of CO and CO_2

CO J	E_J (cm^{-1})[a]	Ω_J (10^{13}radians s^{-1})	CO_2 J	E_J (cm^{-1})[b]	Ω_J (10^{13}radians s^{-1})
41	3,292	3.00	200	15,472	2.95
43	3,616	3.14	212	17,350	3.12
46	4,128	3.36	228	20,012	3.35
48	4,488	3.50	234	21,057	3.44
49	4,674	3.57	240	22,127	3.53

a. Energies for CO states are from (HITRAN).[42]
b. Energies for CO_2 are from semi-empirical calculations CDSD4000.[50]

5.2 Experimental Details

The optical centrifuge spectrometer with multi-pass, high-resolution transient IR absorption detection has been described in detail in Chapter 2.

5.2.1 Tunable Optical Centrifuge Pulses

The instantaneous angular frequency of the optical centrifuge pulses is shown in Figure 5.1a for the full bandwidth spectrum, along with three clipped spectra pulses, referred to here as Clips 1-3. Increasing the extent of the clip decreases the ultimate angular frequency of the optical centrifuge. Figure 5.1b shows the four trap intensities in the range of $\Omega_{\mathrm{OC}} = 2.8 - 3.6 \times 10^{13}$ radian s^{-1}, along with CO_2 and CO rotational levels with rotational frequencies in the range of Ω_{OC}. The four optical traps shown in Figure 5.2b have falloff slopes of $\beta_0 = -0.10$ per 10^{13} radians s^{-1} (full bandwidth), $\beta_1 = -0.51$ per 10^{13} radians^{-1} s (Clip 1), $\beta_2 = -0.59$ per 10^{13} radians^{-1} s (Clip 2) and $\beta_3 = -0.49$ per 10^{13} radians^{-1} s (Clip 3). At the focal point of the optical centrifuge beam, the FBW pulses have an intensity of 3×10^{13} W cm^{-2}. For the reduced bandwidth pulses, the energy of the multi-pass amplifier pump laser was decreased by 30% to avoid damaging the multi-pass amplifier.

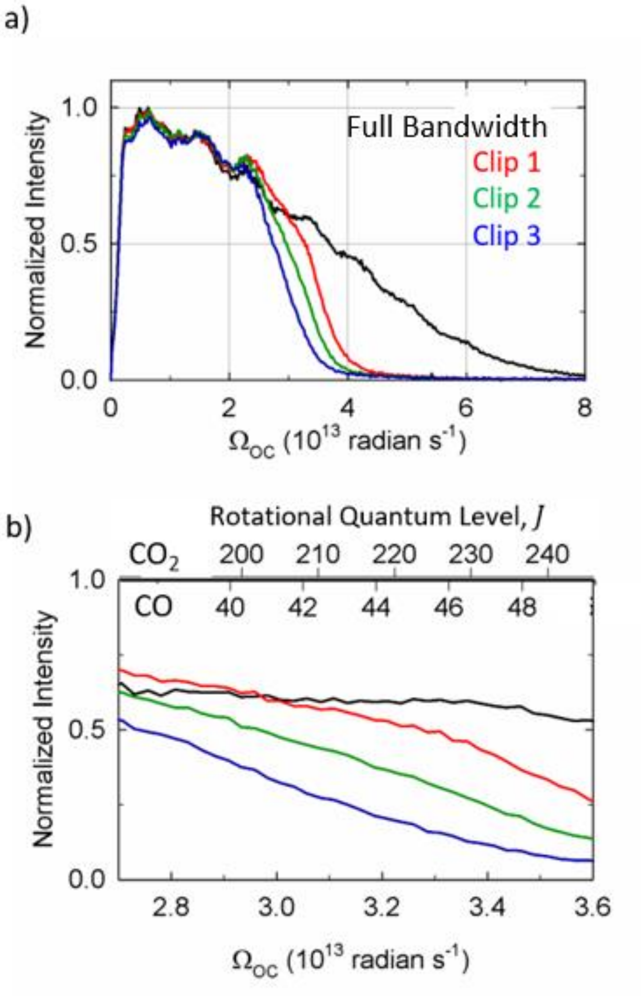

Figure 5.1 a) Instantaneous angular frequency of the full trap (black) and the three clipped chirps used in this experiment. As the clipped bandwidth increases, the extent of angular frequency decreases. b) Range of rotational levels probed for CO_2 and CO between $\Omega_{OC} = 2.8$ to 3.6×10^{13} radians s^{-1}.

5.2.2 High-Resolution Transient IR Absorption Spectroscopy of Centrifuged CO and CO_2

For these experiments, the IR laser output is wavelength-stabilized with active feedback control by locking either to a known IR transition using a reference gas cell or to a fringe of a tunable Fabry-Perot etalon. The IR wavelength is determined using known IR transitions of thermally populated levels and a calibrated wave meter to a resolution better than $\Delta\nu_{wm} = \pm 0.001$ cm^{-1}. The transmitted IR intensity is collected as a function of time on an InSb detector with a signal response of 50 ns. Transient signals are averaged on a 500 MHz digital oscilloscope (Tektronix) for typically 100 laser pulses. The IR probe polarization is vertical to coincide with the plane of molecular rotation in the optical centrifuge. Spectroscopic grade CO and CO_2 were used. Transition frequency measurements for CO_2 used a cell pressure of 2.5 Torr. Nascent distributions for CO and CO_2 were measured with a cell pressure of 500 mTorr at $t = 100$ ns following the optical centrifuge pulse. At 500 mTorr, the gas kinetic collision time is approximately 200 ns based on Lennard-Jones collision rate constants, as shown in Table 2.3.

Nascent distributions of optically centrifuged CO and CO_2 were probed using transient IR absorption spectroscopy near λ=4.3 μm. The CO probe is the IR fundamental,

$$CO\ (\mathrm{v} = 0,\ J) + IR \rightarrow\ CO\ (\mathrm{v} = 1, J + 1). \qquad (5.1)$$

The CO_2 probe involves absorption of one quantum of the ν_3 antisymmetric stretching mode,

$$CO_2(00^0 0, J) + IR \rightarrow CO_2(00^0 1, J + 1). \qquad (5.2)$$

R-Branch transitions were used as the IR probes of both CO and CO_2. To identify the CO_2 transitions for levels with $J = 200$ to 240, transient signals were collected as a function of IR wavelength in frequency steps of $\delta_\nu \leq 0.001$ cm^{-1} between neighboring IR transitions. When possible, the transitions were measured relative to known IR transitions.

5.3 Results and Discussion

Here capture and acceleration efficiencies of CO and CO_2 in a tunable optical centrifuge are reported. Nascent rotational distributions are measured using high-resolution transient IR absorption spectroscopy. A comparison of the CO and CO_2 data provide information about the role of polarizability anisotropy and moment of inertia in the optical trapping process.

First, the transient spectroscopy of CO_2 R-branch transitions for $J \geq 200$ is reported, followed by two experiments to measure the total number density of rotationally excited molecules. The first experiment uses the full spectral bandwidth to measure the number density of molecules with Ω_J values that are significantly below the maximum Ω_{OC}. The measurements in this first experiment provide an indication of the number density of molecules that fall out of the trap in the process of acceleration. In the second experiment, the nascent CO and CO_2 rotational distributions are measured separately, each at a pressure of 500 mTorr using the three reduced-bandwidth optical traps. Combining these two measurements yields the total number density of captured molecules that are accelerated by the optical field, from which the capture and acceleration efficiencies of CO and CO_2 are compared.

5.3.1 Transient IR Probe Transitions of CO_2 $(00^0 0, J = 200 - 240)$

Spectral fingerprinting was used to measure IR transition frequencies for five CO_2 $(00^0 1 \leftarrow 00^0 0)$ R-branch transitions with $J = 200$ to 240. The $R(56)$ $(01^1 1 \leftarrow 01^1 0)$ transition was used to help locate the $R(212)$ $(00^0 1 \leftarrow 00^0 0)$ transition. Figure 5.2a shows the line-center transient absorption signals for $R(56)$ and $R(212)$ at a cell pressure of 2.5 Torr. Figure 5.2b shows the transient spectra at two times, $t = 90$ ns and 200 ns, following the optical centrifuge pulse. The transient spectra in Figure 5.2 give dynamical information about collisional energy transfer of rotationally excited molecules. In these measurements, the average time between collisions is 40 ns. The $(00^0 0)\ J = 212$ transient signal is prompt, showing that this level is populated directly by the optical centrifuge. This level then undergoes collision-induced relaxation with a lifetime of 3.8 μs, corresponding to approximately 95 collisions. In contrast, the transient signal for $(01^1 0)\ J = 56$ has slower appearance with an exponential rise to maximum and a lifetime of 800 ns, showing that this level is populated through collisional energy transfer.

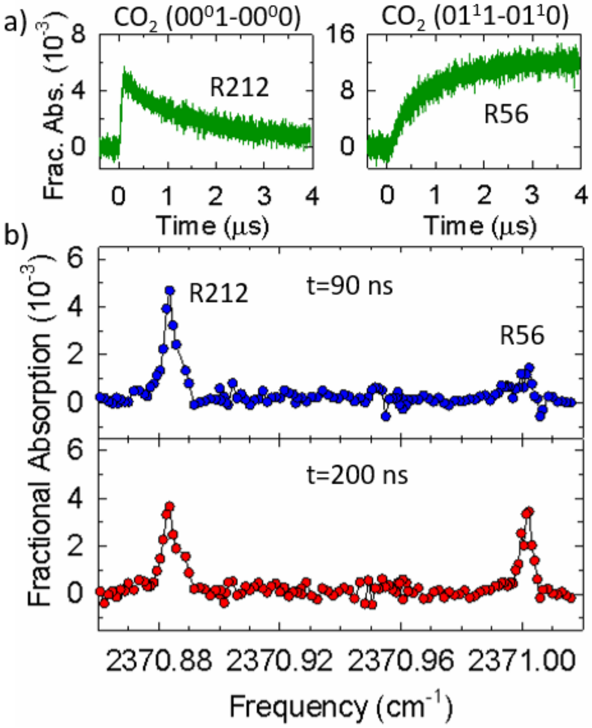

Figure 5.2 a) Line-center transient absorption signals showing that the $(00^0 0, J = 212)$ level is formed promptly in the optical centrifuge while the $(01^1 0, J = 56)$ level is populated by collisions of centrifuged molecules. b) Spectral fingerprinting of the CO_2 $(00^0 1 - 00^0 0)\ R(212)$ transition relative to the $(01^1 1 - 01^1 0)\ R(56)$ transition at $t = 90$ ns and 200 ns following the optical centrifuge pulse.

Once the new transitions were located, transient Doppler-broadened line profiles were measured and the line-center transition frequencies were determined to within $\Delta\nu = \pm 0.002\ \text{cm}^{-1}$ using the wavemeter. Table 5.2 lists the IR probe frequencies for CO and CO_2 used in this study and compares the CO_2 probe transition frequencies with predicted frequencies from the effective Hamiltonian calculations by Perevalov and coworkers (CDSD4000).[50] The observed CO_2 R-branch transition frequencies for $J \leq 240$ are within 0.04 cm^{-1} of the calculated values.

Table 5.2: IR probe transition frequencies for CO and CO_2

CO J	$\bar{\nu}$ (cm^{-1}) [a]	CO_2 J	$\bar{\nu}$ (cm^{-1}) [b] observed	$\bar{\nu}$ (cm^{-1}) [c] (CDSD4000)	$\Delta\bar{\nu}$ (cm^{-1}) obs-calc
41	2271.345	200	2377.441	2377.432	0.009
43	2275.719	212	2370.885	2370.870	0.015
46	2281.970	228	2360.743	2360.717	0.026
48	2285.928	234	2356.552	2356.522	0.030
49	2287.843	240	2352.186	2352.151	0.035

a. HITRAN database[42]

b. Observed R-branch transitions are a subset of 29 new transitions for CO_2 (00^00) with J between 186 and 280. The uncertainty in the observed transition frequencies is $\Delta\nu_w = \pm 0.005$ cm^{-1}, based on the maximum fluctuations in the wavemeter frequencies.

c. Predicted transition frequencies from the CDSD4000.[50]

5.3.2 Rotational Excitation Using the Full Bandwidth Trap

Figure 5.3a shows transient absorption signals of CO rotational levels between $J = 41$ to 49 and for CO_2 levels between $J = 200$ to 240. These data were collected using the full bandwidth trap at a pressure of 500 mTorr. The transients between 50 ns and 200 ns represent nascent signals, based on the time window between the detector rise time and the average collision time. In Figure 5.5b, the signal intensities at $t = 100$ ns have been converted to number densities, and are shown as a function of angular frequency and rotational quantum number. The number densities for both CO and CO_2 are fairly independent of J with a standard deviation of 7%. Because the full bandwidth trap is capable of spinning molecules into much higher rotational levels, the numbers densities for the levels probed here are fairly small, relative to the peak of the nascent inverted distribution. The average number density for the CO levels in this range is $4.8\, x10^{12}$ molecules cm^{-3}, which is almost twice the value for the CO_2 levels, $2.5\, x10^{12}$ molecules cm^{-3}. Interestingly, CO_2 has twice as many rotational levels as CO between $\Omega_J = 2.9$ to 3.6×10^{13} radians s^{-1}, so that the integrated number density for both species in this frequency range is comparable.

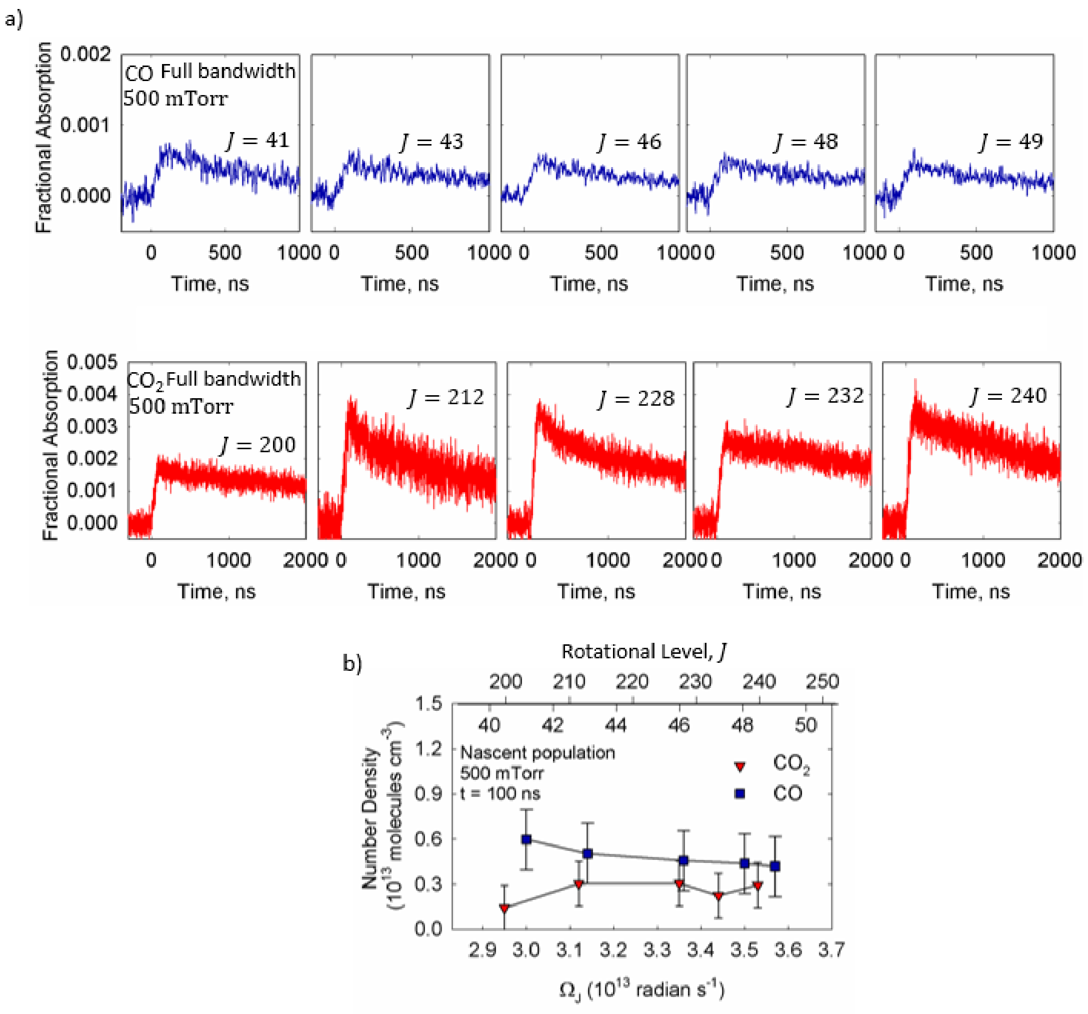

Figure 5.3 a) Transient fractional absorption measurements of CO $J = 41 - 49$ and b) number density as a function of angular frequency for CO$_2$ $J = 200 - 240$ (red triangles) and CO $J = 41 - 49$ (blue squares) using the full optical bandwidth at a pressure of 500 mTorr.

The data shown in Figure 5.5b represent molecules that have been captured by the optical field and then have fallen out of the trap during the acceleration process. Molecules can fall out of the optical trap when their internal kinetic energy exceeds the interaction energy with the optical trap, as shown in Equation 2.2, and/or when the field intensity drops below a critical trapping intensity. The optical centrifuge beam has a Gaussian cross section, and it is likely that the signals in Figure 5.5b originate from the wings of the Gaussian beam that have lower intensity.

5.3.3 Nascent Distributions of CO and CO_2 From a Tunable Optical Centrifuge

Nascent rotational distributions were measured for CO ($J = 41$ to 49) and CO_2 ($J = 200$ to 240) using a tunable optical centrifuge for which Ω_{OC} was sequentially reduced. In total, four optical bandwidths were used: the full bandwidth` and three reduced-bandwidth traps, Clips 1-3. Figure 5.4a shows the angular profiles for the full bandwidth and the three clipped traps. As the optical bandwidth is decreased, the trap intensity at large values of Ω_{OC} decreases and angular acceleration of the trap ends earlier in time. In this manner, molecules are released from the trap at lower angular frequencies and the rotational distribution shifts to lower J levels.

First, the effect of reducing the centrifuge angular frequency is illustrated by measuring the peak of the CO distribution as a function of the clip. Figure 5.4b shows that the CO $J = 62$ level is populated in the full bandwidth optical centrifuge, and that no population is observed when the bandwidth is reduced in Clips 1-3. The relative intensity of the full optical trap $I_{FBW} = 0.36$ at the rotational angular frequency for CO $J = 62$ ($\Omega_J = 4.48\, x\, 10^{13}$ radians s^{-1}) is enough to drive molecules to this level but is weak enough to release a substantial subset of the captured molecules at this frequency. In contrast, the relative intensity of Clip 1 bandwidth $I_{C1} = 0.02$ is insufficient to ramp molecules into the $J = 62$ level, indicating that the critical intensity to hold onto CO molecules is $I_C > 0.02$.

Figure 5.4c shows the progression of population in CO $J = 49$ ($\Omega_J = 3.57\, x\, 10^{13}$ radians s^{-1}) as the bandwidth is sequentially decreased. The signal increases nearly 3-fold when the full bandwidth is reduced to Clip 1. Further bandwidth reduction of Clips 2 and 3 leads to reduced population in CO $J = 49$. Figure 5.4d shows the progression of population in CO_2 $J = 240$, which has an angular frequency very close to that for CO $J = 49$ ($\Omega_J = 3.50\ x\ 10^{13}$ radians s^{-1}). The effect of the clipped bandwidth pulses is nearly identical to that for CO $J = 49$. Thus, the two molecular species respond similarly to changes in the trap properties. Figures 5.4c and 5.4d show that by reducing the trap bandwidth, it is possible to tune through the peak of the nascent rotational distribution.

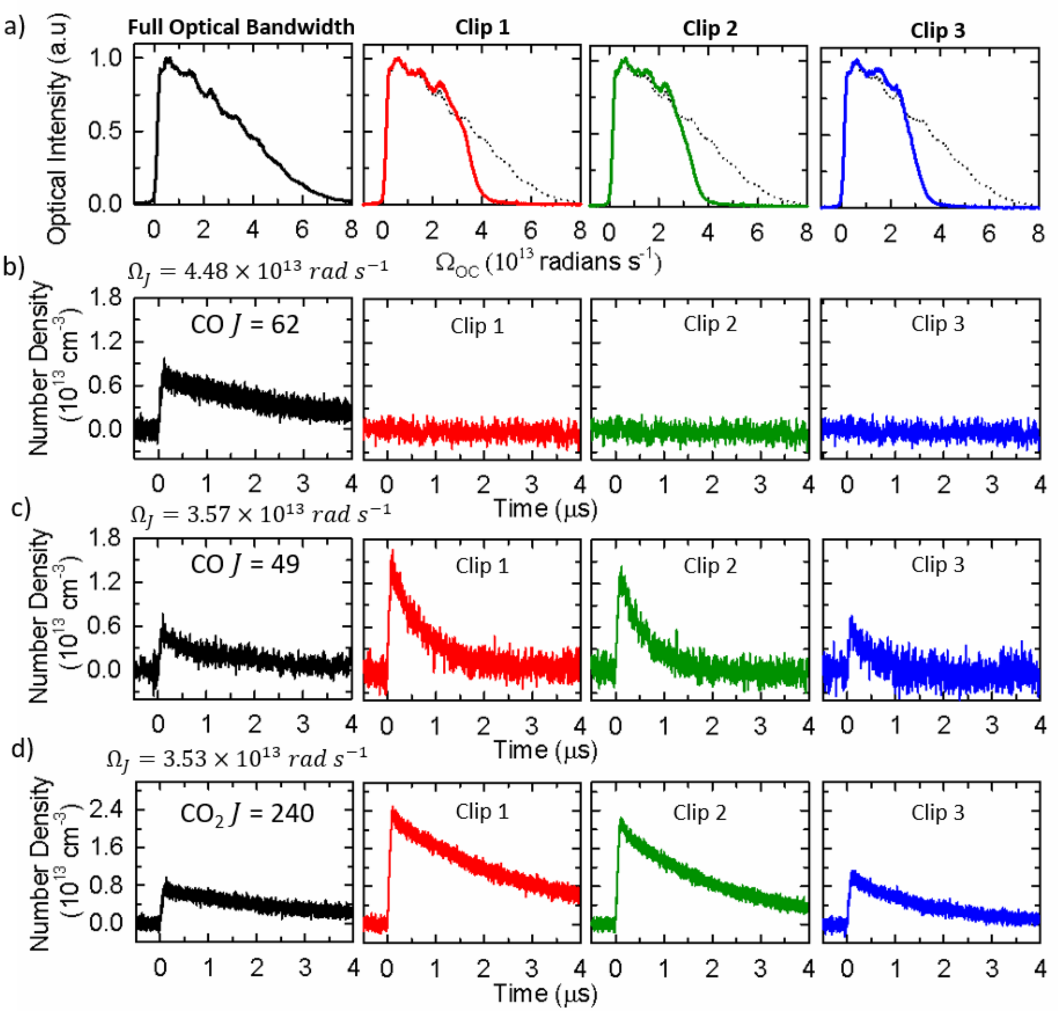

Figure 5.4 a) Full bandwidth spectrum (left-most), and three reduced bandwidth decreasing from left to right. Measurement of number densities for b) CO ($J = 62$), c) CO ($J = 49$), d) CO_2 ($J = 240$) at the four bandwidths.

Figures 5.5a-h show the time-dependent nascent rotational distributions for CO ($J = 41$ to 49) and CO_2 ($J = 200$ and 240) made with the full bandwidth and sequentially-reduced bandwidths (Clips 1-3) at a number of times between 100 and 1000 ns. The shapes of the clipped optical traps are shown as dotted black lines along with the data, where the trap intensity has been scaled to the most populated rotational level. The time-dependent data show that rotationally excited CO relaxes more quickly than CO_2, in the same rotational frequency range.

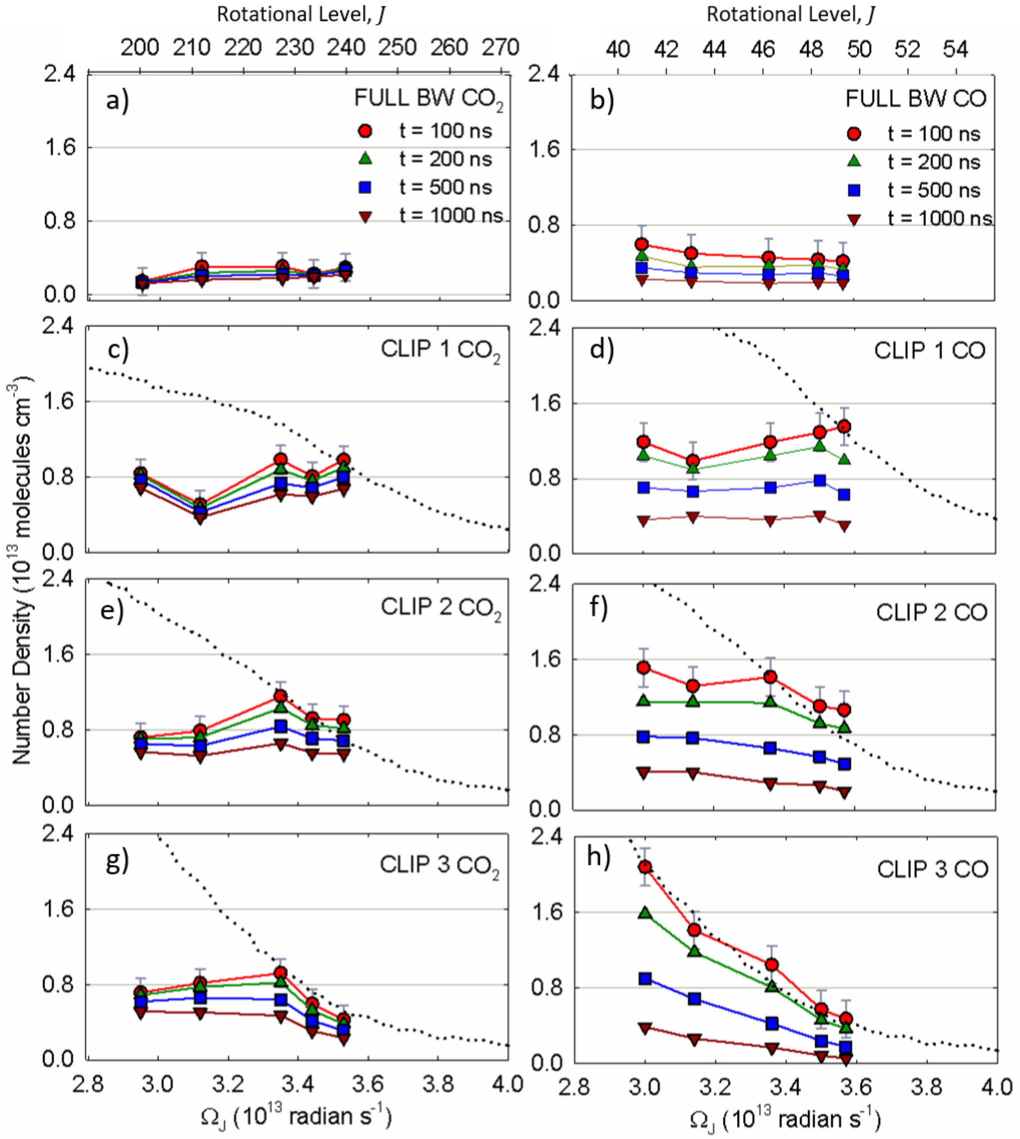

Figure 5.5. Nascent population distributions of CO_2 and CO rotational levels using the a-b) full bandwidth trap and c-h) as a function of reducing the optical centrifuge spectral bandwidth. The clipped spectra are shown as black dotted lines and have been scaled to the peak of each distribution.

Here, the distributions at $t = 100$ ns are compared as a function of the optical trap. Figures 5.5a and b show the CO_2 and CO distributions made with the full bandwidth trap. The signals are relatively small and J-independent. Figures 5.5c and d show that Clip 1 leads to increased population in CO_2 by as much as a factor of 6 and in CO by as much as a factor of 3. Both molecules show an inverted population distribution from the Clip 1 trap, with the largest population in the higher-J levels. Figures 5.5e and f show that Clip 2 releases population at lower J levels and both distributions peak at the similar angular frequency near $\Omega_J = 3.35 \times 10^{13}$ radians s^{-1}. In both cases, the higher-J distributions track the trap intensity for ensembles prepared with Clip 2. The Clip 2 trap also releases more of the lower-J levels of CO than of CO_2, leaving the inverted CO distribution less pronounced. Figures 5.5g and h show the result of further reduction in the bandwidth with Clip 3. Here, the two distributions have notable differences. The CO_2 distribution continues to have an inverted distribution with the peak near $\Omega_J = 3.35 \times 10^{13}$ radians s^{-1} and the higher-J states tracking the field intensity. In contrast, the peak of the CO distribution has shifted to lower angular frequencies and the population inversion is no longer present in this range of angular frequencies. The entire CO distribution in Figure 5.5h tracks the Clip 3 intensity.

A comparison of the data for Clips 2 and 3 reveals important information about how different molecular species are released from an optical centrifuge trap. Notably for Clips 2 and 3, CO_2 retains a peak population at $\Omega_J = 3.35 \times 10^{13}$ radians s^{-1}, whereas the peak population for CO with Clip 3 is seen at $\Omega_J = 3.00 \times 10^{13}$radians s^{-1}. This observation is explained by the fact that CO_2 his held more tightly by the optical trap based on its larger polarizability anisotropy. This phenomenon indicates that a critical intensity exists for which the interaction energy is low enough that molecules are released from the trap. This critical intensity is larger for CO, and molecules are released sooner in the trap than are CO_2 molecules

Qualitatively, the CO and CO_2 distributions have similar responses to clipping the optical centrifuge bandwidth. The extent of rotational excitation is sensitive to the angular frequency of the optical trap and its corresponding intensity at that frequency. For the same optical trap, different molecules are excited to similar angular frequencies, despite differences in their moments of inertia, rotational energies, and anisotropic polarizabilities. This feature is at the heart of the optical centrifuge technique.

The lifetimes of CO ($J = 41$ to 49) and CO_2 ($J = 200$ to 49) prepared with the clipped spectra were determined by fitting the transient absorption signals to exponential decays from their peak values near $t = 100$ ns. In some cases, a single exponential fit was sufficient to characterize the decay signal. In other cases, the transients are better characterized by biexponential decays. The lifetimes are shown in Tables 5.3 and 5.4.

In general, the lifetimes become shorter as the clip increases since the nascent distributions have less rotational energy. CO relaxes significantly faster than CO_2. For example, CO_2 in $J = 240$, populated using Clip 1, has a fast component $\tau_1 = 0.07$ μs and a slow lifetime component $\tau_2 = 3$ μs. At a comparable angular frequency with Clip 1, CO in $J = 49$ has a fast lifetime component $\tau_1 = 0.02$ μs and a slow component $\tau_2 = 0.6$ μs. Overall, this CO transient relaxes nearly 5 times faster than CO_2. For Clip 3, the CO $J = 49$ transient has a single exponential lifetime of $\tau_1 = 0.4$ μs, which is 4 times shorter than the longer lifetime $\tau_2 = 2$ μs for CO_2 in $J = 240$. This comparison indicates that the CO has more efficient rotational energy transfer than CO_2 with the same angular frequency.

Table 5.3: Lifetime of CO_2 rotational levels

	Clip 1		Clip 2		Clip 3	
CO_2 J-level	τ_1 (μs)	τ_2 (μs)	τ_1 (μs)	τ_2 (μs)	τ_1 (μs)	τ_2 (μs)
200	500	----	500	----	3	----
212	0.07	3	0.08	3	2	----
228	0.2	3	0.2	2	0.2	----
234	0.08	4	0.2	2	0.1	2
240	0.07	3	0.1	2	0.09	2

Table 5.4: Lifetime of CO rotational levels

	Clip 1		Clip 2		Clip 3	
CO Rotational Level	τ_1 (μs)	τ_2 (μs)	τ_1 (μs)	τ_2 (μs)	τ_1 (μs)	τ_2 (μs)
41	0.8	----	0.02	0.8	0.09	0.6
43	1	----	0.7	0.8	0.5	0.7
46	0.8	----	0.2	0.7	0.2	0.6
48	0.8	----	0.1	0.6	0.5	----
49	0.02	0.6	0.3	0.7	0.4	----

Once the optical trap has reached the angular frequency that corresponds to the critical intensity, the distribution of molecules released from the trap scales with the trap intensity. This behavior was demonstrated in Figures 5.5g and 5.5h. The time-dependent relaxation of this subset of molecules is further investigated here. Figure 5.6 shows snapshots of the CO_2 and CO populations at 10 times from $t = 100$ to 1000 ns. The CO_2 $J = 228$ level shows a decrease in population over time, whereas the $J = 240$ level shows little population change. Both distributions show collisional broadening over time. The rotational distributions were fit to exponential functions $e^{-\beta x}$ where β

is the exponential parameter. The broadening of the CO distribution is narrower than that for CO_2. The CO data have a fitting parameter $\beta = 0.19\, J^{-1}$, whereas CO_2 has $\beta = 0.064\, J^{-1}$. The data in Figure 5.6, along with the lifetime data, show that CO relaxes more quickly than CO_2 for the same range of angular frequencies. Smaller energy gaps result in more efficient rotational energy transfer. CO energy gaps are $\Delta E = 174$ cm^{-1} on average in this region whereas the average energy gaps for CO_2 are $\Delta E = 347$ cm^{-1}. The factor of two in the energy gaps arises from CO_2 having even J levels in the (00^00) vibrational level.

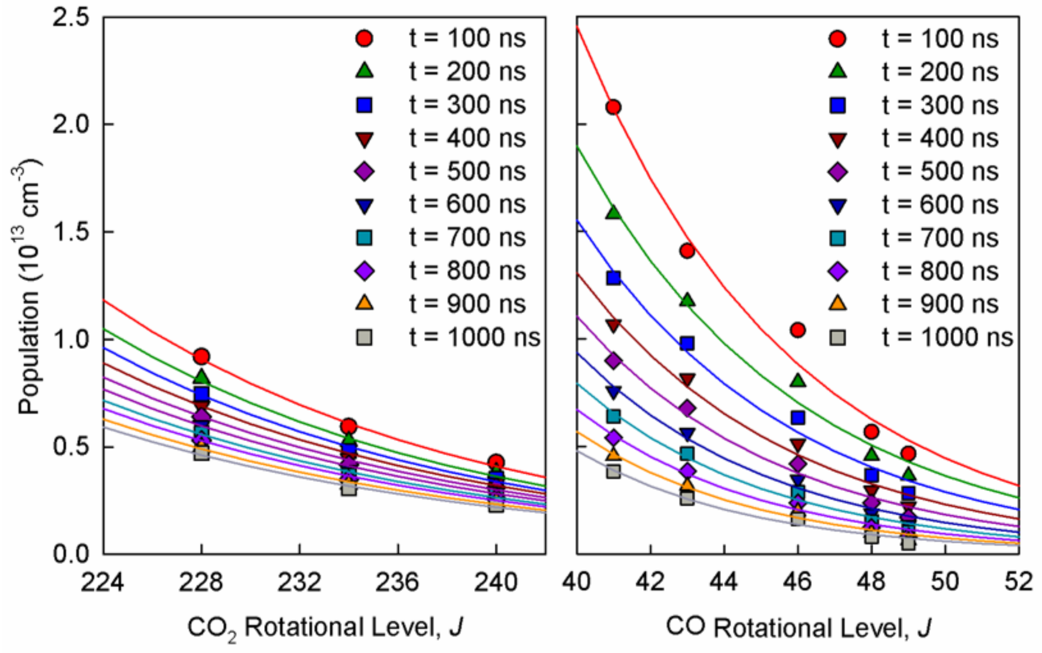

Figure 5.6. Time-dependent rotational distribution of CO_2 and CO using the Clip 3 bandwidth. The rotational distributions were fit to exponential functions.

5.3.4 Capture and Acceleration Efficiencies

Here, capture and acceleration efficiencies of CO and CO_2 are compared based on the nascent population distribution measurements. The total number density of molecules that are captured and angularly accelerated in an optical centrifuge can be determined by summing the population over all J levels. Data collected with the optical full bandwidth centrifuge give a measure of the J-independent number densities of molecules that fall out of trap. The clipped bandwidth data are used to characterize the inverted distributions that are released by the centrifuge. For CO with $J < 41$, the average number density is $N = 4.8\ x10^{12}$ cm^{-3} per level and for CO_2 with $J < 200$, the average number density is $N = 2.5\ x10^{12}$ cm^{-3} per level. These values are shown in Figure 5.7 in grey. The nascent distributions from Clip 3 are shown in red. Number densities for levels that were not measured are interpolated and shown in green.

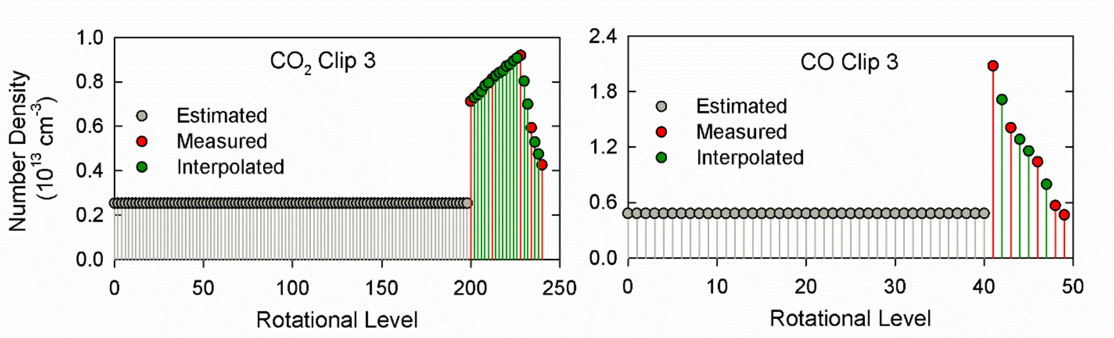

Figure 5.7 Determining total number densities of captured CO and CO_2 molecules in the tunable optical centrifuge using Clip 3. The measured CO ($J = 41$to 49) and CO_2 ($J = 200$ to 240) are shown as red circles, the average number densities using the full optical centrifuge bandwidth are shown as grey circles, and interpolated data between rotational levels in the nascent distribution are shown as green circles.

The total number densities for captured molecules were determined using the three reduced bandwidth measurements. These values are shown in Figure 5.8a as a function of Clip number. The total number density for CO is near $N_{OC}(CO) = 3.1 \times 10^{14}$ cm^{-3} for each Clip. The total number density for CO_2 with Clip 1 is $N_{OC}(CO_2) = 5.2 \times 10^{14}$cm^{-3}. The values for CO_2 decrease slightly with Clip number, and for Clip 3, $N_{OC}(CO_2) = 4.1 \times 10^{14}$ cm^{-3}. The average number density for CO_2 is $N_{OC}(CO_2) = 4.6 \times 10^{14}$ cm^{-3}. The ratios of total number density for captured CO_2 and CO is approximately 1.5, as shown in Figure 5.8b. Thus, both CO_2 and CO are captured and accelerated with nearly the same efficiencies. The increased value for CO_2 is most likely because of its larger interaction energy with the field.

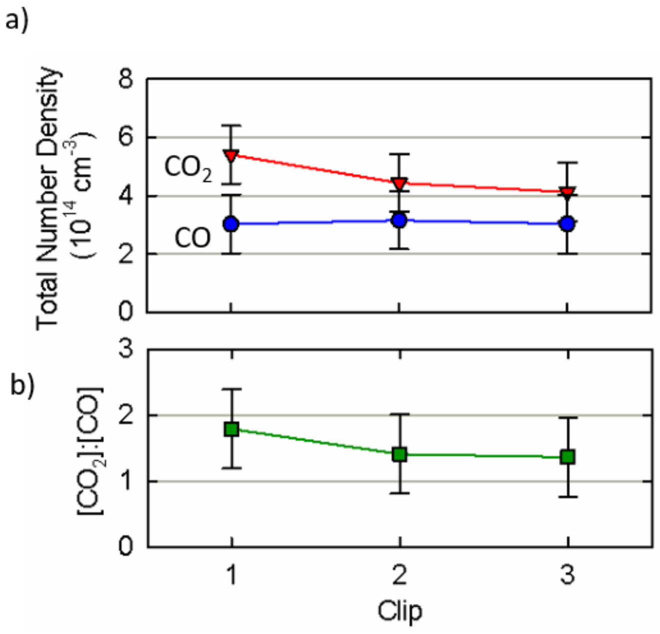

Figure 5.8 a) Total number densities of trapped molecules for CO and CO_2 from integrated distributions. b) The ratio $[CO_2]$:[CO] = 1.5.

Capture and acceleration efficiencies are determined by comparing the number density of centrifuged molecules to the number density in the cell. The number density at 500 mTorr is $N = 1.6 \times 10^{16}$ cm^{-3}. Our results show that the optical centrifuge captures and accelerates about 2% of the CO sample and about 3% of the CO_2 sample. These values are most likely lower limits since the complete distributions were not measured directly and were tabulated based on extrapolated lower-J levels and interpolated higher-J levels.

5.3.5 Intensity-Dependent Nascent Populations

Figure 5.9 explores how the molecules released by the centrifuge are affected by the intensity of the trap. Figure 5.9a shows the instantaneous laser power of the trap in units of mJ per ps as a function of angular frequency. Figure 5.9b shows number densities of CO and CO_2 as a function of the instantaneous laser power. For each J-level measured, the maximum number density of molecules that are released from the trap occurs when the instantaneous laser power is near 0.05 mJ ps^{-1}. The data in Figure 5.9b show that CO and CO_2 are released from the optical centrifuge at similar trap intensities.

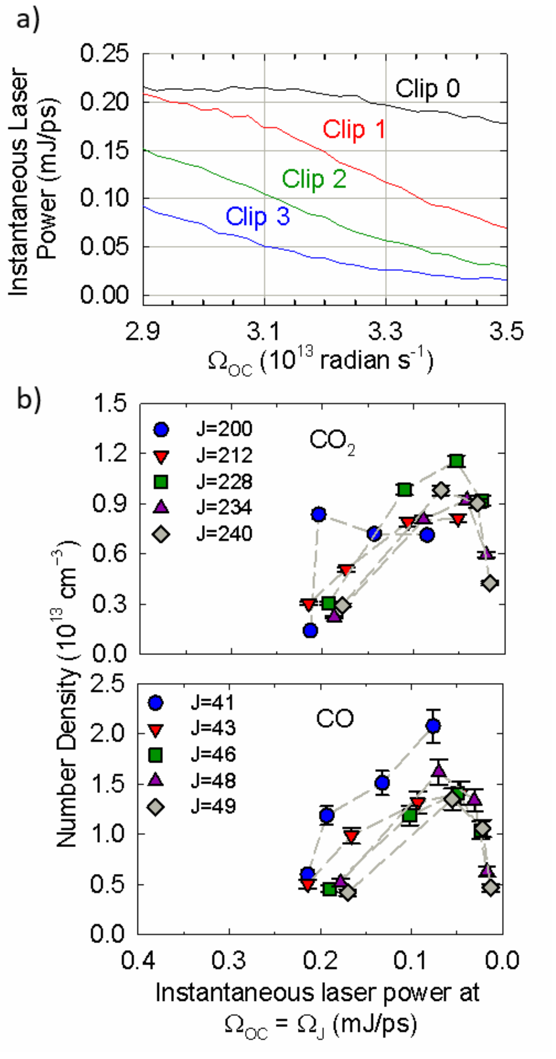

Figure 5.9 a) Instantaneous laser power of sequentially clipped pulses and a function of optical centrifuge angular frequency. Transient populations at 100 ns of CO_2 (b) and CO (c) rotational states as a function of instantaneous laser power. The optical trap effectively traps CO and CO_2 molecules until an instantaneous power near 0.05 mJ ps^{-1}.

A molecule remains trapped in the field until the interaction potential experienced by the molecule has fallen below the lower limit

$$U_0 > 2\pi I\beta, \tag{5.3}$$

where β is the chirp rate. Equation 5.3 can be combined with Equation 2.1 to provide a given pulse intensity required for sufficient trapping of a molecule and is shown in Equation 5.4.

$$E^2 > \frac{8\pi I\beta}{\Delta\alpha} \tag{5.4}$$

The values of $I/\Delta\alpha$ are 2.46 and 3.05 for CO and CO_2, respectively, and therefore the lower limit for these two molecules to stay trapped is similar. These similar ratios are likely the reason that CO and CO_2 follow a similar trend in Figure 5.9. These results provide a lower limit of intensity I needed to rotationally excite molecules, and will enable future experiments by allowing us to maximize population in levels with specific rotational energies through manipulation of the bandwidth and intensity of the electric field. Increasing number densities of nascently centrifuged molecules provides an opportunity to study the dynamics of molecules in this newly explored energy regime.

5.4 Conclusion

We have shown that high-resolution transient IR absorption spectroscopy is a powerful tool capable of measuring the capture and acceleration efficiency of the optical centrifuge. The first experiment using the full bandwidth of the optical centrifuge provides a measure the J-independent number density of molecules that fall out of the trap as it proceeds through its angular acceleration. The second set of measurements provide number densities for the CO and CO_2 nascent distributions. The results show that the optical centrifuge captures and accelerates about 3% CO_2 and about 2% CO. Parameters of the optical centrifuge can now be tuned to maximize the number density of captured molecules. Increasing the number density of captured molecules will result in larger signal sizes such that the collision dynamics of nascently centrifuged molecules can be further studied.

Chapter 6: Investigating the Relaxation of the Nearly-Nascent CO and N_2O Distributions with a Buffer Gas Collision Partner

6.1 Introduction

In this chapter, the relaxation dynamics of CO and N_2O super rotors with He and Ar buffer gases are investigated. Sudden and adiabatic collision regimes are explored from the impact that He and Ar buffer gases have on super rotor relaxation. A sudden collision occurs when the interaction time t_{col} between collisions partners is comparable to or longer than the rotational period t_{rot} of the molecule. In this regime, the rotational motion of the super rotor is slow enough that impulsive collisions can occur between the collision partners, and energy is readily transferred. An adiabatic collision occurs when the rotational interactions that are period of the molecule t_{rot} is much faster than the interaction time t_{col}, leading to more repulsive and less efficient energy transfer. Argon is ten times more massive than helium, which leads to differences in their relative velocities and interaction times in super rotor collisions.

An adiabaticity parameter describes the efficiency of rotation-to-translation energy transfer during a collision based on the rotational period of the molecule t_{rot} and the duration of the collisional interaction t_{col}:

$$a = \frac{t_{col}}{t_{rot}}. \tag{6.1}$$

When $a \leq 1$, the collisions are in the sudden regime, and efficient rotation-to-translation energy transfer is expected. When $a > 1$, the collisions are in the adiabatic regime, leading to less efficient rotation-to-translation energy transfer. The classical rotational period of the molecule is

$$t_{rot} = 2\pi/\omega_{rot}, \tag{6.3}$$

where ω_{rot} is the rotational frequency of the molecule in units of radians per second. The average collision duration is defined here as

$$t_{col} = \ell / v_{rel}, \tag{6.2}$$

where ℓ is the distance of the collision interaction and v_{rel} is the relative velocity between collision partners. The interaction length ℓ is determined from a Lennard-Jones potential energy curve for a head-on collision at 300 K, and is taken to be the distance σ that marks the onset of the repulsive interaction to a larger distance at which the absolute value of the potential energy is 1% of thermal collision energy (3 cm^{-1}). The transition between the adiabatic to sudden collision regimes has not been measured experimentally for CO and N_2O super rotors and the exact range of interaction lengths remains unknown.

A Lennard-Jones potential energy describes the interaction between two non-bonding atoms or molecules based on their distance of separation. The potential $V(r)$ accounts for the combination of attractive forces (including dipole-dipole, dipole-induced dipole, and dispersion) and repulsive forces:

$$V(r) = 4\mathcal{E}\left[\left(\frac{\sigma}{r}\right)^{12} - \left(\frac{\sigma}{r}\right)^{6}\right]. \tag{6.4}$$

In this equation, $\mathcal{E}$ is the well-depth of the potential, which describes the strength of the attractive component between collision partners, σ is the maximum distance at which the potential is repulsive, and r is the center-to-center distance between the two particles. For collisions of a buffer gas (BG) and a super rotor (SR), values of ε and σ were determined

$$\varepsilon_{col} = using\sqrt{(\varepsilon_{BG} * \varepsilon_{SR})} \tag{6.5}$$

and

$$\sigma_{col} = \frac{(\sigma_{BG} + \sigma_{SR})}{2}. \tag{6.6}$$

The Lennard-Jones parameters for He-CO, He-N_2O, and Ar-N_2O collisions are shown in Table 6.1. The collision rate constant k_{LJ} was determined from Equation 2.26.

Table 6.1 Lennard-Jones parameters for buffer gas-super rotor collisions

Collision Partners	ε_{LJ} (cm^{-1})	σ_{LJ} ($x10^{-10}$ m)	v_{rel} (m s^{-1})	k_{LJ} ($10^{-10} cm^3 s^{-1}$)
He-CO	22.2	3.16	1460	3.82
He-N_2O	33.0	3.08	1430	3.75
Ar-N_2O	113	3.50	600	2.78

The Lennard-Jones potential energy curves for collisions between He-CO, He-N_2O, and Ar-N_2O are shown in Figure 6.1a. The potential energy curve for Ar-N_2O collisions (red) has an attractive component that is 3-5 times stronger than He collisions with N_2O and CO. Adiabaticity curves for collisions between He-CO, He-N_2O, and Ar-N_2O are shown in Figure 6.1b based on the adiabaticity parameters shown in Table 6.2. Because the reduced mass of Ar and N_2O is 5.7 times larger than that with He as a collision partner, the relative velocity v_{rel} is smaller and the collision interaction time t_{col} is longer. The division between sudden and adiabatic collision regimes occurs near $a = 1$. The rotational levels where $a = 1$ for He-CO, He-N_2O, and Ar-N_2O are estimated as $J = 54, 213$ and 53, respectively. Rotational levels are investigated here for CO and N_2O that are near $a = 1$ for collisions with He: $J = 42 - 70$ for CO and $J = 92 - 197$ for N_2O. At an angular frequency of $\Omega_{OC} = 3.03 \times 10^{13}$ radians s^{-1}, CO is rotationally excited to $J = 42$ with $E_{rot} = 3400$ cm^{-1} and N_2O is rotationally excited to $J = 192$ with $E_{rot} = 15{,}500\ cm^{-1}$.

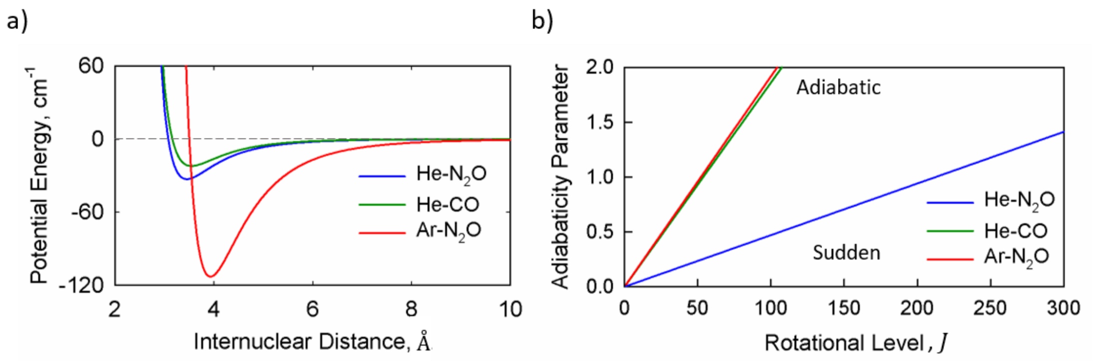

Figure 6.1 a) Lennard-Jones potential energy and b) adiabaticity curves for collisions between CO and N_2O with He and Ar.

Table 6.2 Adiabaticity parameters for super rotor-buffer gas collisions

Molecule	Reduced mass (amu)	t_{col} (ps)	Rotational level J where $a = 1$
CO-He	3.50	0.16	54
N_2O-He	3.67	0.19	213
N_2O-Ar	20.9	0.76	53

6.2 Experimental Details

The optical centrifuge was used to populate high-J rotational levels of CO and N_2O to investigate the effect that collisions with buffer gas atoms have on the rotational relaxation of the nearly-nascent distribution of centrifuged molecules. As shown in Figure 6.1a, two optical bandwidths were used in this experiment, the full trap bandwidth (grey) and a reduced bandwidth (blue). The instantaneous angular frequency of both centrifuges is shown in Figure 6.1b. The full bandwidth trap has optical intensity beyond $\Omega_{oc} = 6.0 \times 10^{13}$ radians s^{-1}. The reduced optical bandwidth (shown in blue) has a decreasing slope from $\Omega_{oc} = 2.5$ to 3.5×10^{13} radians s^{-1}. The collision dynamics of He and Ar buffer gases with CO and N_2O were investigated using high-resolution transient IR absorption. The sample detector used in this experiment had a

100 ns rise time. Transient absorption signals for CO $J = 42$ to 70 and N_2O $J = 92$ to 197 were collected with either vertically polarized or horizontally polarized IR probe light, at a pressure of 5 Torr. Buffer gas experiments with CO were performed by adding up to 10 Torr He. Buffer gas experiments with for N_2O were performed by separately adding up to 10 Torr He or 10 Torr Ar. Transient Doppler-broadened line profiles were measured for CO $J = 42$ to 70 with 4 Torr CO and either 2 Torr or 4 Torr He. Doppler profiles were measured for N_2O $J = 140 - 197$ with 5 Torr N_2O and either 10 Torr He or 10 Torr Ar. Line profiles were fit to Gaussian functions and the time dependent translational temperatures were extracted from the fits.

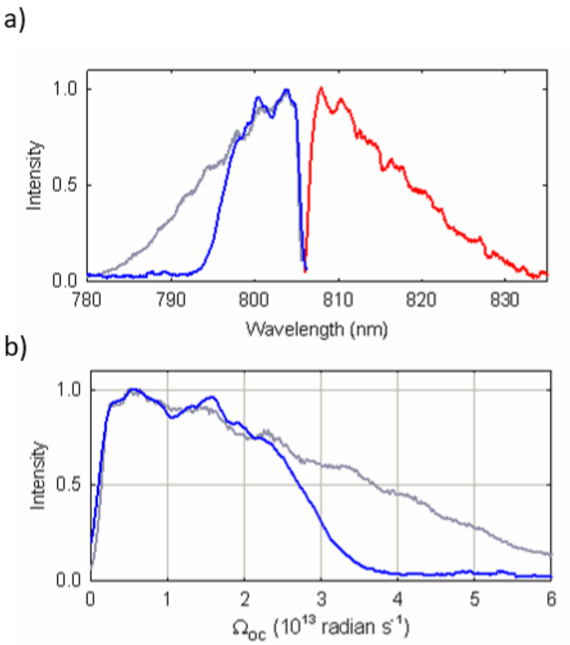

Figure 6.2 a) Clipped optical bandwidth (shown in blue) used to populate high-J rotational levels of N_2O. b) Time-dependent angular frequency of clipped optical bandwidth (shown in blue) compared to the full optical bandwidth (shown in grey).

6.3 Results

Here, the collision dynamics of CO and N_2O with He and Ar buffer gas are reported.

6.3.1 CO-He Collisions

The in-plane and out-of-plane transient signals of CO in levels with $J = 42 - 70$ at a pressure of $5\ \mathrm{Torr}$ with the addition of $0, 5,$ and $10\ \mathrm{Torr}$ helium are shown in Figure 6.3. The full bandwidth optical centrifuge was used for the CO buffer gas experiments. The in-plane transient signals maximize at $J = 62$ and show decreased signal in $J = 70$, indicating an inverted rotational population. The out-of-plane signals decrease with increasing J, highlighting that the higher-J levels have a larger degree of angular momentum orientation. With the addition of $5\ \mathrm{Torr}$ and $10\ \mathrm{Torr}$ He, the transient signals above $J \geq 54$ decrease overall, showing that the addition of He increases the rate of rotational relaxation. The in-plane and out-of-plane transient signals for $J = 70$ decrease by a factor of 2.5 with the addition of $10\ \mathrm{Torr}$ He, whereas the $J = 42$ level retains nearly the same population. The population at the peak of the distribution, $J = 62$, reduces by a factor of two when 10 Torr He is added. Overall, He efficiently removes population from the highest rotational levels, $J = 54$ to 70. The IP and OOP transient signals for the $J = 42$ level are not affected very much, with a standard deviation of 0.04% and 0.02%, respectively, at 200 ns by the addition of He. This observation indicates that this level primarily gains population through the collisional cascade.

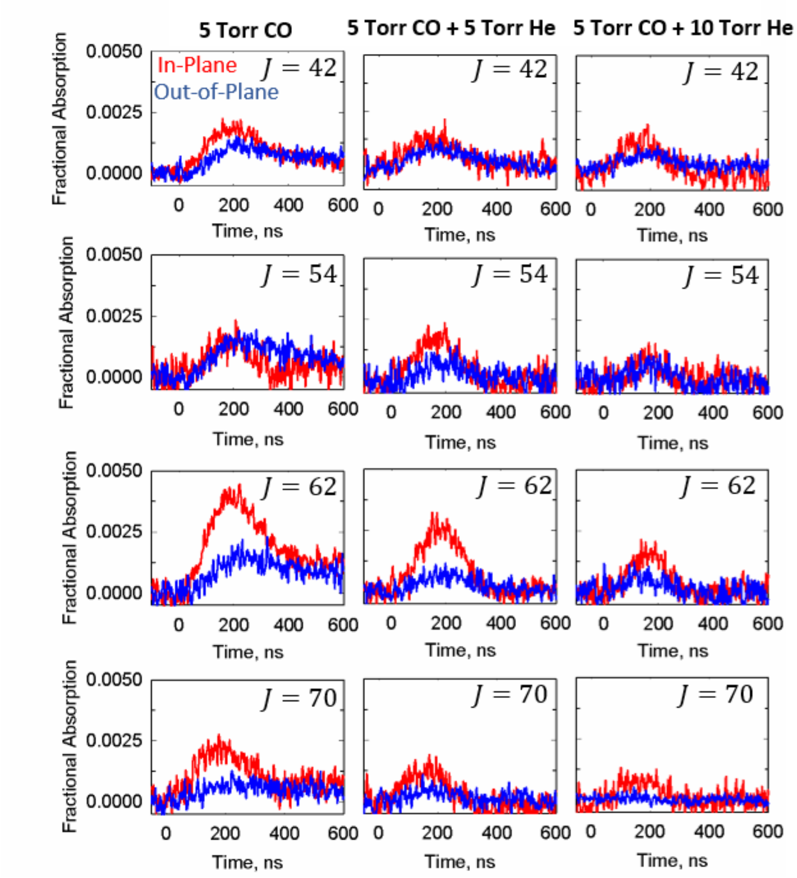

Figure 6.3 In-plane and out-of-plane transient signals of CO $J = 42 - 70$ at a pressure of 5 Torr with 0, 5, and 10 Torr He added.

The in-plane and out-of-plane fractional absorption signals of the CO $J = 42 - 70$ rotational levels with $0, 5,$ and 10 Torr He at three times, $t = 100 - 300$ ns, are shown in Figure 6.4. At a pressure of 5 Torr CO and no He, the distribution peaks at $J = 62$ and an inverted population is shown at the three measurement times. By $t = 300$ ns, the peak of the distribution is still discernible, with population decreases observed at each J-level measured. Significant population still remains at $t = 300$ ns. The relaxation dynamics of the rotational distribution are similar with the addition of 5 Torr He, showing a maximum population in $J = 62$ at $t = 200$ ns, but the overall population in levels $J > 54$ is reduced. The peak of the inverted distribution is also narrower when He is present. With the addition of 10 Torr He, the peak of the distribution at $J = 62$ decreases by a factor of three, and the inverted nature of the distribution is significantly diminished. At $t = 200$ ns and no He, population in $J = 62$ level is more than twice that of $J = 42$. When 10 Torr He is added, the $J = 62$ population is 1.5 times larger than $J = 42$ population at $t = 200$ ns. By $t = 300$ ns, the CO levels with $J \geq 42$ have essentially no population remaining. These data highlight the fact that He is an efficient quencher of rotational energy in CO.

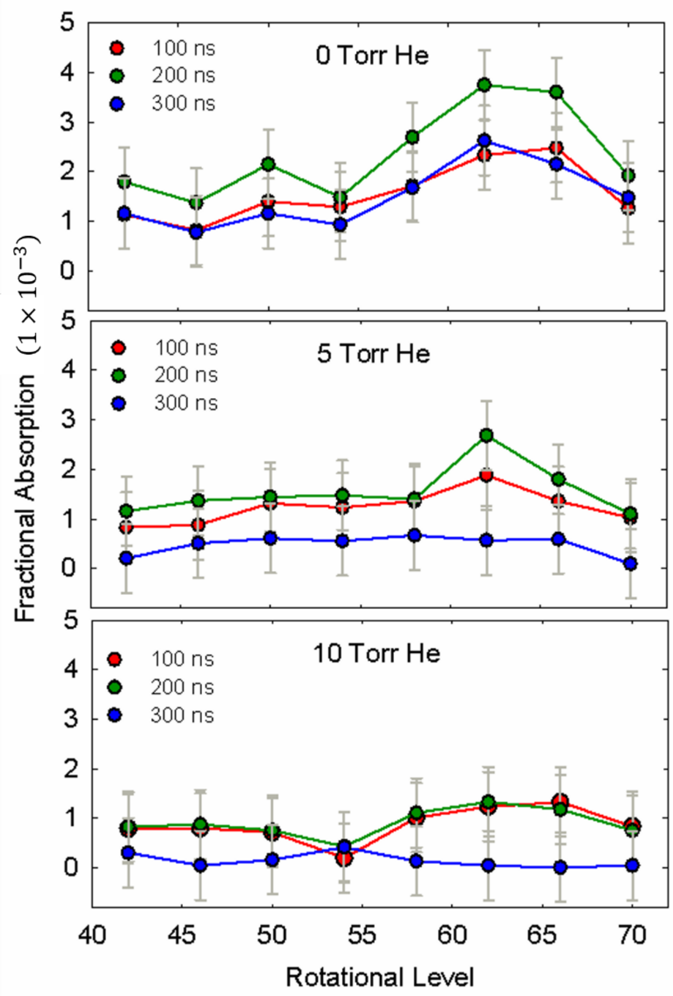

Figure 6.4 Fractional absorption for 5 Torr CO in rotational levels $J = 42$ to 70 over $t = 100$ to 300 ns with the addition of 5 Torr (middle panel) and 10 Torr (bottom panel) He.

The pressure dependence of CO rotational relaxation was investigated using variable He pressures and 4 Torr CO. The fractional absorption signals at $t = 160$ ns are shown in Figure 6.5 for several CO levels with $J = 42, 54,$ and 62 with 0 to 4 Torr He. For $J = 54$ and 62, the transient signals generally decrease with increasing He and have a similar pressure dependence based on a linear fit of the data. For the lowest rotational level measured, $J = 42$, the transient signals remain relatively unchanged overall.

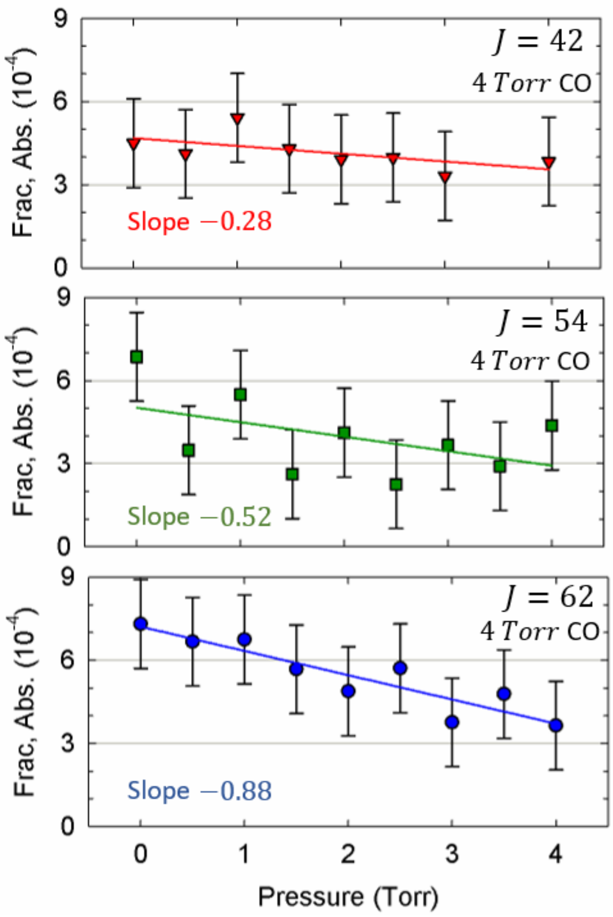

Figure 6.5 Pressure dependence of 4 Torr CO in $J = 42$ to 62 with 0 to 4 Torr He. Fractional absorption measurements taken at $t = 160$ ns and collected with parallel IR polarization.

Figure 6.6 shows Doppler-broadened line profiles of CO in $J = 42$ at $t = 200$ ns and a pressure of 4 Torr with increasing He pressure ranging from 0 to 4 Torr. For $J = 62$, the He pressure ranged from 0 to 2 Torr. The Doppler profiles were collected with vertical IR polarization that is parallel to the plane of molecular rotation. Signals collected using horizontal IR polarization were too small to measure Doppler profiles. The residuals of the Gaussian fit are shown below each Doppler profile. The translational energy was extracted from the FWHM of the fit of each profile.

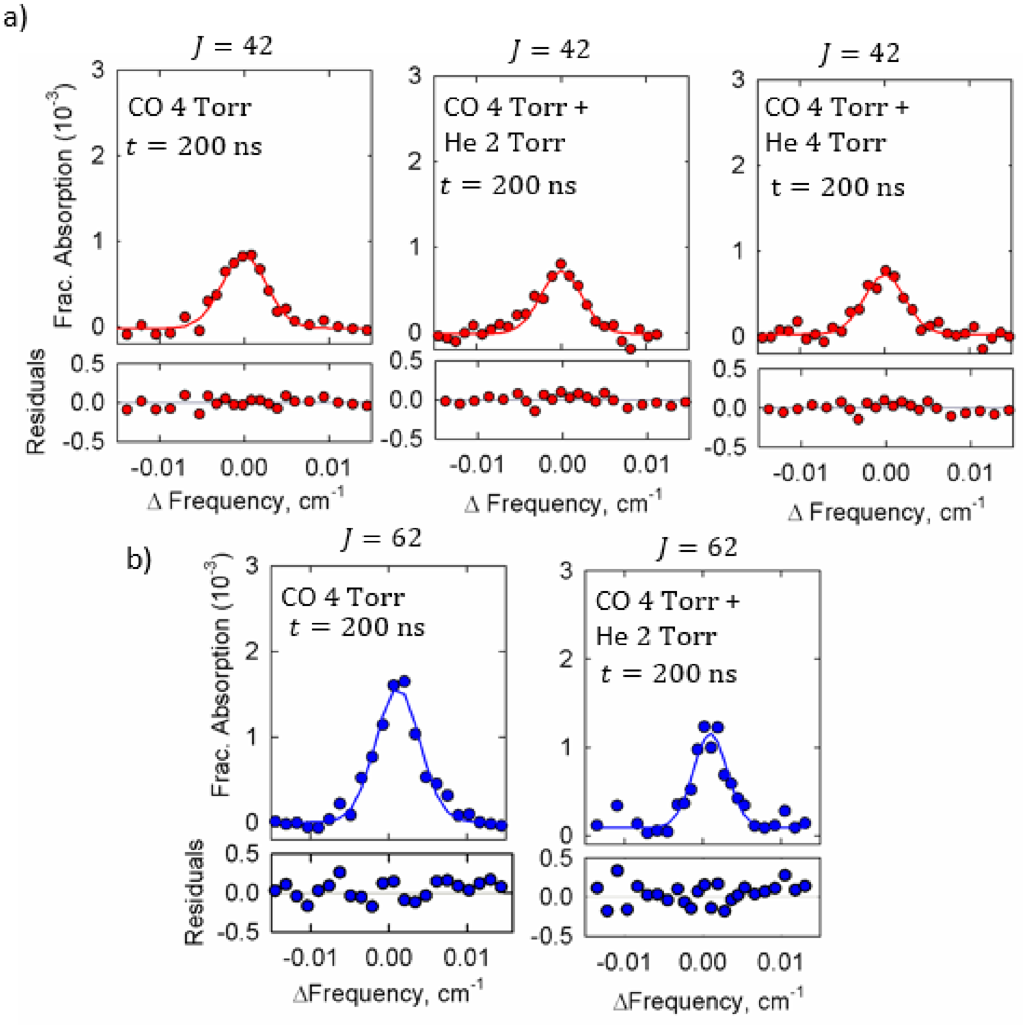

Figure 6.6 a) Doppler-broadened line profiles of 4 Torr CO in $J = 42$ at $t = 200$ ns with increasing He pressure from 0 to 4 Torr. b) Doppler profiles of $J = 62$ at $t = 200$ ns with increasing He pressure from 0 to 2 Torr. Profiles were collected with vertical IR polarization.

Figure 6.7a shows the time-dependent translational energy of molecules in rotational levels with $J = 42$ and $J = 62$ at a pressure of 4 Torr with 0 Torr He. Based on a Lennard-Jones collision rate constant of $k_{LJ} = 2.93 \times 10^{-10}$ cm^{-3} s^{-1} for CO-CO collisions, the average time between collisions at 4 Torr is 26 ns. At $t = 160$ ns (or ~6 collisions), molecules in $J = 42$ and 62 have translational energy near $T = 400$ K. Both levels show little increase in translation from $t = 160$ to 250 ns (6-10 collisions). After $t = 250$ ns, the population is removed from the higher rotational levels and relaxed into lower levels, indicating that the population loss from the $J = 42$ and 62 levels occurs without significant translational energy gain.

Figure 6.7b shows the translational energy in $J = 42$ and 62 at pressures of 4 Torr CO with 2 Torr He added. Based on a Lennard-Jones collision rate constant for CO-He, the average time between collisions is 13 ns at total pressure of 6 Torr. Molecules in $J = 42$ have translational temperatures near $T = 400$ K at $t = 160$ ns (12 collisions). The translational energy for $J = 62$ decreases to temperatures near $T = 300$ K with the addition of He and remains relatively constant throughout $t = 160$ to 250 ns. The cool translational temperatures for the $J = 62$ level that persist through ~12 to 19 collisions on average indicate that these molecules undergo mainly adiabatic collisions with He or collisions with CO from which the scattered molecules have little recoil velocity. This observation also suggests that first set of collisions with He preferentially removes molecules in $J = 62$ with more translation, leaving behind a subset of cooler molecules than were initially prepared in the centrifuge.

Figure 6.7c shows the translational energy of $J = 42$ at a pressure of 4 Torr CO with 4 Torr He added. At 8 Torr total pressure, the average time between collisions is 10 ns. At $t = 160$ ns, the translational energy increases slightly near $T = 500$ K and remains relatively constant through $t = 160$ to 250 ns (~16-25 collisions). The relatively low translational temperatures show that $J = 42$ undergoes mainly adiabatic collisions with He.

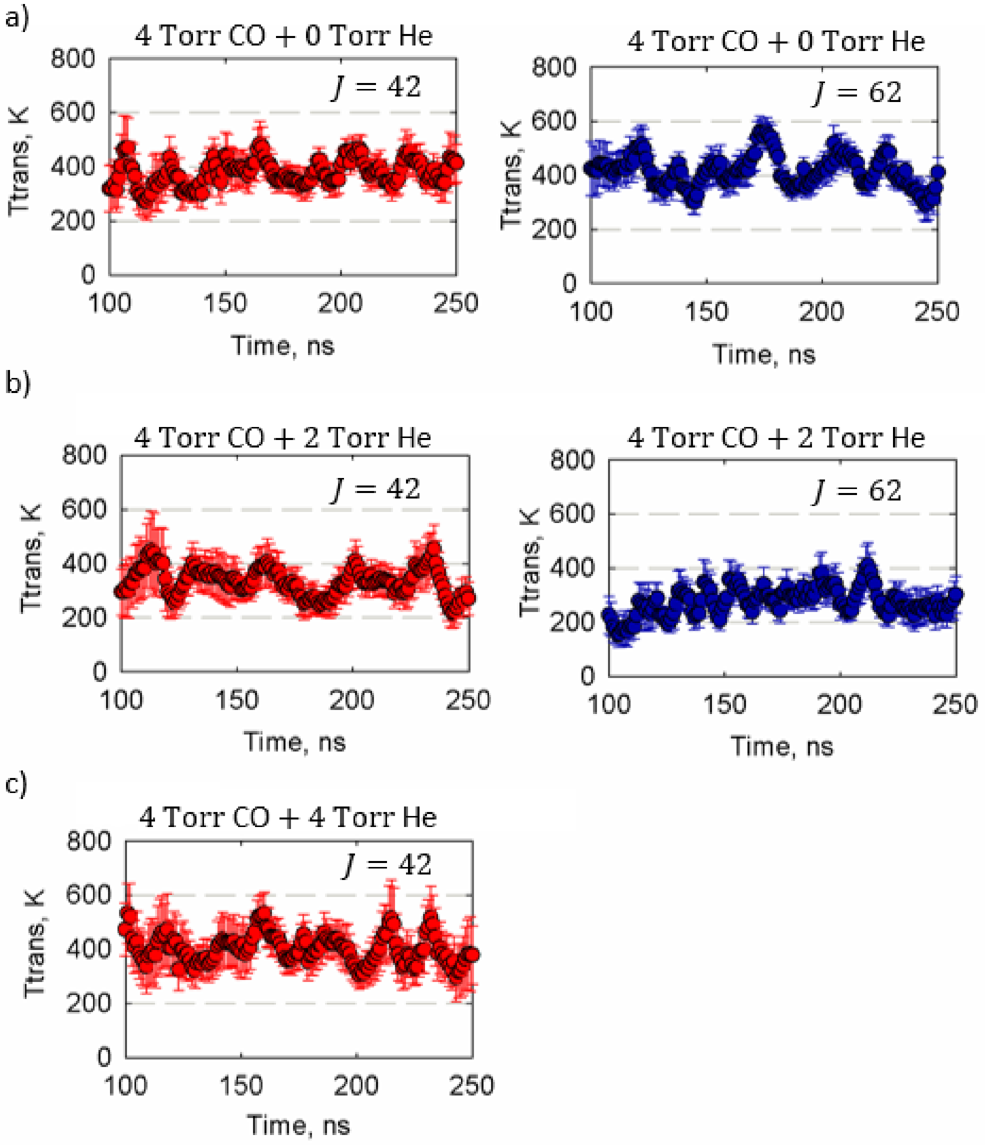

Figure 6.7 Time-dependent translational temperature for CO in $J = 42$ and $J = 62$ at pressures of 4 Torr with a) 0 Torr He, b) 2 Torr He, and c) 4 Torr He.

The data presented here for the collision dynamics of CO and He show that He is an efficient quencher of rotational energy in CO and that little translational energy accompanies the production of CO in rotational levels with $J \geq 42$. The adiabaticity parameter for He-CO collisions has a value of one when $J = 54$, based on the model used here. The translational temperatures for $J = 42$ and 62 with 2 Torr He show the collision products with higher-J levels have lower recoil velocities, and that the collisions that produce $J = 62$ are more adiabatic than collisions that produce $J = 42$. It would be interesting to explore the phenomenon by probing higher-J levels, which is not feasible for CO given that the peak of the centrifuged distribution is at $J = 62$. Instead, we decided to explore higher rotational levels by investigating collisions of optically centrifuged N_2O with He.

6.3.2 N_2O-He Collisions

The collision dynamics between N_2O and He are reported in this section. The optical centrifuge bandwidth was tuned to maximize population in $J = 195$ at a pressure of 5 Torr. Figure 6.8 shows transient signals collected using the full optical bandwidth (black) and the clipped optical bandwidth (red) collected using parallel polarized IR light. The population in $J = 195$ increases by a factor of 7 by reducing the optical bandwidth of the optical centrifuge.

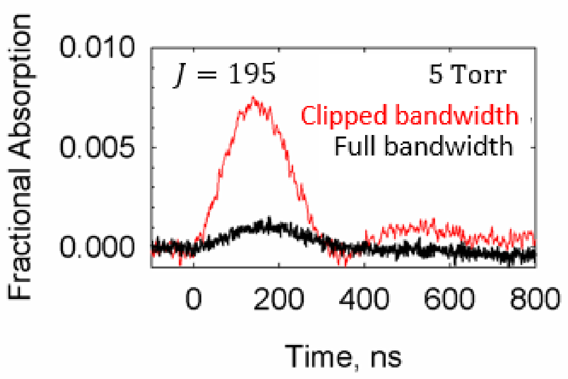

Figure 6.8 Transient signal of $J = 195$ at a pressure of 5 Torr using the full optical bandwidth (black) and clipped optical bandwidth (red) with vertical IR polarization.

Transient signals were collected for N_2O in $J = 92 - 197$ at a pressure of 5 Torr with 0 Torr and 10 Torr He and are shown in Figure 6.9. The transients were collected with parallel polarized IR probe. The 5 Torr N_2O measurements without He (shown in red) show an inverted population distribution that peaks at $J = 195$ and has reduced signal in $J > 196$. Under these conditions, the signal for $J = 195$ is twice the intensity of that for $J = 180$. With the addition of 10 Torr He, the population in $J = 195$ is no longer the peak intensity and is nearly equal to that for $J = 180$, indicating that He collisions lead to efficient rotational energy transfer of N_2O.

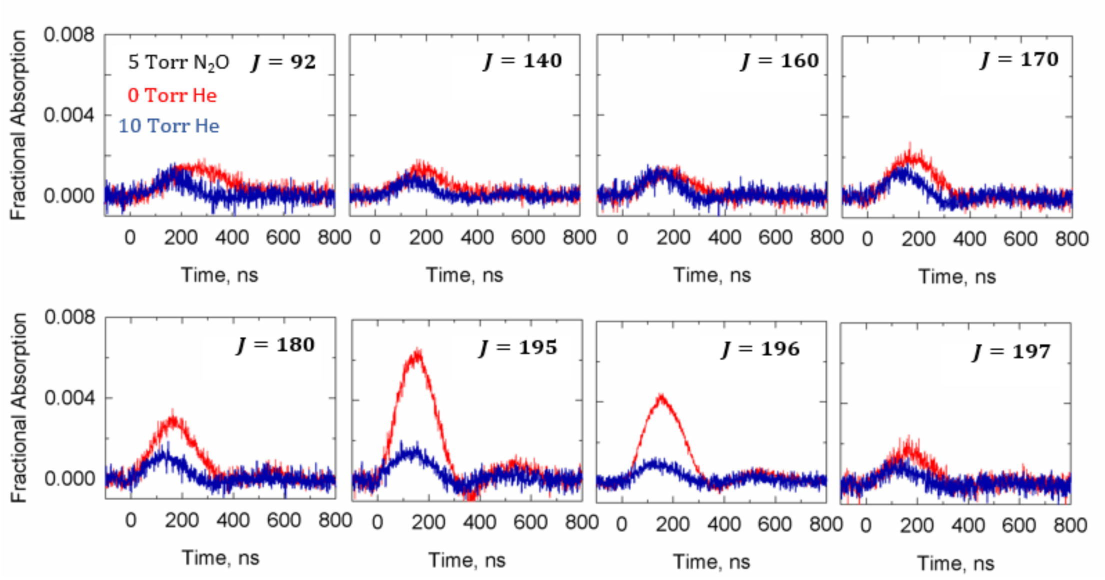

Figure 6.9 Transient absorption signals of N_2O in $J = 92 - 197$ at a pressure of 5 Torr with 0 Torr (red) and 10 Torr (blue) He added. The transient signals were collected with parallel polarized IR light.

Figure 6.10 shows the time-dependent fractional absorption signals of $J = 92 - 197$ from $t = 130 - 250$ ns at a pressure of 5 Torr N_2O and with 10 Torr He. In Figure 6.10a, the inverted population distribution is clear with $J = 195$ showing maximum population at $t = 130$ ns. With the addition of 10 Torr He, the peak of the distribution decreases six-fold at $t = 130$ ns, whereas the fractional absorption in $J = 92$ is essentially unchanged. This observation shows that He rotationally relaxes N_2O rotational levels with $J \geq 170$ efficiently and that lower-J levels are populated by collisional energy transfer. By $t = 250$ ns, without He there is an inverted rotational distribution that peaks at $J = 195$. With the addition of 10 Torr He, the rotational distribution between $J = 140$ to 197 has close to zero population by $t = 250$ ns.

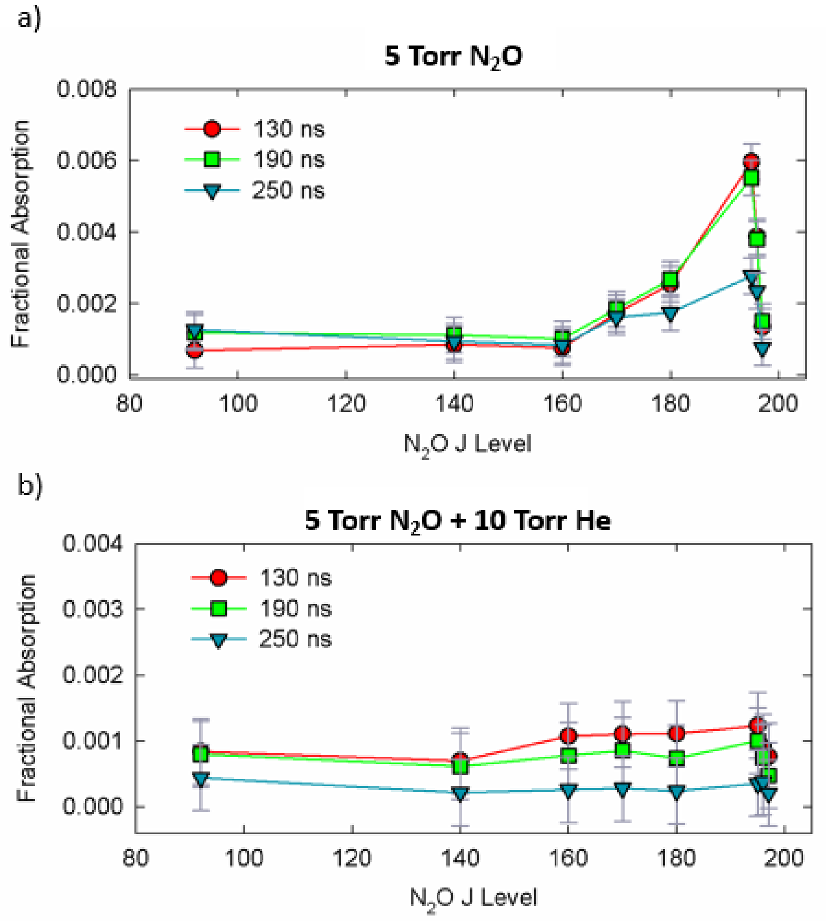

Figure 6.10 Time-dependent fractional absorption of $J = 92 - 197$ collected with parallel polarized IR light at a pressure of 5 Torr N_2O with a) 0 Torr and b) 10 Torr He.

Doppler-broadened line profiles for $J = 140 - 197$ were collected using s-polarized IR light at a pressure of 5 Torr N_2O and with 0 and 10 Torr He. The Doppler profiles were fit to Gaussian functions at $t = 150$ ns and the residuals of the fits are shown below each profile in Figure 6.11.

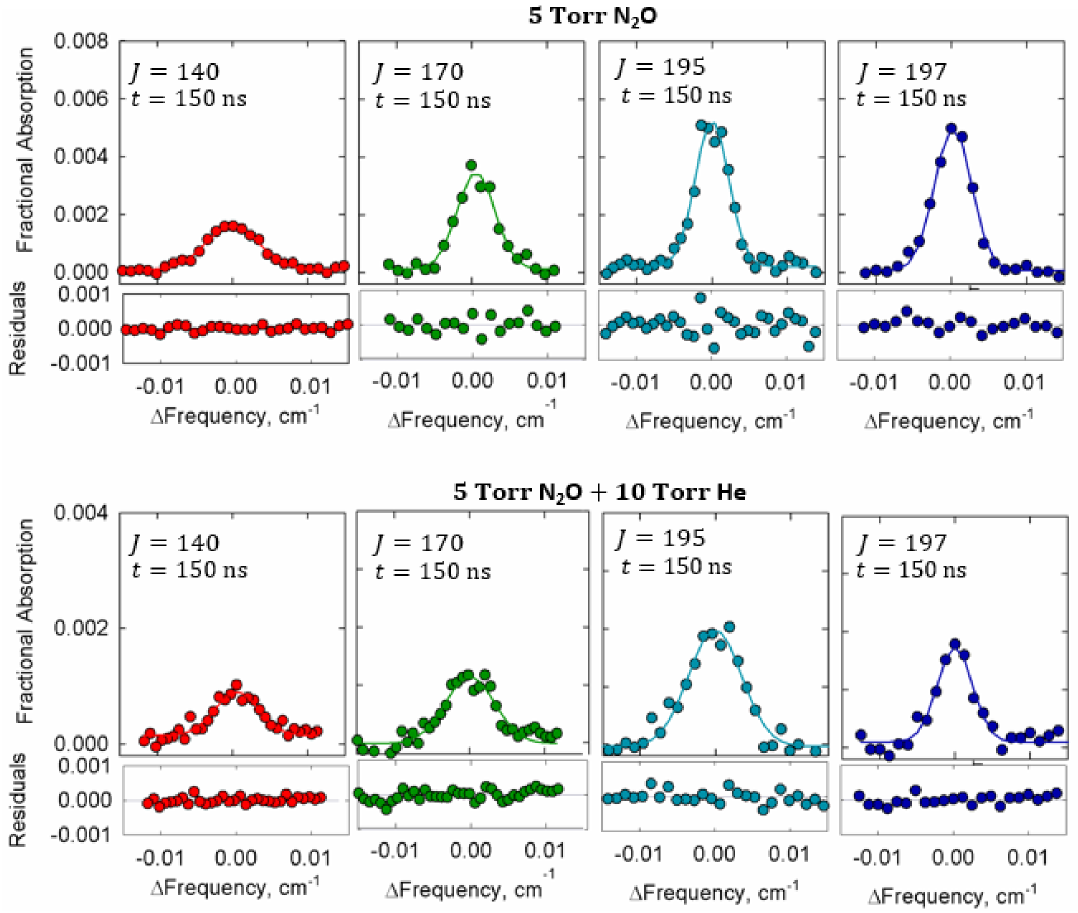

Figure 6.11 Doppler-broadened line profiles for J = 140 to 197 at pressures of 5 Torr N_2O with 0 Torr (top panel) and 10 Torr He (bottom panel) are shown at t = 150 ns after the optical centrifuge pulse.

The translational temperatures are plotted as a function of time for $J = 140 - 197$ at 5 Torr N_2O and with 10 Torr He are shown in Figure 6.12a and 6.12b. The average time between collisions for 5 Torr N_2O is 18 ns and for 15 Torr N_2O-He is 5 ns. In Figure 6.12a, the translational temperature for $J = 195$ with no He present is near $T = 450$ K at $t = 120$ ns. This value persists to $t = 250$ ns (~14 collisions) until population is removed from this level. The $J = 170$ and 197 rotational levels both have translational temperatures initially near $T = 550$ K at $t = 120$ ns (~7 collisions) that steadily increase to $T = 700$ K by $t = 250$ ns. In contrast, N_2O in $J = 140$ has a translational temperature near $T = 900$ K at $t = 120$ ns and the temperature increases to $T = 1300$ K by $t = 250$ ns. The measurements in Figure 6.12a indicate that N_2O molecules with $J \geq 170$ result from collisions that result in very little translational energy gain, while molecules with $J = 140$ result from collisions involving rotation-to-rotation/translation energy transfer.

Adding 10 Torr He has a significant effect on the translational energies of the N_2O molecules, as shown in Figure 6.12b. The $J = 195$ level of N_2O has significantly more translational energy in the presence of He, indicating that He increases the impulsive nature of the relaxing collisions. The $J = 170$ level also has enhanced translation in the presence of He. In contrast, the $J = 140$ level initially has lower translational energy in the presence of He and has a smaller increase in translational temperature over time. Translational energy for the $J = 197$ level remains relatively unchanged in the presence of He.

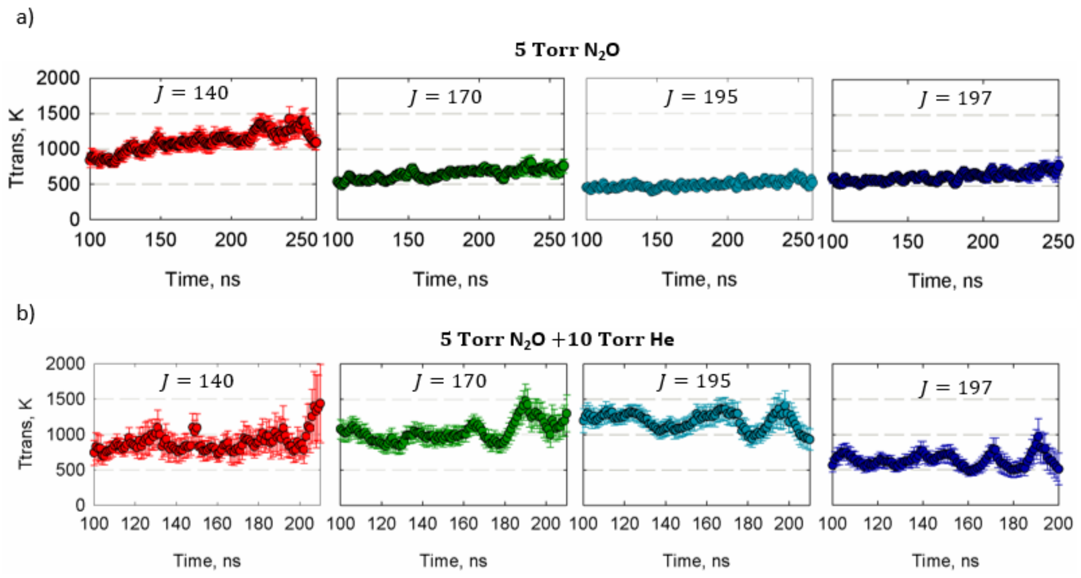

Figure 6.12 Time-dependent translational energy for $J = 140$ to 197 with a) 0 Torr and b) 10 Torr He.

The average translational temperatures of $J = 140$ to 197 at pressures of 5 Torr N_2O with no He added (red circles) and with 10 Torr He added (blue triangles) is shown in Figure 6.13. The 5 Torr measurements are shown at $t = 250$ ns (~14 collisions) and the 15 Torr measurements are shown at $t = 100$ ns (~20 collisions). Without He, the highest levels $J = 195$ to 197 initially exhibit translation near thermal temperatures, with average translational energy decreasing with increasing J. With the addition of 10 Torr He, the $J = 195$ level has translational energy near $T = 1200$ K, while the lower-J levels such as $J = 140$ are translationally cooler with temperatures near $T = 900$ K than when He is absent. The increase in the translational energies of the $J = 195$ molecules in the presence of He shows that He-N_2O collisions are more impulsive than N_2O-N_2O collisions, which come into the adiabatic regime when one of the N_2O molecules is in $J = 44$. Rotational levels between $J = 160$ to 170 are relatively unaffected by the addition of He. It is interesting that levels below $J = 160$ are cooler in the presence of the He buffer gas, whereas levels above $J = 170$ are hotter when He is present. This observation shows that the addition of a He buffer gas can be used to change the J-dependent translational energy release in collisions of centrifuged molecules.

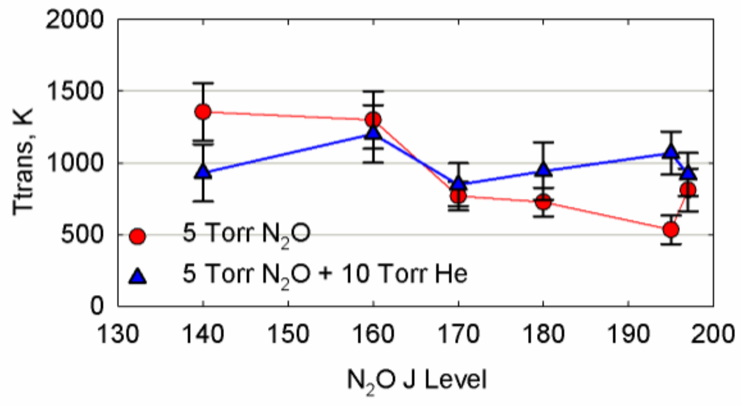

Figure 6.13 Translational temperature for rotational levels $J = 140$ to 197 at 5 Torr (red circles) after ~14 collisions and with 10 Torr He (blue triangles) after ~20 collisions.

6.3.3 N_2O-Ar Collisions

Transient signals of $J = 92$ to 197 at 5 Torr N_2O and with 10 Torr Ar are shown in Figure 6.14. The transient measurements were collected with parallel polarized IR light. Transient signals with 5 Torr N_2O (red) show an inverted population distribution that peaks at $J = 195$. An inverted distribution is also observed with the addition of 10 Torr Ar (blue), but the peak of the distribution shifts to $J = 197$, whereas the other transient signals decrease slightly.

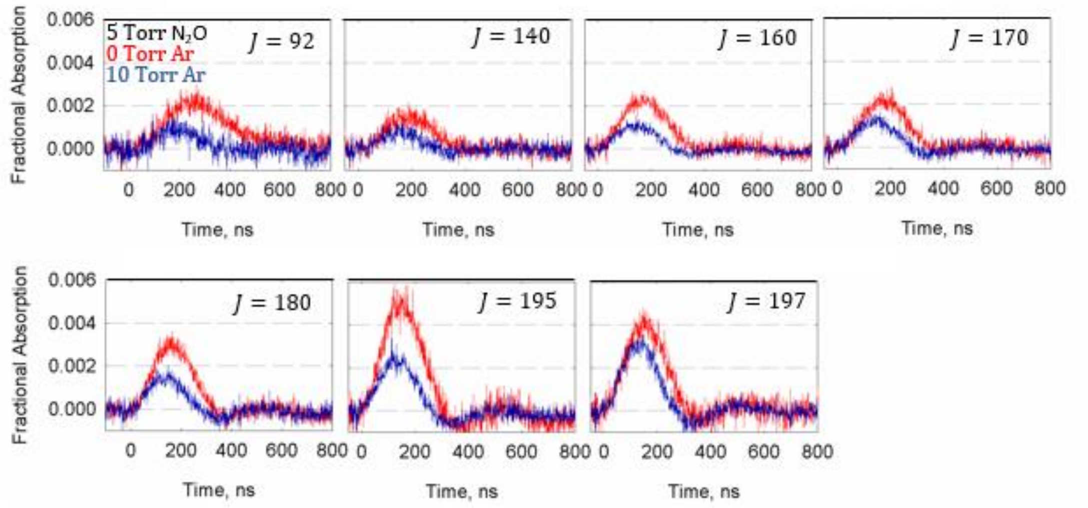

Figure 6.14 Transient absorption signals of 5 Torr N_2O (red) in $J = 92$ to 197 and with 10 Torr Ar added (blue). Measurements were collected with vertical IR polarization.

Time-dependent fractional absorption signals are shown in Figure 6.15 at three times from $t = 130$ to 250 ns of a) 5 Torr N_2O and b) with 10 Torr Ar added. In the 5 Torr measurements, the $J = 195$ level is the peak of the distribution at $t = 130$ ns. All levels measured relax over time out to $t = 250$ ns, except for $J = 140$, which remains constant, and $J = 92$, which grows in the collisional cooling of higher-J levels. With the addition of 10 Torr Ar, the transient signals show reduced population for all levels at $t = 130$ ns. The inverted population distribution is still visible with a maximum at $J = 197$. With the addition of Ar, the population in $J = 195$ is reduced by 40%, whereas that for $J = 197$ is reduced by 20% at $t = 130$ ns. In comparison, the $J = 195$ level in Figure 6.10 is reduced by 79% and $J = 197$ is reduced by 76% with the addition of He. This observation indicates that Ar is less efficient than He at rotationally relaxing the high-J N_2O levels with $J \geq 195$. By $t = 250$ ns the population in the high-J approaches zero.

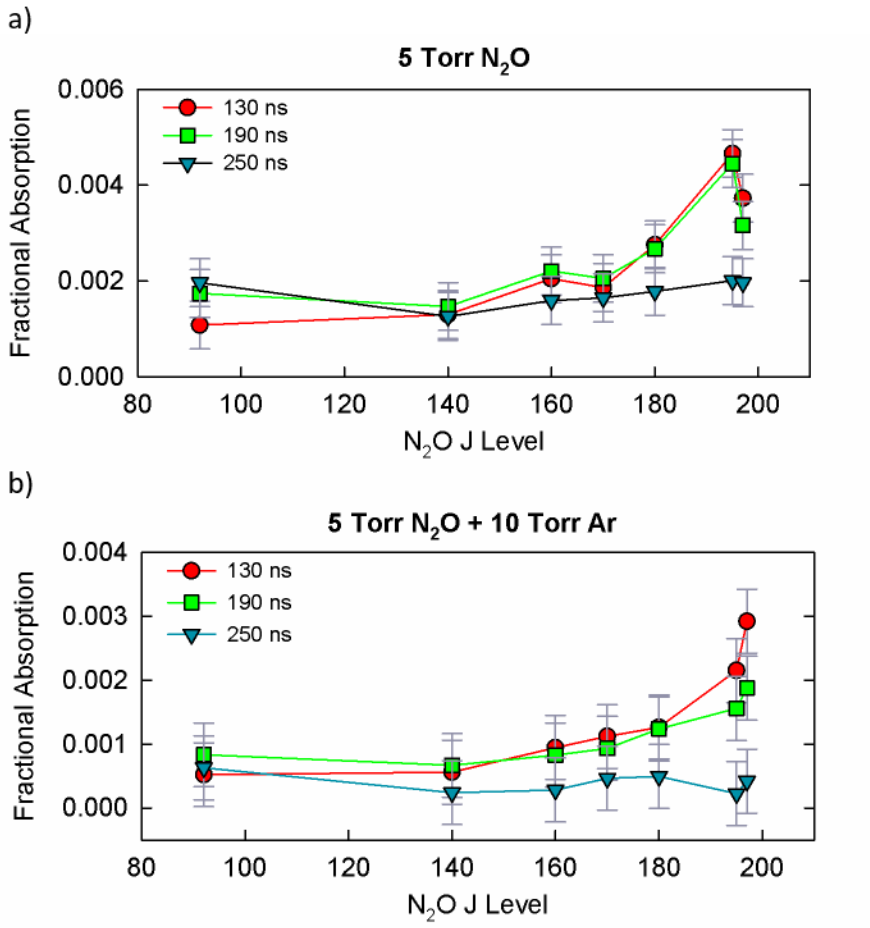

Figure 6.15 Time-dependent fractional absorption from $t = 130$ to 250 ns of a) 5 Torr N_2O and b) with 10 Torr Ar added.

Doppler-broadened line profiles were collected for N_2O in $J = 195$ to 197 at a partial pressure of 5 Torr with 10 Torr Ar and are shown in Figure 6.16. The profiles are shown at $t = 150$ ns and the residuals of the Gaussian fits are shown below each profile. At a total pressure of 15 Torr, the average time between N_2O and Ar collisions is 7 ns. At $t = 100$ ns (~14 collisions) molecules with $J = 195$ have translational temperatures near $T = 780$ K. Molecules with $J = 197$ have cooler translational temperatures near $T = 600$ K. Both rotational levels gain little translation from $t = 100$ to 220 ns (~14 to 31 collisions).

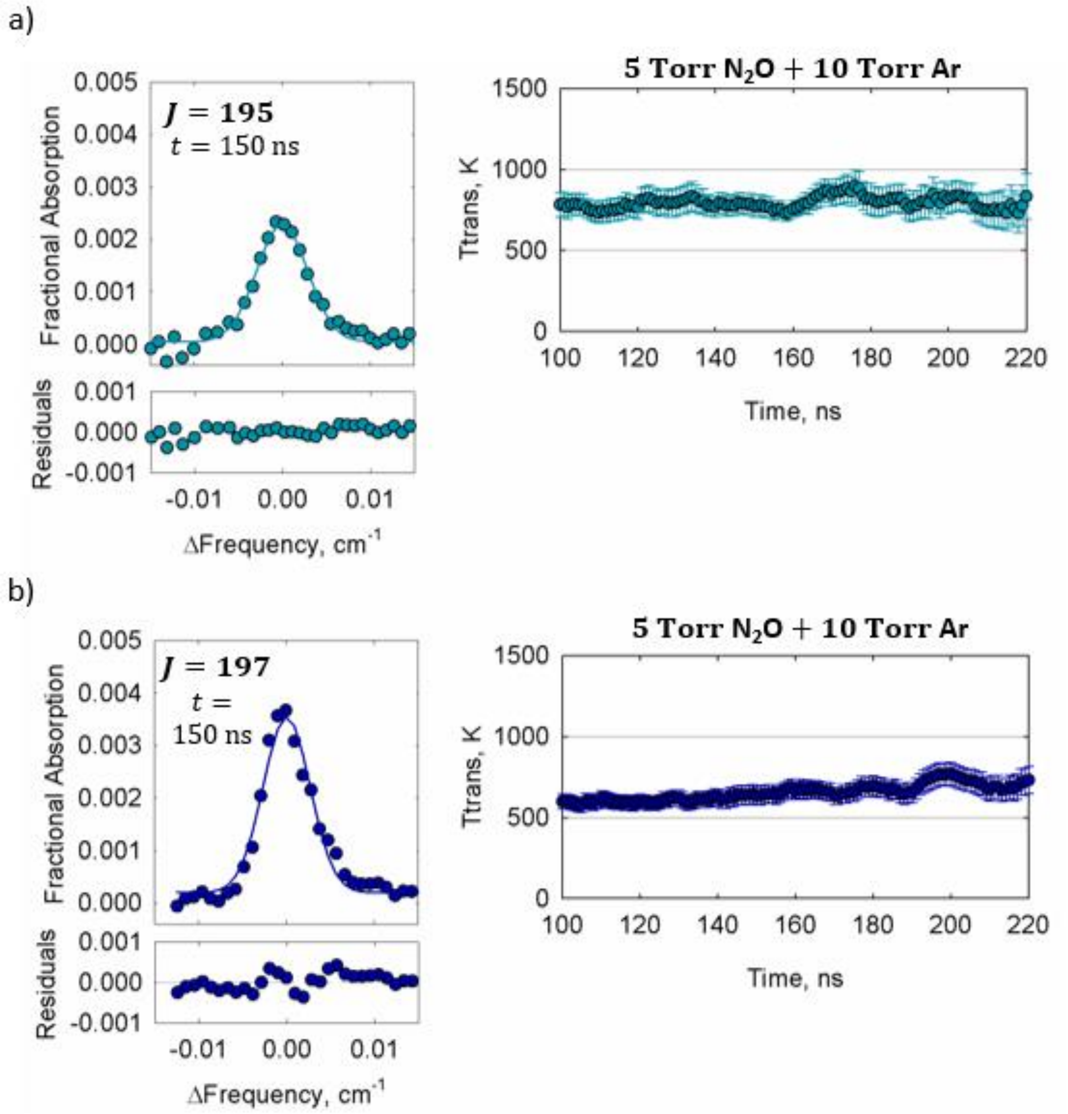

Figure 6.16 Doppler broadened line profile at $t = 150$ ns and time-dependent translational energy from $t = 100$ to 220 ns for a) $J = 195$ and b) $J = 197$ at a pressure of 4 Torr N_2O with 10 Torr Ar.

A comparison of translational temperatures of $J = 195$ and 197 at 5 Torr N_2O (red circles), with 10 Torr He (blue squares), and with 10 Torr Ar (green triangles) is shown in Figure 6.17. The data are shown after ~14 collisions for 5 Torr N_2O ($t = 250$ ns) and with 10 Torr Ar ($t = 100$ ns), and after ~20 collisions with 10 Torr He ($t =$

$100\ \mathrm{ns}$). For the $J = 195$ level, collisions with He lead to larger recoil than do collisions with Ar or N_2O, indicating that He collisions are more impulsive than the other two partners. For $J = 197$, collisions with Ar and He are more adiabatic.

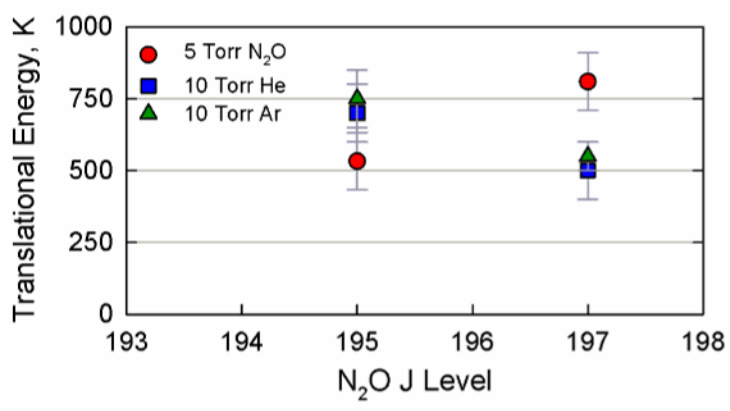

Figure 6.17 Translational temperature of $J = 195$ to 197 at 5 Torr N_2O (red circles) with 10 Torr He (blue squares) and 10 Torr Ar (green triangles). The data shown are after 14 collisions for 5 Torr N_2O ($t = 250$ ns) and with 10 Torr Ar ($t = 100$ ns), and are shown at 20 collisions with 10 Torr He ($t = 100$ ns).

Conclusions

The collision dynamics of CO super rotors in $J = 42$ to 70 and N_2O super rotors in $J = 92$ to 197 with He and Ar buffer gases are explored here. Transient absorption signals and Doppler-broadened line profiles reveal that He collisions lead to faster quenching and larger recoil than collisions with Ar, indicating more sudden collisional energy transfer. Interestingly, the $J = 197$ rotational level of N_2O gains less translational energy with both buffer gasses as a collision partner than $J = 195$. This suggests that $J = 197$ with rotational angular frequency of 3.11×10^{13} radians s^{-1} could be in a transition regime between the adiabatic (where $a > 1$) and sudden (where $a \leq 1$) collision regimes. Future studies on N_2O-He super rotor collisions above $J = 197$ would help investigate the role of extreme rotational motion in molecular collisions.

Chapter 7: Conclusions and Future Work

The optical centrifuge is a powerful optical method that non-resonantly drives molecules with anisotropic polarizability to rotational levels far beyond thermal equilibrium. In the work presented here, three different optical centrifuge traps were used to rotationally excite N_2O, CO, and CO_2 to high-J levels. The collision dynamics of the rotationally excited samples were investigated using a high-resolution transient IR absorption spectrometer. The optical centrifuge prepares an ensemble of molecules with oriented angular momentum vectors. Polarization-dependent transient absorption measurements yield information on the reorientation dynamics and energy transfer as well as absolute number densities and new IR spectral transitions.

In Chapters 3 and 4, the nearly-nascent rotational distributions of N_2O and CO were prepared using a reduced and full bandwidth optical centrifuge, and characterized with polarization-dependent transient absorption measurements. The results show that the nearly-nascent molecules prepared by the optical centrifuge have an inverted population distribution that is highly anisotropic, exhibit gyroscopic behavior, and have cool translational temperatures that persist throughout several collisions. Population was measured in rotational levels for N_2O up to $J = 205$ ($E_{rot} = 17,380\ \text{cm}^{-1}$) and for CO up to $J = 67$ ($E_{rot} = 8{,}650\ \text{cm}^{-1}$) using the reduced bandwidth trap, and for CO up to $J = 80$ ($E_{rot} = 12,300\ \text{cm}^{-1}$) using the full bandwidth trap. This was the first observation of how much angular momentum the full bandwidth optical centrifuge imparts to CO and provides an indication of how much of the spectral bandwidth is used in the acceleration process.

Doppler-broadened line profiles shown in Chapters 3 and 4 reveal that N_2O molecules in $J = 195$ have translational temperatures near $T = 500$ K after ~2 collisions, whereas CO molecules in $J = 75$ have sub-thermal temperatures near $T = 240$ K. The translational broadening observed for $J = 195$ indicates that the optical centrifuge initially prepares N_2O molecules well above $J = 200$. The nascent distribution of N_2O prepared by the full bandwidth optical centrifuge has not been measured yet due to limitations in the IR range of the current experimental set up, as well as unknown IR spectral transitions above $J = 205$. It would be interesting to extend the IR tuning range in our transient spectrometer to observe the extent of N_2O molecular excitation using the full bandwidth trap as well as to measure new IR spectral transitions and collision dynamics of N_2O molecules above $J = 205$.

The transient measurements collected for the nearly-nascent distributions of N_2O and CO using the reduced and full bandwidth optical centrifuges revealed that the slope of the rotational distribution mimics the intensity profile of the optical trap. This was our first indication that we could selectively populate rotational levels by changing the spectral bandwidth of the optical trap, leading to a tunable optical centrifuge.

A tunable optical centrifuge was used in Chapter 5 to explore how the molecular properties of CO and CO_2, such as polarizability anisotropy and moment of inertia, affect the capture and acceleration efficiecies in the optical trap. Total number densities measured for the nascent distributions show that the optical centrifuge captures and accelerates about 3% CO_2 and about 2% CO from the total gas sample. The nascent distributions reveal that the critical optical trap intensity to hold onto the molecules is larger for CO than for CO_2, causing CO molecules to be released from the trap sooner and leading to a broader distribution than for CO_2. Parameters of the optical centrifuge can now be tuned to maximize the number density of captured molecules in select rotational levels.

The tunable optical centrifuge opens the door to more targeted studies of molecules in select rotational levels. Varying the optical centrifuge chirp rate could also expand the range of molecular species captured and accelerated to include heavier or non-symmetric molecules. MacPhail *et. al.* have recently shown in molecular simulations that a slow centrifuge with a chirp rate of 0.017 rad ps^{-2} could capture and excite nearly ~20% of a propylene oxide sample.[51] MacPhail *et. al.* describe the parameters needed to create a "fast" and "slow" optical centrifuge by changing the groove density and distance between the double-pass double-grating stretcher in the pulse shaper.[51] A tunable centrifuge with a variable chirp rate could allow the exploration of more complex reactions involving heavier molecules with large amounts of angular momentum.

The efficiency of collisional energy transfer between CO and N_2O super rotors with He and Ar buffer gases were explored in Chapter 6. The results reveal that He collisions lead to faster rotational quenching and larger recoil than collisions with Ar, indicating more sudden collisional energy transfer. Interesting collision dynamics were observed for N_2O super rotors in rotational levels between $J = 195$ to 197 with He and Ar. Doppler profiles reveal small translational energy gain for N_2O molecules in $J = 197$ from collisions with both buffer gases, whereas molecules in $J = 195$ gain substantially more translation with the addition of buffer gas. This observation suggests that the $J = 197$ $(\Omega = 3.11 \times 10^{13} rad\, s^{-1})$ rotational level could be in a transition between the adiabatic and sudden collision regimes. Molecular dynamic simulations of centrifuged N_2 by Khodorkovsky *et. al.* describe two stages of super rotor relaxation: a period of inhibited rotation-to-translation relaxation due to a high value of the adiabaticity parameter $(a \gg 1)$, followed by an explosive release of rotation-to-translation energy transfer based on the role of chain reactions first proposed by Semenov.[49,52] Khodorkovsky states that the shape of the transition stage between the two regimes is determined by the dynamics of the collision products and the distribution of the collision events. The transition between adiabatic and sudden collision regimes can be explored further by extending the IR tunability for N_2O above $J = 205$ to investigate the role of extreme rotational motion in molecular collisions.

The results reported here add to the growing body of knowledge surrounding super rotor molecules. The development of the tunable optical centrifuge will help increase signal-to-noise in the nascent rotational distributions and could provide more targeted studies of specific rotational levels and interactions. It would be interesting to change the chirp rate of the centrifuge in addition to a tunable bandwidth. A slower accelerating chirp rate could trap heavier or nonlinear molecules. Polarization-dependent studies of a nonlinear molecule accelerated by the optical trap would investigate the principal axis that interacts with the field. Overall, the optical centrifuge is a powerful tool to understand the behavior and energy transfer processes involved in high energy molecules.

Bibliography

[1] Wainger, M; Al-Agil, I; Brunner, T. A.; Karp, A. W.; Smith, N.; Pritchard, D. E. Power Law Scaling of Rotational Energy Transfer in $\mathrm{Na}_2^*(\mathrm{A}\Sigma)$ + He. *J. Chem. Phys.* **1979**, *71*, 1977-1978.

[2] Brunner, T. A.; Smith, N.; Karp, A. W.; Pritchard, D. E. Rotational Energy Transfer $\mathrm{Na}_2^*(\mathrm{A}\Sigma)$ Colliding with Xe, Kr, Ar, Ne, He, H_2, CH_4, and N_2: Experiment and Fitting Laws. *J. Chem. Phys*. **1981**, *71*, 3324-3341.

[3] Cohen, J. B.; Bright Wilson, E. Rotational Energy Transfer in Pure HCN and in HCN-Rare Gas Mixtures by Microwave Double Resonance and Pressure Broadening. *J. Chem. Phys.* **1973**, *58*, 442-455.

[4] James, P. L.; Sims, I. R.; Smith, I. W. M.; Alexander, M. H.; Yang, M. A. A Combined Experimental and Theoretical Study of Rotational Energy Transfer in Collisions Between NO $\left(X^2\Pi_{1/2}, v = 3, J\right)$ and He, Ar, and N_2 at Temperatures Down to 7 K. *J. Chem. Phys.* **1998,** *109*, 3882-2897.

[5] Mccaffery, A. J.; Proctor, M. J.; Whitaker, B. J. Rotational Energy Transfer: Polarization and Scaling. *Ann. Rev. Phys. Chem.* **1986**, *37*, 223-244.

[6] Mullin, A. S.; Park, J.; Chou, J. Z.; Flynn, G, W.; Weston, R. E. Some Rotations Like It Hot: Selective Energy Partitioning in the State Resolved Dynamics of Collisions between CO_2 and Highly Vibrationally Excited Pyrazine. *Chem. Phys.* **1993**, *175* (1), 53-70.

[7] Dexheimer, S. L.; Durand, M.; Brunner, T. A.; Pritchard, D. E. Dynamical Constraints on the Transfer of Angular Momentum in Rotationally Inelastic Collisions of I_2 $(B^3\Pi)$ with He and Xe. *J. Chem. Phys*. **1982**, *76*, 4996-5004.

[8] Magill, P. D.; Scott, T. P.; Smith, N.; Pritchard, D. E. Level-to-Level Vibrationally Inelastic Rate Constants for Li_2^*-X (X=He, Ne, Ar, Xe) Collisions. *J. Chem. Phys.* **1989**, *90,* 7195-7206.

[9] Barnes, J. A.; Keil, M.; Kutina, R. E.; Polanyi, J. C. Laser Double-Resonance Measurements of Rotational Relaxation Rates of HF $(J = 13)$ with Rare Gases, H_2 and D_2. *J. Chem. Phys.* **1980**, *72*, 6306-6308.

[10] Callear, A. B.; Hedges, R. E. M. Rotational and Vibrational Relaxation of He_2 $a^3\Sigma_u^+$. *Faraday Society*. **1970**, *92*, 2921-2935.

[11] Stahlberg, B.; Baev, V. M.; Gaida, G.; Schroder, H.; Toschek, P. E. Laser Intracavity Absorption Spectroscopy of He_2 $(a^3\Sigma_u^+)$. **1985**, *81*, 207-216.

[12] Northby, J. A.; Yurgenson, S.; Kim, C. Detachment Spectroscopy of Metastable

Excitations in Helium Nanodroplets. *J. Low Temp. Phys.* **1995**, *101*, 427-432.

[13] Sung, J. P.; Setser, D. W. Observation of High Rotational Levels of HF Formed by Chemical Reaction in One Torr of Ar Buffer Gas. *J. Chem. Phys*. **1978**, *69*, 3868-3869.

[14] Hay, S.; Shokoohi, F.; Callister, S.; Wittig, C. Collisional Metastability of High Rotational States of CN$(X^2\Sigma^+, v" = 0)$. *Chem. Phys. Lett.* **1985**, *118* (1), 6-11.

[15] Sivakumar, N.; Hall, G. E.; Houston, P. L.; Hepburn, J. W.; Burak, I. State-Resolved Photodissociation of OCS Monomers and Clusters. *J. Chem. Phys*. **1988**, *88* (6), 3692-3708.

[16] Wei, W.; Wallace, C. J.; Mcbane, G. C.; North S. W. Photodissociation Dynamics of OCS Near 214 nm Using Ion Imaging. *J. Chem. Phys*. **2016**, *145*, 24310.

[17] Ma, Y.; Liu, J.; Li, F.; Wang, F.; Kitsopoulos, T. N. Roaming Dynamics in the Photodissociation of Formic Acid at 230 nm. *J. Phys. Chem. A.* **2019**, *123*, 3672-3677.

[18] Gong, M.; Ostriker, E. C.; Wolfire, M. G. A Simple and Accurate Network for Hydrogen and Carbon Chemistry in the Interstellar Medium. *Astrophys. J.* **2017**, *843*, 38.

[19] Brogi, M.; De Kok, R. J.; Birkby, J. L.; Schwarz, H.; Snellen, I. A. G. Carbon Monoxide and Water Vapor in the Atmosphere of the Non-Transiting Exoplanet HD 179949 B. *Astron. Astrophys.* **2014**, *565*, A124.

[20] Joblin, C.; Bron, E.; Pinto, C.; Pilleri, P.; Le Petit, F.; Gerin, M.; Le Bourlot, J.; Fuente, A.; Berne, O.; Goicoechea, J. R.; Habart, E.; Köhler, M.; Teyssier, D.; Nagy, Z.; Montillaud, J.; Vastel, C.; Cernicharo, J.; Röllig, M.; Ossenkopf-Okada, V.; Bergin, E. A. Astrophysics Structure of Photodissociation Fronts in Star-Forming Regions Revealed by Herschel Observations of High-J CO Emission Lines. *A&A.* **2018**, *615*, 129.

[21] Bernath, P. F. Molecular Opacities for Exoplanets. *Phil. Trans. R. Soc. A.* **2014**, *372*, 20130087.

[22] Bailly, D.; Camy-Peyret, C.; Lanquetin, R. Temperature Measurement in Flames through CO_2 and CO Emission: New Highly Excited Levels of CO_2. *J. Molec. Spec.* **1997**, *182*, 10-17.

[23] Taatjes, C. A.; Leone, S. R. Laser Double-Resonance Mesurements of Rotational Relaxation Rates of HF ($J = 13$) with Rare Gases, H_2, and D_2. *J. Chem. Phys.* **1988**, *89* (1), 302–308.

[24] Villeneuve, D. M.; Aseyev, S. A.; Dietrich, P.; Spanner, M.; Ivanov, M. Y.; Corkum, P. B. Forced Molecular Rotation in an Optical Centrifuge; **2000**, *85* (3), 542-545.

[25] Armon, T.; Friedland, L. Quantum versus Classical Dynamics in the Optical Centrifuge. *Phys. Rev. A* **2017**, *96*, 33411.

[26] Yardley, T. Introduction to Molecular Energy Transfer; Academic Press, New York, **1980**.

[27] Phipps, S. P.; Smith, T. C.; Hager, G. D.; Heaven, M. C.; McIver, J. K.; Rudolph, W. G. Investigation of the State-to-State Rotational Relaxation Rate Constants for Carbon Monoxide (CO) Using Infrared Double Resonance. *J. Chem. Phys.* **2002**, *116* (21), 9281–9292.

[28] Yuan, L.; Toro, C.; Bell, M.; Mullin, A. S. Spectroscopy of Molecules in Very High Rotational States Using an Optical Centrifuge. *Faraday Discussions*. **2011**, 101–111.

[29] Toro, C.; Liu, Q.; Echebiri, G. O.; Mullin, A. S. Inhibited Rotational Quenching in Oriented Ultra-High Rotational States of CO_2. *Mol. Phys.* **2013**, *111* (12–13), 1892–1901.

[30] Murray, M. J.; Ogden, H. M.; Mullin, A. S. Importance of Rotational Adiabaticity in Collisions of CO_2 Super Rotors with Ar and He. *J. Chem. Phys.* **2018**, *148* (8), 84310.

[31] Ogden, H. M.; Michael, T. J.; Murray, M. J.; Mullin, A. S. Transient IR (00^01–00^00) Absorption Spectroscopy of Optically Centrifuged N_2O with Extreme Rotation up to $J = 205$. *J. Quant. Spectrosc. Radiat. Transf.* **2020**, *246*,, 106867.

[32] Karczmarek, J.; Wright, J.; Corkum, P.; Ivanov, M. Optical Centrifuge for Molecules; **1999**, *82*, 3420-3423.

[33] Toth, R. A. N_2O Vibration–Rotation Parameters Derived from Measurements in the 900–1090 and 1580–2380 cm^{-1} Regions. *J. Opt. Soc. Am. B.* **1987**, *4* (3), 357-374.

[34] Esplin, M. P.; Barowy, W. M.; Huppi, R. J.; Vanasse, G. A. High Resolution Fourier Spectroscopy of Nitrous Oxide at Elevated Temperatures. *Mikrochim. Acta*. **1988**, *95* (1–6), 403–407.

[35] Morino, I.; Yamada, K. M. T.; Maki, A. G. Terahertz Measurements of Rotational Transitions in Vibrationally Excited States of N_2O. *J. Mol. Spectrosc.*

1999, *196* (1), 131–138.

[36] Bailly, D.; Vervloet, M. $^{14}N_2{}^{16}O$ in Emission in the 4.5-Mm Region: Transitions V1 V2/ V3 → V1 V2/ (V3 - 1) Occurring between Highly Excited Vibrational States. *J. Mol. Spectrosc.* **2001**, *209* (2), 207–215.

[37] Bailly, D.; Pirali, O.; Vervloet, M. $^{14}N_2{}^{16}O$ Emission in the 4.5 MM Region: High Excitation of the Bending Mode Transitions V1v2lv3 → V1v2l(v 3 - 1) with (2v1 + v2) = 5. *J. Mol. Spectrosc.* **2003**, *222* (2), 180–190.

[38] Ting, W. J.; Chang, C. H.; Chen, S. E.; Chen, H. C.; Shy, J. T.; Drouin, B. J.; Daly, A. M. Precision Frequency Measurement of N_2O Transitions near 45 Mm and above 150 Mm. *J. Opt. Soc. Am. B.* **2014**, *31* (8), 1954.

[39] Perevalov, V. I.; Tashkun, S. A.; Kochanov, R. V.; Liu, A. W.; Campargue, A. Global Modeling of the $^{14}N_2{}^{16}O$ Line Positions within the Framework of the Polyad Model of Effective Hamiltonian. *J. Quant. Spectrosc. Radiat. Transf.* **2012**, *113* (11), 1004–1012.

[40] Tashkun, S. A.; Perevalov, V. I.; Lavrentieva, N. N. NOSD-1000, the High-Temperature Nitrous Oxide Spectroscopic Databank. *J. Quant. Spectrosc. Radiat. Transf.* **2016**, *177*, 43–48.

[41] Hargreaves, R. J.; Gordon, I. E.; Rothman, L. S.; Tashkun, S. A.; Perevalov, V. I.; Lukashevskaya, A. A.; Yurchenko, S. N.; Tennyson, J.; Müller, H. S. P. Spectroscopic Line Parameters of NO, NO_2, and N_2O for the HITEMP Database. *J. Quant. Spectrosc. Radiat. Transf.* **2019**, *232*, 35–53.

[42] Gordon, I. E.; Rothman, L. S.; Hill, C.; Kochanov, R. V.; Tan, Y.; Bernath, P. F.; Birk, M.; Boudon, V.; Campargue, A.; Chance, K. V.; Drouin, B. J.; Flaud, J. M.; Gamache, R. R.; Hodges, J. T.; Jacquemart, D.; Perevalov, V. I.; Perrin, A.; Shine, K. P.; Smith, M. A. H.; Tennyson, J.; Toon, G. C.; Tran, H.; Tyuterev, V. G.; Barbe, A.; Császár, A. G.; Devi, V. M.; Furtenbacher, T.; Harrison, J. J.; Hartmann, J. M.; Jolly, A.; Johnson, T. J.; Karman, T.; Kleiner, I.; Kyuberis, A. A.; Loos, J.; Lyulin, O. M.; Massie, S. T.; Mikhailenko, S. N.; Moazzen-Ahmadi, N.; Müller, H. S. P.; Naumenko, O. V.; Nikitin, A. V.; Polyansky, O. L.; Rey, M.; Rotger, M.; Sharpe, S. W.; Sung, K.; Starikova, E.; Tashkun, S. A.; Auwera, J. Vander; Wagner, G.; Wilzewski, J.; Wcisło, P.; Yu, S.; Zak, E. J. The HITRAN2016 Molecular Spectroscopic Database. *J. Quant. Spectrosc. Radiat. Transf.* **2017,** *203*, 3–69.

[43] Yuan, L.; Teitelbaum, S. W.; Robinson, A.; Mullin, A. S. Dynamics of Molecules in Extreme Rotational States. *Proc. Natl. Acad. Sci. U. S. A.* **2011,** *108* (17), 6872–6877.

[44] Murray, M. J.; Ogden, H. M.; Mullin, A. S. Anisotropic Kinetic Energy Release

and Gyroscopic Behavior of CO_2 Super Rotors from an Optical Centrifuge. *J. Chem. Phys.* **2017**, *147* (15), 154309.

[45] Murray, M. J.; Ogden, H. M.; Toro, C.; Liu, Q.; Mullin, A. S. Impulsive Collision Dynamics of CO Super Rotors from an Optical Centrifuge. *ChemPhysChem* **2016**, *17* (22), 3692–3700.

[46] Ogden, H. M.; Michael, T. J.; Murray, M. J.; Liu, Q.; Toro, C.; Mullin, A. S. The Effect of CO Rotation from Shaped Pulse Polarization on Reactions That Form C_2. *Phys. Chem. Chem. Phys.* **2019**, *21* (26), 14103–14110.

[47] Guelachvili, G.; De Villeneuve, D.; Farrenq, R.; Urban. W.; Verges, J. Dunham Coefficients for Seven Isotopic Species of CO. *J. Molec. Spec.* **1983**, *98*, 64-79.

[48] Farrenq, R.; Guelachvili, G.; Sauval, A. J.; Grevesse, N.; Farmer', C. B. Improved Dunham Coefficients for CO from Infrared Solar Lines of High Rotational Excitation. *J. Molec. Spec.* **1991**, *149*, 375-390.

[49] Khodorkovsky, Y.; Steinitz, U.; Hartmann, J.-M.; Sh Averbukh, I. Collisional Dynamics in a Gas of Molecular Super-Rotors. *Nat. Commun.* **2015**, *6* (1), 7791.

[50] Tashkun, S. A.; Perevalov, V. I., CDSD-4000: High-resolution, High-Temperature Carbon Dioxide Spectroscopic Databank. *J. Quant. Spectrosc. Radiat. Transf.* **2011**, *112* (9), 1403-1410.

[51] MacPhail-Bartley, I.; Wasserman, W. W.; Milner, A. A.; Milner, V. Laser Control of Molecular Rotation: Expanding the Utility of an Optical Centrifuge. *Rev. Sci. Instrum.* **2020**, *91* (4), 045122.

[52] Semenov, N. N. On The Theory of Combustion Processes. *Z. Phys. Chem.* **1928**, (48), 571-582.